UiT
THE ARCTIC
UNIVERSITY
OF NORWAY

FACULTY OF SCIENCE AND TECHNOLOGY

Department of Geology

Investigation of seafloor craters and mounds in the central Barents Sea

—

Magnus Sørbø
EOM-3901 Master thesis in Energy, Climate and Environment
June 2016

I

Abstract

Recently acquired datasets of multibeam, echosounder and seismic data reveal the geomorphology and distribution of seafloor craters and mounds in central Barents Sea. The study found 288 craters, 227 pingos and 119 gas flares in the area, each with its own distinctive appearance. The majority of pingos lie inside or close to craters. This indicate a connection between the two features.

Inspection of the subsurface shows several faulting systems and migration pathways underneath the seabed features. Migration of hydrocarbons supplies the shallow subsurface with gas, trapping the gas inside cages of ice, to become gas hydrates. Models of the gas hydrate stability zone (GHSZ) show conditions sufficient to sustain a considerable amount of hydrates in the subsurface. Signs of gas hydrate BSRs are observable inside and outside of the study area.

Four major glaciations covered the study area during Late Cenozoic. This have resulted in different climatic events, affecting the GHSZ. The GHSZ has decreased significantly since Last Glacial Maximum, leading to vast dissolution of gas hydrates and release of free gas. The pressure change, caused by the ice sheet movement, reactivated faults and enhanced supply of gas to the shallow subsurface. Gas flares at the seafloor indicate an active fluid system. The hydrates push the seafloor upwards to create submarine pingos. This has caused one or several blowouts after reaching the threshold limit of the seafloor. The depressions, created by the blowouts, are interpreted to consist of 20 % pockmarks (50-100 m), 53 % large pockmarks (100-300 m) and 27 % fluid flow craters (>300m).

III

Acknowledgement

v

Table of Contents

1-Introduction

Solheim and Elverhøi (1993) discovered circular depressions and mounds on the seafloor in the central Barents Sea (Fig.1). The observed features varied in size, and occurred with different densities throughout the study area (Fig.2). Recently acquired marine geophysical datasets enable us to visualize and study the geomorphological features in more detail. In addition, the datasets show the internal structures, and links with deeper lying structures.

1.1 - Objective

The overall objective of this thesis is to get a better understanding of the formation of craters and mounds in the central Barents Sea (Fig.2).

In order to accomplish the main goal, there are several secondary objectives:

- Map the distribution of craters and mounds.

- Map the internal structure of features.

- Map fluid flow features.

- Relate gas flares in the water column with geomorphological features

This study utilizes multibeam-datasets to visualize the bathymetry, echosounder-datasets to visualize gas in the water column, and seismic data from University of Tromsø and the Norwegian Petroleum Directorate to visualize the subsurface.

1.2 - Motivation

Studying the geomorphological features is of great interest in a scientific matter. The features are important to understand in several topics. One topic is the global climate change. Global warming is an increasing problem. The knowledge of fluid migration is an element to improve knowledge on global climate change. Fluid seepage poses a threat to the environment, as the fluids mainly consist of methane. Methane is a gas with a significant environmental impact. It is 10 times as dangerous over a 100-year period as carbon dioxide (IPCC, 2013). A large release of methane into the water column, and possibly to the atmosphere, would have possible serious consequences for the climate system

The release of gas to the water column is usually linked with craters on the seafloor. Craters on the seafloor also act as a reminder of the stability issues of the seafloor. Submarine landslides occur from time to time. The Storegga-slide, outside the coast of Norway, as one of the most

famous. The development of craters on the seafloor, leads to a stability reduction of the subsurface and poses as a geohazard. Additionally, the presence of gas shows that there are factors in the subsurface able to create landslides. The formation mechanism for the geomorphological features are thus important to understand, both to avoid landslides and to predict the occurrences.

The fluid migration of the area is important in order to understand the formation mechanism. Fluid migration acts as a stability factor, and can direct attention towards deeper laying structural features. Possible also concerning new gas and oil reservoirs. Except the obvious relation to conventional hydrocarbon exploration, gas hydrates are another possible new resource. Similar observed craters and mounds, as those of the study area (Fig.2), proved to be gas hydrate related. Gas hydrates are a conceivable new energy resource, as the hydrates consist of large amounts of compressed methane. The world may find a new energy resource with further research and understanding of gas hydrates and their properties.
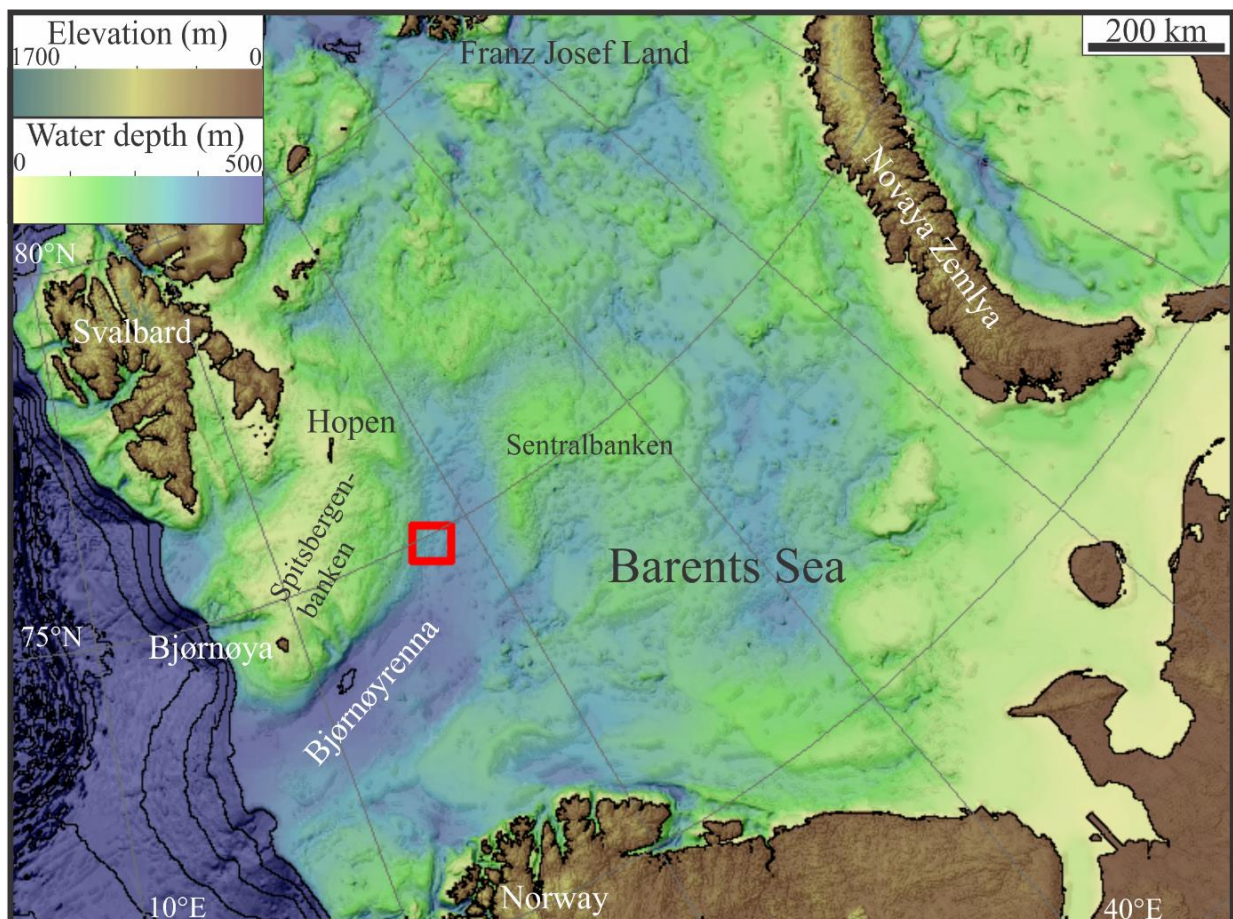
Figure 1: Overview of the Barents Sea, with the study area lying inside the red box.
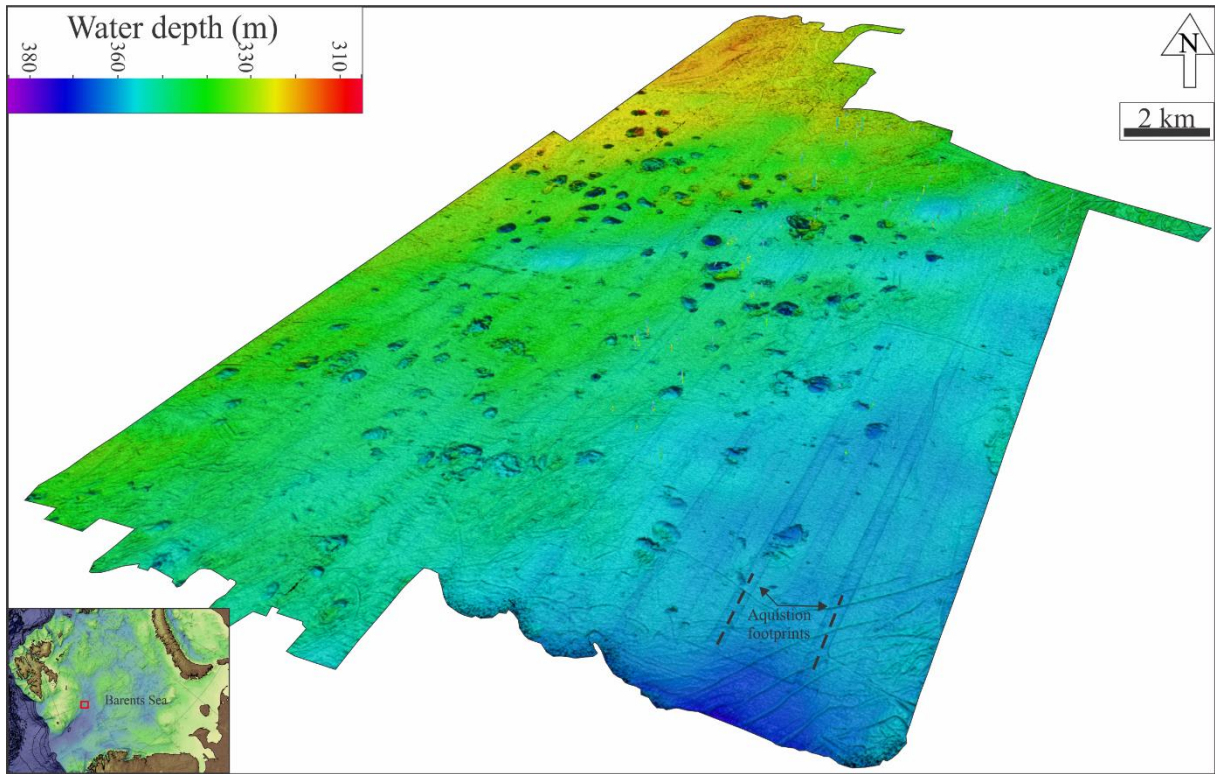
Figure 2: Overview bathymetric map of the study area.

2 – Subsea fluid flow

Identifying subsea fluid flow on geophysical datasets is performed by looking for specific signs in the seismic sections. Fluids present in the subsurface affect the properties of the subsurface, leading to visible changes on seismic surveys. The change is observable as high amplitude anomalies. Hydrocarbons present in the subsurface result in a prominent reduction of the p-wave velocity, changing the acoustic impedance. The acoustic impedance is the product of density and seismic velocity of sediment packages, and is observable at interfaces between these packages. Acoustic impedance is the property that produces the seismic reflection. The high amplitude reflection anomaly, commonly called a hydrocarbon indicator, represents a fluid contact, and is shown as bright spots (Andreassen, 2009) (Fig.3).

Several other signs of hydrocarbons present in the subsurface exist, like phase reversal, meaning a shift of 180° along a continuous reflector (Fig.3), resulting in a peak becoming a trough and vice versa (Løseth et al., 2009). Two other signs are dim spots and flat spots (Fig.3). Dim spot is the effect of a local decrease of amplitude along a reflector, while flat spot refer to the effect the lower part of a gas/oil-water contact have in the seismic section. The flat spot is easily visible as they have an angle relative to the surrounding stratigraphic layers (Løseth et al., 2009).
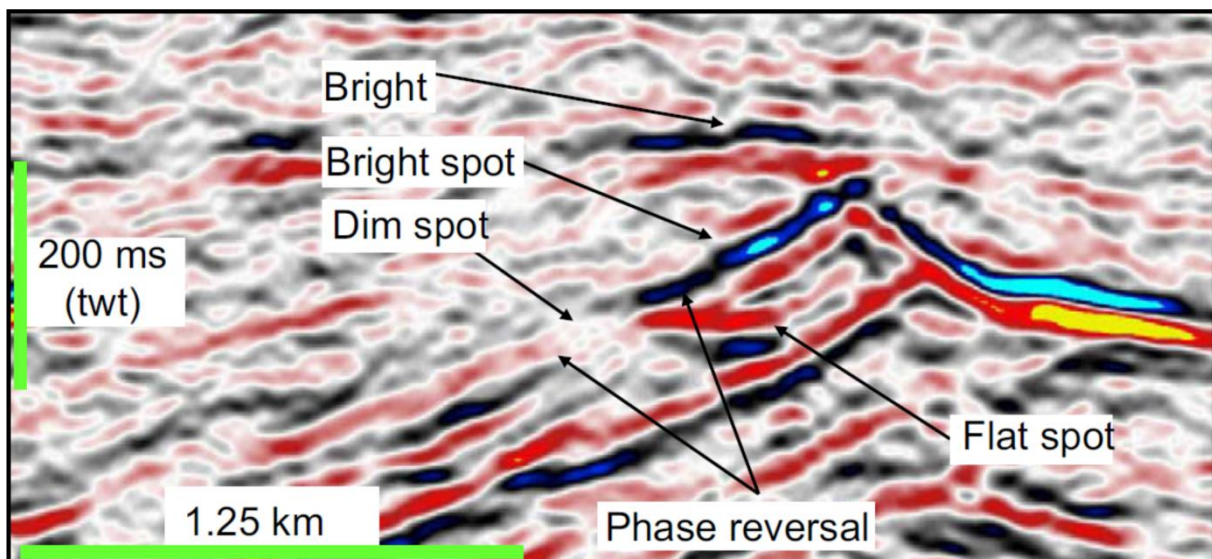
Figure 3: Image showing different seismic amplitude anomalies. From Løseth et.al (2009).

2.1 – Gas chimney

Fluid migration in the subsurface disturb the seismic reflectors. In seismic sections, migration pathways for fluids appear as vertical zones of acoustic masking, referred to as gas chimneys (Løseth et al., 2009). Fluid migration create vertical zones of low seismic amplitude, frequency and coherency, at which hydrocarbons migrate to shallower subsurface conditions (Sun et al., 2012). The transportation zone may appear as both distinct vertical zones, but also as diffusively masked areas (Løseth et al., 2009).

Typically, gas chimneys are in association with bright spots at the edges (Andreassen et al., 2007). Gas in the sediments create overpressure, which result in fracturing of friable rocks. Fracturing of rocks results in increased fluid migration and horizontal migration of fluids, into sediment packages. Thus, it is possible to observe fluids as bright spots on the flanks of gas chimney features.

It is important to emphasize that the hydrocarbon indicators need to appear together, in order to conclude whether or not the anomalies are made of hydrocarbons, or just are lithological changes.

2.2 – Gas hydrates:

Previous studies of gas chimneys document a trend of being associated with the gas hydrate stability zone (GHSZ) (Mienert et al., 2001; Bünz et al., 2003). The GHSZ is the zone where gas hydrates are stable. Gas hydrates are gas trapped inside a compound of ice (Sloan, 1998). Predominantly methane (CH_4), but also propane (C_3H_8) and ethane (C_2H_6) among others.

Gas hydrates exist in various parts of the world, but present with a set of necessary basic conditions (Collett et al., 2009). From the gas chimneys or fluids migrating through faults, an adequate supply of gas is necessary. Secondly, an adequate supply of water is needed. Either provided through absorption of seawater, or by natural occurrences in the subsurface. At last, there is a need for specific temperature and pressure conditions (Hovland, 2005). Generally, the right conditions are on land in Polar Regions, since the surface temperatures are sufficiently cold. In marine environments, gas hydrates exist at depths deeper than 300-500 m (Hovland, 2005). The occurrence of gas hydrates are disperse molecules in sediment pore spaces, like nodules of pure hydrate, cementing pore spaces, or as a layered structure (Sloan, 1998).

2.2.1 – Gas hydrate stability zone
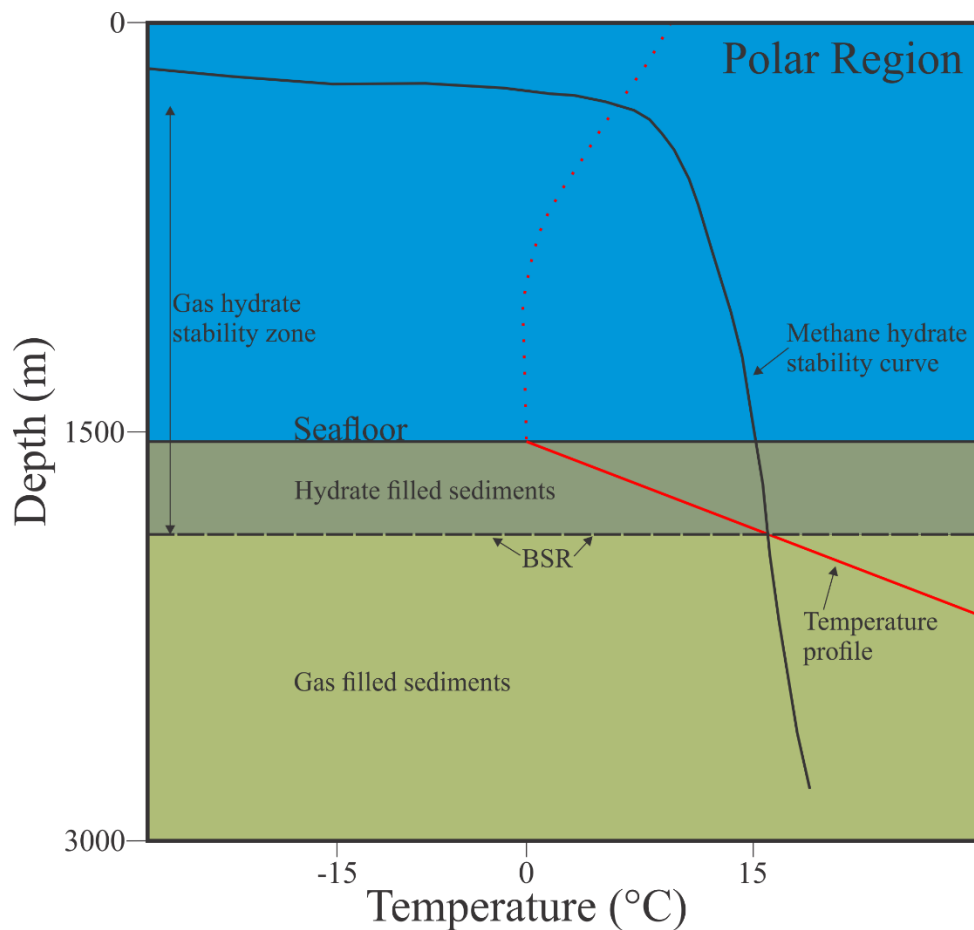
Figure 4: Sketch showing the gas hydrates stability zone in Polar Regions. Modified from Chand & Minshull (2003).

Gas hydrates are stable in specific conditions, and are vulnerable to change in environment. The zone of which they are stable is the gas hydrate stability zone (Fig.4) (Hyndman and Davis, 1992). Inside this zone gas hydrates can form, while underneath this zone free gas exist in the sediments. This creates a transition zone at the lowermost end of the GHSZ. The transition zone creates a change in acoustic impedance, because free gas has lower seismic velocity compared to gas hydrates. The interface is observable as a reversed polarity reflector mimicking the seafloor, called a bottom-simulating reflector (BSR) (Shipley et al., 1979; Hyndman and Davis, 1992). Two other types of BSRs exist, both related to biogenic material, and occur with the same polarity as the seabed reflector in seismic sections (Nouzé et al., 2009).

The gas hydrate BSR depends on gas hydrate formation, and relies on temperature and pressure conditions. Thus, the BSR follows isotherms rather than stratigraphic horizons. In turn, it make the BSR crosscut dipping bedding planes. Consequently, detection of a BSR proves difficult when sediment packages are parallel (Hornbach et al., 2003).

Gas hydrate stability relies on several factors: pressure, temperature, salinity, hydrothermal gradient and chemical composition of gas. Pressure and temperature are the most influential factors. Increased pressure increase the GHSZ and vice-versa. Increased temperature decrease the GHSZ and vice-versa. Salinity affect the pressure and temperature, resulting in a decreasing GHSZ with increasing salinity. Additionally, the chemical composition and ionic impurities plays a vital part (Collett, 2000; Hovland, 2005; Vadakkepuliyambatta et al., 2015).

2.3 - Pockmarks

Pockmarks are geomorphological features related to fluid flow and gas hydrate accumulation. They are shallow seabed depressions, but may also occur in deeper water. The physical appearance and shape of the depressions varies greatly. Most often pockmarks appear with circular shape. There are several definitions of the size and depth of pockmarks. Generally, pockmarks are between 50 and 100 m in diameter, and with a depth ranging from 1-3 m (Judd and Hovland, 2007). Ostanin (2013) developed a classification system based on the size and depth of observed craters. The system far exceed the suggested dimension from Judd and Hovland (2007), but act as a reminder of the difference in approach as to what define a pockmark.

Generally, pockmarks exist in siliciclastic sediments. However, they are also observable in carbonate settings (Benjamin et al., 2015). The main factor separating them from other morphological depressions is that they are erosive features, where the erosive agent acts from underneath, rather than from above (Judd and Hovland, 2007).

According to Judd and Hovland (2007) three main factors determine the formation of pockmarks:

1: Formation mechanism
Meaning a sufficient supply of gas, and an accumulation of gas in the subsurface.

2: Stable seabed
Meaning a seabed not consisting of large-scale erosional or depositional events.

3: Sediments suitable for pockmark formation
Meaning mainly fine-grained sediments in the area. However, pockmarks are also observable in relation to other features, such as iceberg ploughmarks and submarine channels.

The pockmark triggering mechanism is important to understand, and extensive research have been and is still performed. A range of triggering factors have been suggested, but each

dismissed due to a lack of correlation with the observed features. Solheim and Elverhøi (1993) preferred the gas hydrate explanation, and dismissed mechanisms such as meteors and glacial erosion.
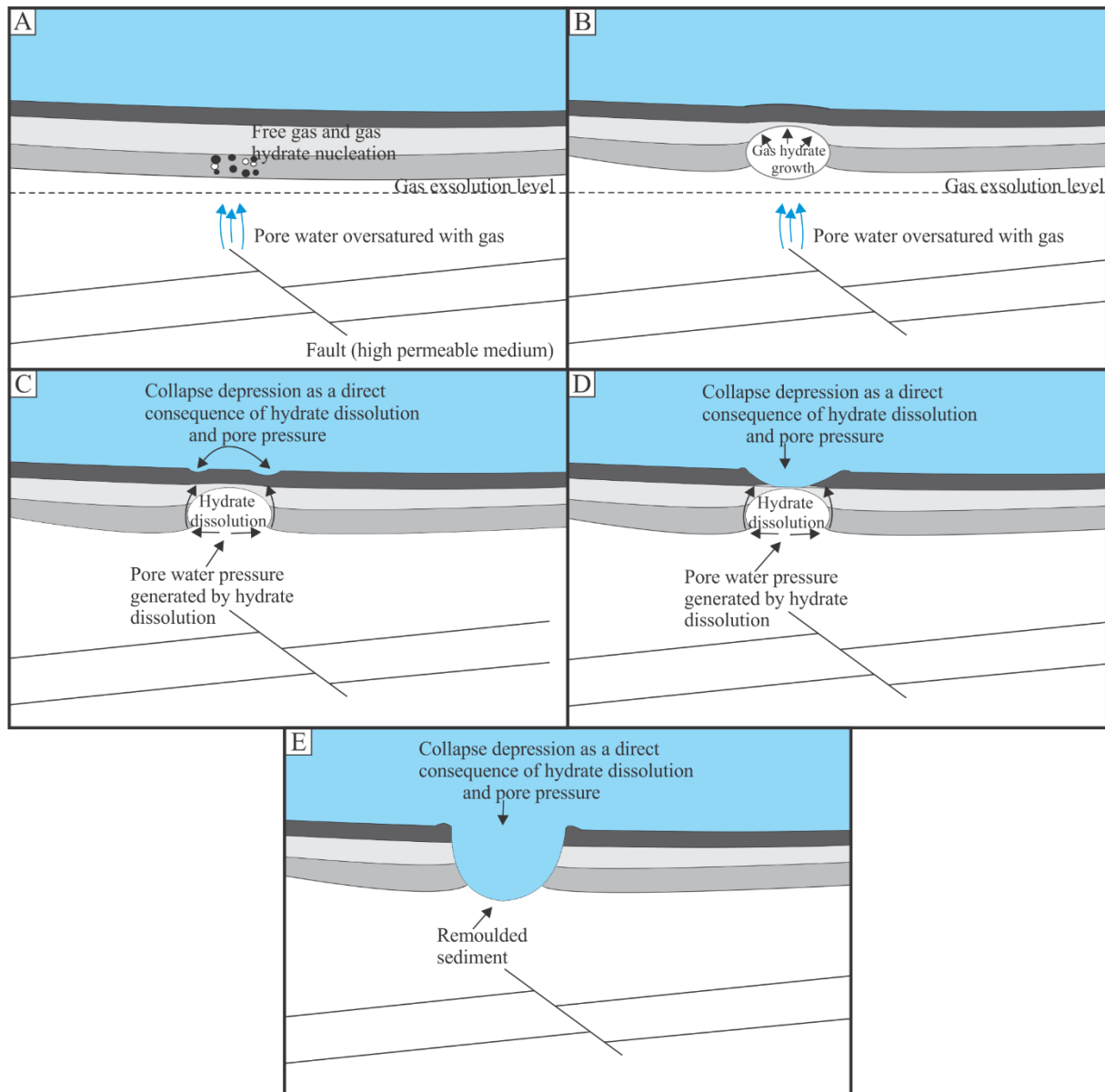
Figure 5: Sketch showing the different stages of pockmark formation as suggested by Sultan. Modified from Sultan et.al. (2010).

The principle behind formation of pockmarks is based on a continuous supply of gas either from deeper reservoirs, or from dissolution of gas hydrates (Fig.5). Supplying the shallow stratigraphic features with free gas leads to accumulation in the subsurface. A layer seals the dissolute free gas until the accumulated gas exceed a threshold limit, resulting in an explosive release of free gas and expulsion of sediments from the seafloor, creating a deep crater called pockmark.

Pockmarks found at present day tend to be inactive or dormant features (Judd and Hovland, 2007). Faulting systems underneath the depressions often link with the features, but as the crater form, a sealing of the migration pathway occur.

2.4 – Gas hydrate mounds

In contrast to the negative topographical features of the previous section, there are positive features. Mounds are such features, and appear as elevated areas on bathymetric datasets. The mounds appear in a variety of sizes, but tend to be smaller than the depressions. Seafloor mounds related to fluid flow characterizes in two groups: mud volcanoes and submarine pingos.

Submarine pingos are positive topographical features related to gas hydrates. Pingos have a variety of shapes, but generally, they are circular. They are commonly 30-50 m high, and up to 400 m in diameter (Bates and Jackson, 1987). The first research on pingos suggested water migration as a formation mechanism. Frozen water in the subsurface expands, and the seafloor rises. The reason for the suggested triggering mechanism was observation of mounds in high latitudes and cold climates. In 2006, Hovland and Svensen found that gas hydrates also contribute to formation of pingos.

They postulated three prerequisite factors for pingo formation;

1: High flux
Meaning a relatively high flux of hydrocarbons flowing in the subsurface, resulting in a continuous supply of hydrocarbons are essential to sustained hydrate growth.

2: Cool bottom water temperature
Low temperature enhancing the formation of gas hydrates. In addition, cool water temperature lead to low dissolution of existing gas hydrates, further contributing to growth.

3: Water depths deeper than 400 m
At water depths sufficiently deep a higher degree of supercooling of fine-grained sediments occur. Ensuring gas hydrate formation.

To summarize, according to Hovland and Svensen (2006), gas hydrates are necessary, both in stable form, but also under continuous formation. This means an accumulation of hydrates is necessary. Hydrates grow in size for a prolonged period of time result in hydrates pushing on the seafloor, to create pingos. During this process, gas migrates upwards from deeper laying

reservoirs. From the water column, seawater enters through the adjacent sediments, exchanging the depleted seawater from hydrate formation (Hovland and Svensen, 2006).

2.5 – Gas flares

After migration of gas from shallow or deep reservoirs to the shallow subsurface, the gas may breach the seafloor, leaking into the water column. Seepage of gas appear as bubbles. Gas flares refer to the bubbles in the water column, floating towards the sea level. The gas inside the bubbles affect the acoustic and mechanical properties of the water. This means that the sound attenuation increases, sonic energy scatters, speed of sound propagation changes and tensile strength of seawater and sediments are reduced (Judd and Hovland, 2007).

Due to the changes of water properties, gas flares are easy to map with an echosounder. Dependent on the pressure when gas release, the flare can reach high in the water column. West of Svalbard gas flares reached 700 m from the seafloor (Bünz et al., 2012). The existence of gas flares is an indication of an active fluid system at present day.

3-Geological Setting

3.1 – The Barents Sea region

The Barents Sea is a large region, located north of Norway and Russia (Fig.1). Eastwards the island Novaya Zemlya bounds the sea, Franz Josef Land bounds to the north, Svalbard to the west. While southwest, the Barents Sea is bounded by the eastern margin of the deep Atlantic Ocean. In total, the Barents Sea as a region covers 1.3 million km^2 (Doré, 1995). The bathymetry of the Barents Sea characterizes by being an epicontinental shelf with average water depth of 300 m (Doré, 1995). Banks and troughs are visible, ranging from 50-300 m and 300-500 m, respectively (Vorren et al., 2011) (Fig.1).

A large-scale monoclinal structure in the middle of the Barents Sea divide the sea into two major provinces. The monoclinal stretch from north to south, and result in a western part and an eastern part. Complex tectonic activity influence the eastern Barents Sea at Novaya Zemlya, Timan-Pechora Basin and the Uralian orogeny (Smelror et al., 2009). On the other hand, a major rifting process during post-Caledonian time shaped the land of the western Barents Sea province. In addition, there were several other rifting periods, leading to continental break-up along the western margin of the Eurasian plate (Smelror et al., 2009).

3.2 – Geological history of the Barents Sea

The Barents Sea area originally formed from two major continental collisions during the Paleozoic, succeeded by a time of separation. The first took place in the Caledonian orogeny about 400 million years ago (ma.), resulting in a closing of the Iapetus Ocean. This collision led to the merging of the Laurentian and Baltican plates, known as the Laurasian continent (Doré, 1995; Smelror et al., 2009).

Several sightings of north-south strike and northeast-southwest strike basins appeared due to the orogeny. Post-Caledonian rifting led to a change in strike from N-S in Svalbard, to NE-SW outside of Finnmark. After the Caledonian orogeny extensive erosion took place, culminating in several horst-graben structures and deposition of evaporates (Smelror et al., 2009).

In the Triassic, the two orogenies collapsed, and the supercontinent Pangea separated (Doré, 1995). Several clinoform belts are observable in Triassic sediments, ranging from 200 to 400 m high (Lundschien et al., 2014). Two such clinoform-belts dominate the central part of the Barents Sea (Riis et al., 2008). They are potentially good source rocks, due to the high organic content. A dramatic thinning of the Lower and Middle Triassic occur from Bjarmeland Platform towards Fingerdjupet Basin (Fig.7). A larger thickness of Late Triassic compensate for the

thinning (Lundschien et al., 2014). During the Triassic, few large tectonic activities occurred, but erosion continued and led to uplift of the Barents Sea Shelf, resulting in a westward progradation and deltaic environment (Smelror et al., 2009). A major transgression in Late Jurassic led to flooding of the entire Barents Sea, resulting in a deep-marine setting. A major volcanic event in the Cretaceous near Franz Josef Land led to even more uplift, and the area transported sediments westwards, while rifting processes occurred, thus creating deep basins (Smelror et al., 2009).

In Paleocene-Eocene continental break-up of the North Atlantic occurred. A passive shear-margin developed. The two areas, Norwegian and Greenland Sea, suffered from dispersion throughout the Oligocene, establishing a marine connection of the North Atlantic-Arctic marine setting in the Miocene. Deposits from the Cenozoic are practically non-existent in the central Barents Sea, because of extensive erosion during the Plio-Pleistocene deposited large amounts of sediments at the shelf break (Smelror et al., 2009).

3.3 – Glacial history of the Barents Sea

Signs of large-scale glaciations, through increased ice-rafted debris flux and increased distribution of dropstones (>1 cm), in the Barents Sea are from about 2.7 Ma (Knies et al., 2002). Indication of growth of ice between 2.3-1.6 Ma, mainly limited to the northern areas of the Barents Sea, are in contrast to the southwestern part of the Barents Sea (Butt et al., 2000; Sejrup et al., 2005; Vorren et al., 2011). At seismic sections from the southwestern part of the Barents Sea, indications of sixteen glacial advances during the last 1 Ma are observed (Solheim et al., 1996). Based on seismic sections evidence of eight major glacial advances during the last 0.44 Ma and 1.5 Ma have also been suggested (Sættem et al., 1992; Laberg and Vorren, 1996; Andreassen et al., 2004).

During the Quaternary, these glaciations extended from the Barents and Kara Sea, toward the land areas in the south (Svendsen et al., 2004). There have been much debate upon the extent of the ice sheet in the different ice age periods, and especially the last glacial maximum (LGM).

Based on seismic data, Andreassen (2004) suggested that during the last 1.5 Ma grounded ice reached the southwestern shelf edge in the Barents Sea eight times. Recent studies of the Late Cenozoic show ice sheets reached the shelf edge four times (Vorren et al., 2011). Extensive geological fieldwork resulted in modelling of a reconstruction of the ice sheet extent. Knowledge of the sediments found at present day comes from core-samples. Inspection of long cores and 3D seismic surveys have resulted in better understanding of the chronology and

dynamics of the ice sheets (Vorren et al., 2011). Thus, ice reaching the shelf edge happened during these four periods (Fig.6): 1) Late Saalian (130 000 years ago), 2) Early Weichselian (90-80 000 years ago), 3) Middle Weichselian (60-50 000 years ago) and 4) Late Weichselian (20-15 000 years ago) (Svendsen et al., 2004).
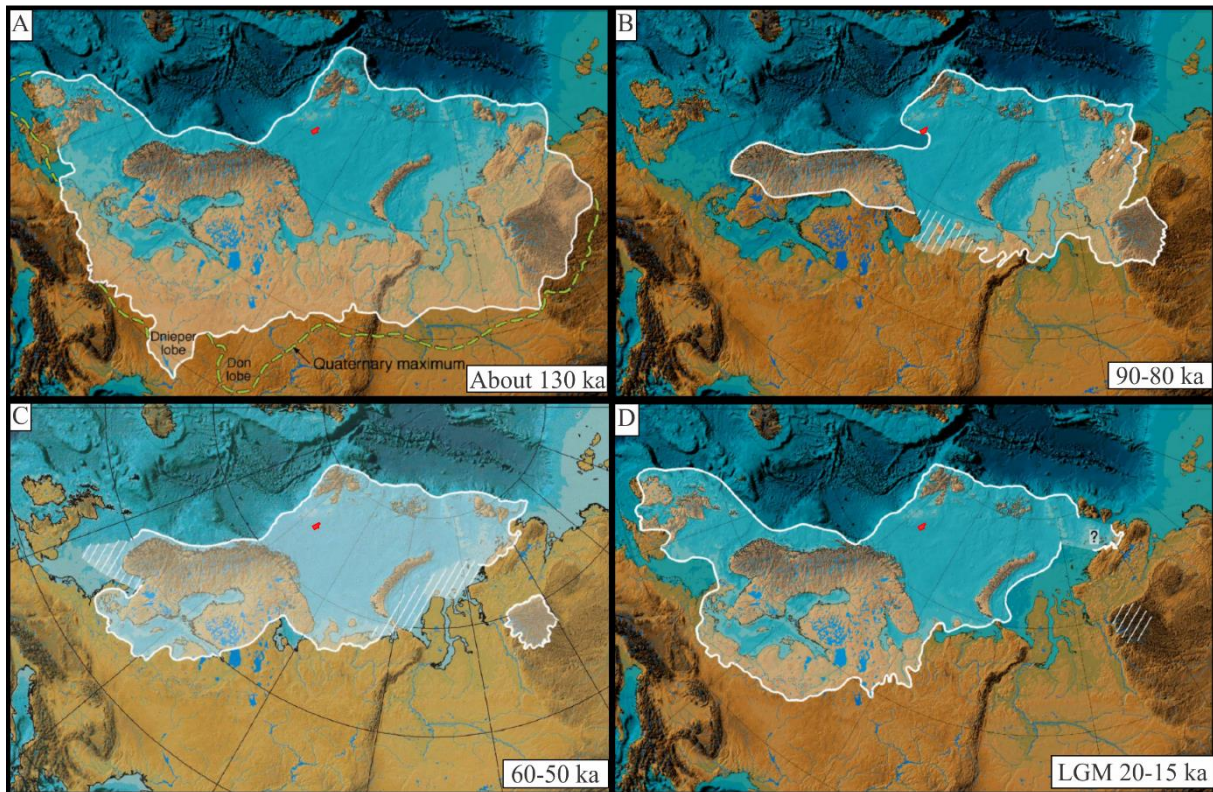
Figure 6: Ice sheet extent during the last four major glaciations. Modified from Svendsen et al. (2004).

Bjørnøyrenna trough is a major geomorphological feature of the Barents Sea, stretching 750 km in length, and 150-200 km in width, Its location is easily visible on bathymetric maps of the Barents Sea (Vorren et al., 2011) (Fig.1). At the shelf edge visible fan-shaped protrusions are observable. Large ice streams in the trough transported sediments towards the trough mouth fan, at the shelf edge (Andreassen et al., 2008). Investigation of the trough mouth fans suggest the fans acted as depocentres for sediments. Transportation of sediments due to large ice streams and glaciers, acts as erosional agent of the seabed. This led to a difference in sediments in the subsurface. At the very top there are glacial deposits, while underneath there is sedimentary bedrock. The difference in rock properties between these two create a strong reflector, called the upper regional unconformity (URU). Vorren et al., (2011) proposed that the URU is the erosional base of the glacial periods the area experienced.

3.4 – The study area

The study area (Fig.2) is situated in central Barents Sea, and is selected because of the large amounts of depressions and mounds. In this report, investigation of an area of 690 km^2 took place. The location of this area is 245 km northeast of Bjørnøya and 187 km southeast of Hopen (Fig.1). Its location is at the edge towards Spitsbergenbanken, in the middle of Bjørnøyrenna trough. The trough acted as transport route for sediments and ice sheets, which in turn influenced the study area.
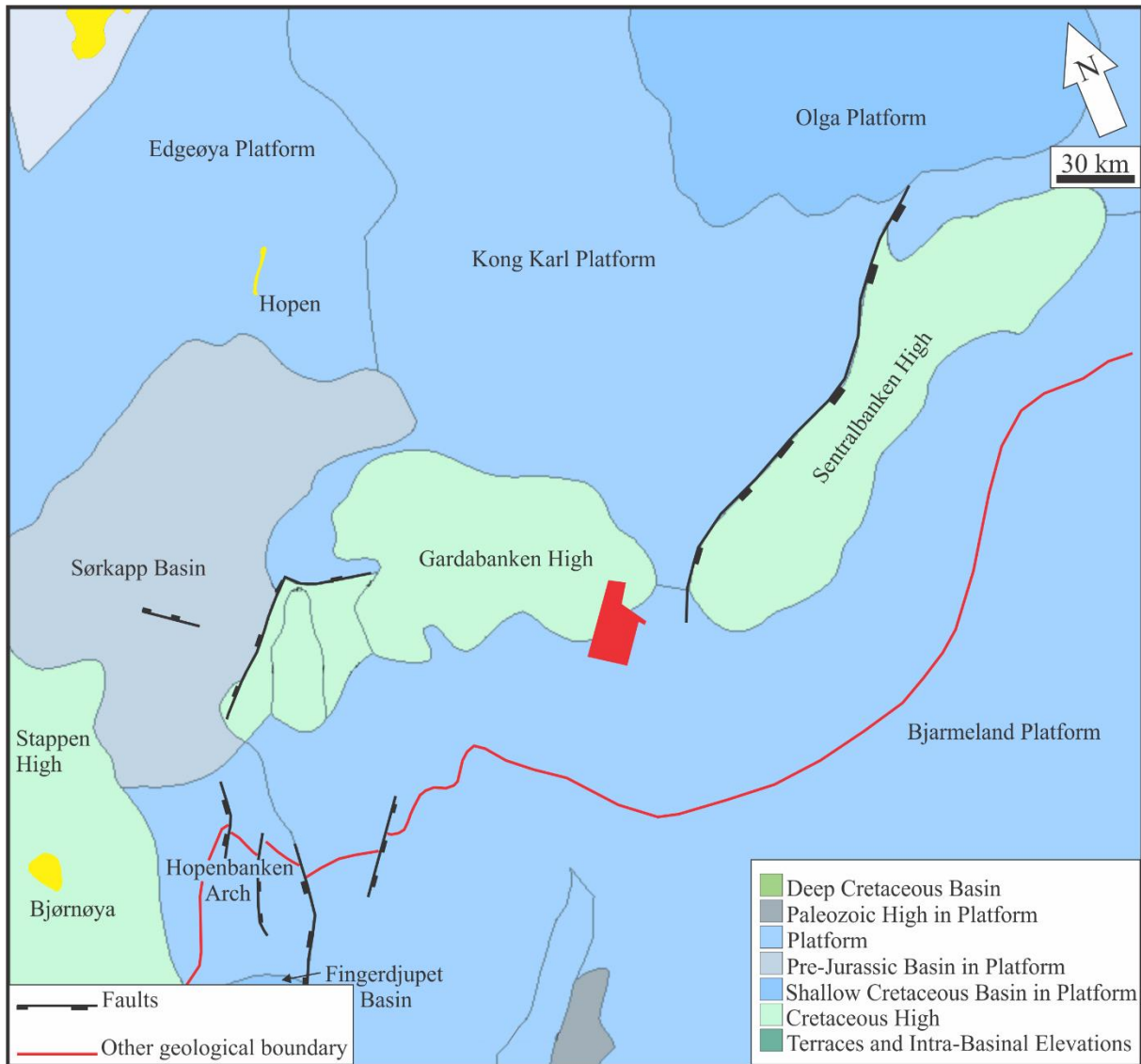
Figure 7: Overview of the structural elements of the Barents Sea. Modified from NPD (2016).

The Barents Sea consist of several basins and platforms (Fig.7). Each with its own distinctive sedimentological property. The study area location crosscuts two structural elements. These are Gardabanken High, and Bjarmeland Platform (Fig.7). Gardabanken High is a cretaceous high, while Bjarmeland Platform is a platform. Gardabanken High being a cretaceous high refer to the fact that the elevated bank area was part of a Mesozoic uplift. The uplift of Gardabanken High led to even more transport of sediments into Bjørnøyrenna from north-northwest. The erosion as a cause of mass movement in Bjørnøyrenna, combined with large-scale tectonic events has contributed to the slope of the study area (Fig.2). The highest area of the study area lies at a water depth of 317 m, while the lowest lies at water depths of 362 m. Despite this, the seafloor is relatively flat, with the exception of the geomorphological features observed (Fig.2).
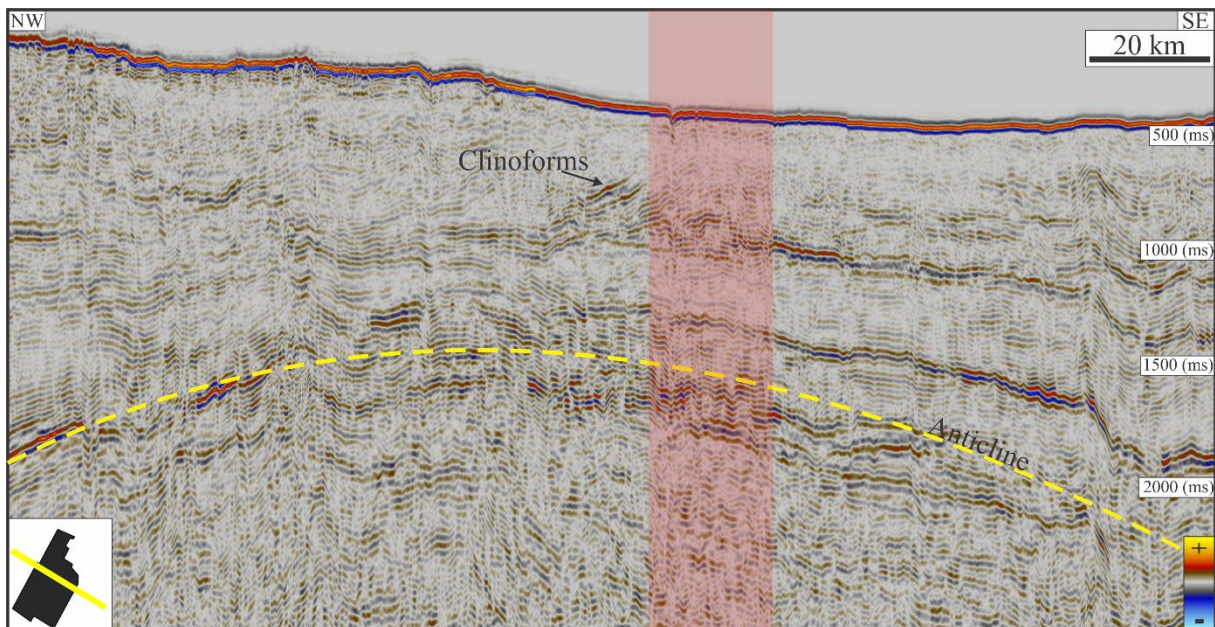
Figure 8: Regional setting of the study area from the seismic section NPD_BA_82_STR_06.MIG_FIN.D10_82.-22.5-9868. The red rectangle outlines the study area extent.

In the subsurface, there are visible faulting system bearing witness to the rifting processes the Barents Sea experienced (Smelror et al., 2009). In the subsurface of the study area, an anticline exist (Fig.8), showing that the area previously experienced uplift. Anticlines are generally good structures for hydrocarbons to migrate. Anticlines also tend to enhance fault systems, which contributes to the already existing faults caused by rifting processes.

The geological setting of the study area has changed between continental and marine (Smelror et al., 2009), resulting in deltaic environment underneath the study area, when the shoreline extent was sufficient. This has led to formation of clinoforms that are observable in the subsurface of the study area (Fig.8).

In addition to the geological influence, the glacial environment clearly contributed to the present day appearance of the study area. During the Quaternary, the study area experienced several major glaciations (Fig.6). Bjørnøyrenna acted as the main transport route for ice sheets, during these glaciations. The four major glaciations occurred 130 thousand years ago (ka), 90-80 ka, 60-50 ka and 20-15 ka (Fig.6). At the second glaciation (Fig.6, B) happening 90-80 ka the ice sheet extent was more limited in Bjørnøyrenna. Thus, the study area lies almost at what was the edge of the ice sheet extent.
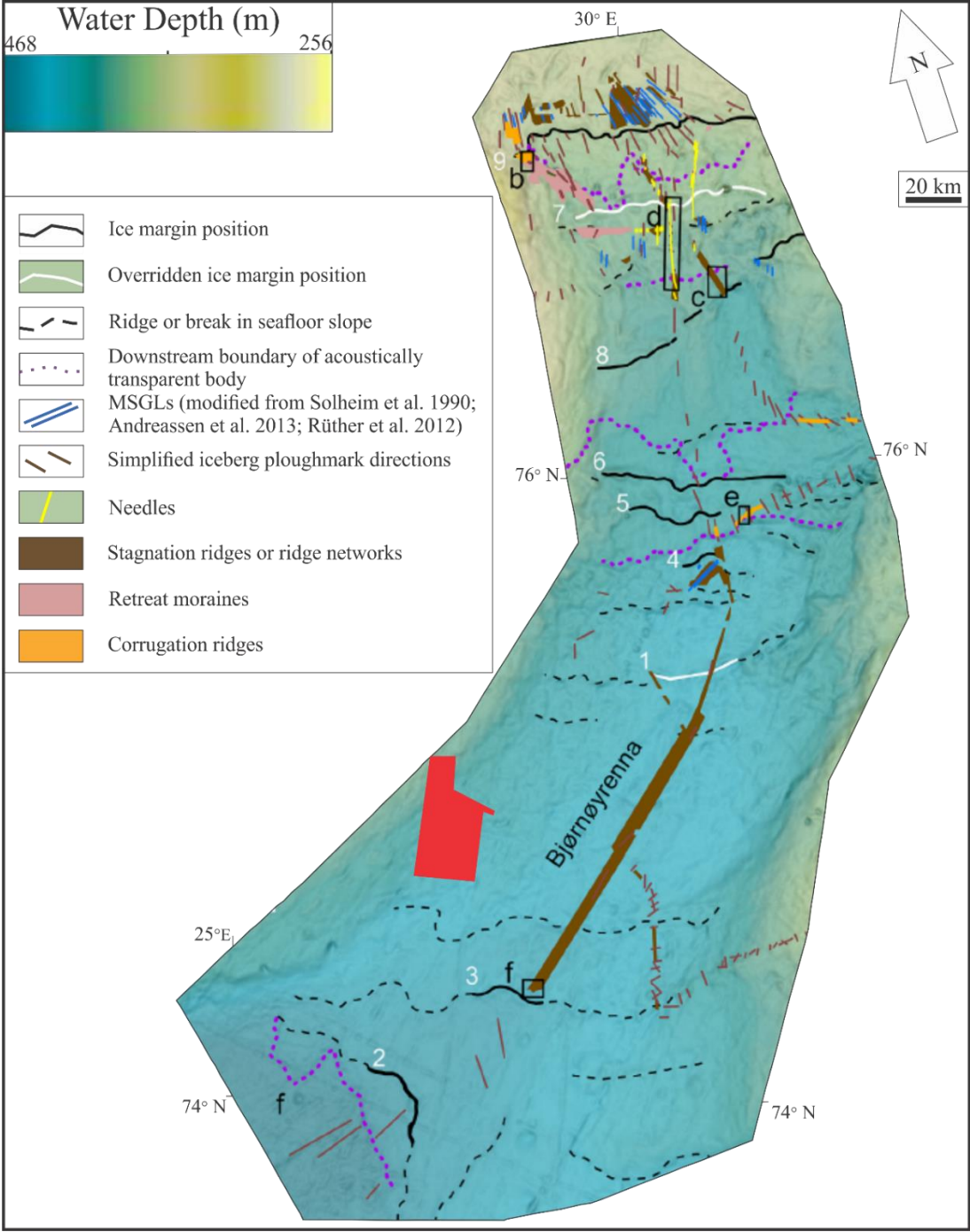
Figure 9: Glacial setting of the study area. Modified from Bjarnadóttir et al. (2014).

Bjarnadottir et al. (2014) performed an extensive study of the glacial features found in Bjørnøyrenna (Fig.9). In the beginning of Bjørnøyrenna, mega-scale glacial lineations, ice margin positions, boundaries of acoustically transparent bodies, iceberg ploughmarks, needles and stagnation ridges and stagnation networks are observable (Fig.9). These acoustic transparent bodies, ice margin positions and ridges or breaks in seafloor slopes, goes across the whole of Bjørnøyrenna. Thus, it is reason to believe that the same processes are observed in other locations of Bjørnøyrenna (Bjarnadóttir et al., 2014), affecting the seafloor of the study area.

4- Data and Methods:

4.1-Data Acquisition

Data acquisition happened during two cruises. The first acquisition took place in 2013, and the second in 2015. Centre of Excellence for Gas Hydrate, Environment and Climate (CAGE) were responsible for collecting the data. CAGE is a part of the geology department at the University of Tromsø that own the research vessel Helmer Hanssen. The boat is equipped with several monitoring devices, such as multibeam echosounder, single beam echosounder and a 2D reflection seismic device.

4.1.1 - Multibeam echosounder:

A Kongsberg Simrad EM 300 is installed at Helmer Hansen. This is a multibeam echosounder device, which measures the two-way travel time of a sound wave, from the transmitter to the seafloor, and back. The sound pulses have frequencies of 30 KHz, which is too high to penetrate the seafloor, leading to high-resolution bathymetric maps of the seafloor. The horizontal gridding consisted of the whole area being mapped by a cell size (X, Y) of 15x15 m, whereas a portion of the study area were mapped with cell size 5x5 m.

The swath width of the system is dependent on the seabed sediments. In shallow water, the swath width is commonly four times the water depth, and here it means it is less than 500 m. The maximum swath width is 5 km. The gathered signal attenuate due to a security measure to avoid damaging the system when hitting ice. In addition, there is a lower quality of the signals furthest away from the transmitter, as these signals travel the longest distance and have a lower angle of reflection.

4.1.2 - Single beam echosounder:

A Kongsberg Simrad EK 60 is keel-mounted at the Helmer Hansen. Primarily the single beam echosounder estimate depth to the seafloor. Sound pulses shoot out from the transducer, and are later received. The Simrad EK 60 can use three different frequencies: 18 kHz, 38 kHz, and 120 kHz. The use of different frequencies depend on the depth of the surface. 18 kHz is for depths up to 10 km, 38 kHz for depths up to 2 km, while 120 kHz is used for depths up to 500 m. The single beam echosounder map gas in the water column, leaking from the seafloor. For this purpose either 18 KHz or 38 KHz is preferred.

4.1.3 - 2D Reflection Seismic:

At Helmer Hansen, a mini GI (Generator-Injector) acts as seismic source. The air gun is suitable to acquire high-resolution seismic surveys. To be able to visualize the deeper surfaces 2D reflection seismic analysis is performed. Each lithological interface visualizes because of a change in acoustic impedance. Two main components are necessary to complete the survey. These are the source and the streamer. The mini GI is the source, and shoot seismic waves towards the seafloor by releasing compressed air. A total volume of 30 in^3 is the maximum capacity of the air gun, whereas in harmonic mode, used in this survey, there are pulses of 15 in3. The air supply to the air gun comes from a compressor operating at maximum 210 bars. A high-frequency signal provides information to study the shallow subsurface.

In these surveys oil-filled tubes encloses the hydrophones, commonly known as the streamer. A 16 m long streamer consisting of 20 sensors spread over 6 meters, acquired the data. The air gun was 32 meters behind the ship, while the streamer was at twice the distance. In order to avoid too much noise in the acquired data, the mini GI was 2 m below sea level. The ship had a speed of four knots during the acquisition.

The data were collected with different properties, shown in Table 1.

Table 1: Overview of properties for the Cage seismic data.

Seismic Line	Traces	Samples per trace	Sample Interval (m)	Frequency (Hz)
CAGE_14_KA_SR_03_ brute_stack_mig	5551	6000	0,25	154
CAGE_14_KA_SR_04_ brute_stack_mig	3257	6000	0,25	105
CAGE_14_KA_SR_05_ brute_stack_mig	4036	6000	0,25	143
CAGE_14_KA_SR_06_ brute_stack_mig	3077	6000	0,25	169
CAGE_14_KA_SR_999spark _stack_fkFilt_equalized	3852	4000	0,25	473
CAGE_14_KA_SR_08spark1 _brute_stack_fkFilt	3746	4000	0,25	363
CAGE_14_KA_SR_9spark _stack_fkFilt_equalized	3870	4000	0,25	363
CAGE_14_KA_SR_10spark _stack_fkFilt_equalized	3345	4000	0,25	473
CAGE_14_KA_SR_11spark _stack_fkFilt_equalized	5154	4000	0,25	363
CAGE_14_KA_SR_12_ Brute_stack_deghost_mig	8408	6000	0,25	143
HH13_038_mig_deghost	876	3000	0,5	36
HH13_039_mig_deghost	1080	3000	0,5	86
HH13_040_mig_deghost	1132	3000	0,5	83
HH13_041_mig_deghost	1206	3000	0,5	53
HH13_042_mig_deghost	1624	3000	0,5	95
CAGE15-5-001	5791	3401	0,25	67

2D seismic sections from the Norwegian Petroleum Directorate (NPD) are also provided. The following data properties applied to the NPD lines (Table 2).

Table 2: Overview of properties for NPD seismic sections.

Seismic Line	Traces	Samples per trace	Sample Interval (m)	Frequency (Hz)
2737-89-LS	2958	1501	2	31
7455-87-W	10250	1550	4	23
745730-93	21234	1501	4	20
2730-87(2)	14120	1500	4	18
2735-89-L	2630	1501	2	33
2745-87	13674	1490	4	18
2745-87-SBSW	9156	1500	4	18
745230-94	6598	1500	4	16
G-1-89-LS	2142	1501	2	29
G-3-89-LS	3294	1501	2	24
NPD_BA_82_STR_06.MIG_FIN.D10_82.-22.5-9868	24504	1501	4	14
NPD_BA_82_STR_06.MIG_fin.d23_82.-24.5-4390	13438	1501	4	13

4.1.4 – Artefacts

All data acquisition result in survey footprints, known as artefacts. These footprints occur as parallel lines in both the seismic data and the bathymetric data. Survey footprints are noise in the collected data, leading to features on the seafloor that may be mistaken for real geomorphological features. The survey footprints are noise that correspond to the acquisition geometry (Bulat, 2005).
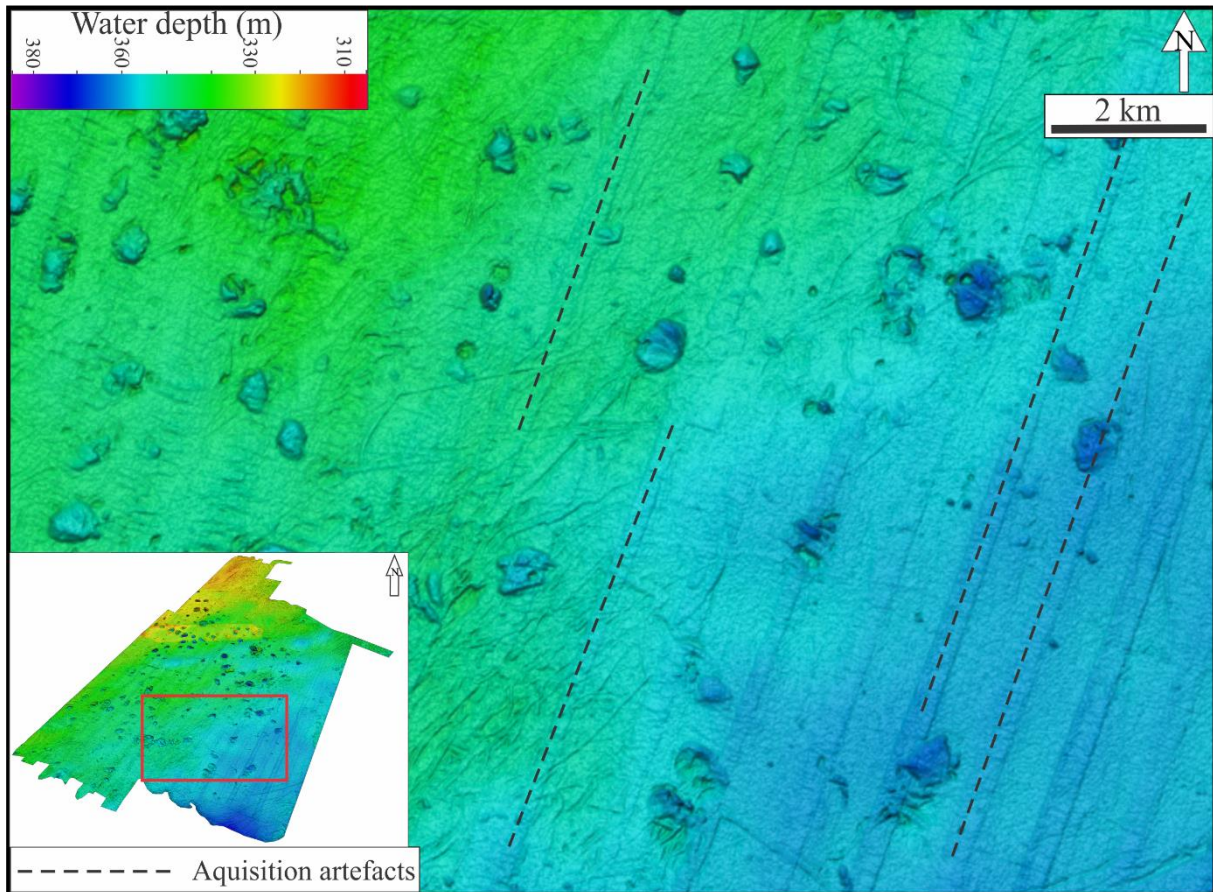
Figure 10: Image showing lineations following the acquisition geometry.

As seen from the image above (Fig.10), there are lineations indicating a time-gap in the survey. The time-gaps suggest real features, while they in fact only exist because of the sampling of data.

4.2-Software

Three main computer programs were used in interpretation of the geomorphological features of the subsea and seabed.

4.2.1 - Fledermaus:

Fledermaus enabled visualization of the bathymetric data. It is used both to map the amount of craters and mounds found, as well as to showing the bathymetric profiles of different features. FMMidwater enabled visualization of gas flares. Differences in density of the gas-bearing water, and seawater are possible to inspect. These can be individually marked, and further implemented in the Fledermaus program. The bathymetric data was further linked with the gas flares.

4.2.2 - Petrel:

Petrel is a software used in order to interpret the seafloor features and subsurface. Petrel enabled visualization of the 2D seismic sections. In addition, the bathymetric data is observable, helping to relate the subsurface with the seafloor. In Petrel, the seabed was interpreted in order to create a relationship with deeper laying features.

4.2.3 - ArcGIS:

The software enabled creation of the overview map of the Barents Sea. Its usage extended to give a better understanding of the geographical location of the study area, and it enabled a better relation of the study area to glacial processes.

4.3 – Modelling of BSR-thickness

The gas hydrate stability zone (2.2.1 – Gas hydrate stability zone) is important to map, as it gives vital information as to where gas hydrates are stable today. It has a very important role in identification of any BSR of the area, thus three models based on the CSMHYD model of Sloan (1998) was created. These are from last glacial maximum, deglaciation, and present day. Modelling two different parts of the study area, resulting in one model, for each period. For the deepest part of the study area, lying at 27°45'36, 7"E, 74°43'3, 7"N and with a depth of 362 m. The second location is for the shallower area at 27°50'41"E, 75°4'12"N and with a water depth of 317 m. To obtain the GHSZ for the area, the software MatLab was used. The software enables to write a code, which calculates the GHSZ depending on different input parameters.

The different input parameters which affect the model are:

1: Gas composition

Two different gas compositions were used in these models. The first was a 100 % methane model, as pure methane gives the thinnest GHSZ. The second composition consisted of 96 % methane, 3 % propane and 1 % ethane based on a study done by Chand et al., (2008) suggesting that in the Barents Sea there is a small amount of 4 % of higher order carbon.

2: Salinity

The salinity, salt content, of the seawater affects the GHSZ. The two models are made with the usual salinity of 35 ‰.

3: Geothermal gradient

Usually, there is an assumption of a constant geothermal gradient of a study area. However, the gradient may be different if different factors are present. These are (Chand et al., 2008):

1: The proximity to piercement features.
2: Basin inversion, resulting in shallow basement rocks.
3: Presence of faults, resulting in a focussed fluid flow in the area.

Previous studies have shown different geothermal gradients in the Barents Sea. Ranging from 31° C/km in the west, to 30 and 35 °C/km in the south (Long et al., 1998). The average geothermal gradient is 30 °C/km in the Barents Sea (Laberg et al., 1998) For the purpose of this model, a geothermal gradient of 40 °C/km was used (International Heat Flow Commision,

2016). The geothermal gradient measurement is situated 80 km northwest of the study area, but is the nearest measurement of the geothermal gradient.

4: Bottom water temperature

CTD data from a cruise in 2015 indicated a bottom water temperature of the two different areas of the study area to be 1.4°C for the deep area, and 1.645°C for the shallow area. The bottom water temperature is determined by controlling water masses moving from the Atlantic, bringing warm water northwards, while the Arctic Ocean brings cold water southwards. The bottom water temperatures during LGM are -3.582612°C for the deep area, and -3.9709076°C for the shallow area. These two temperatures are not constant during LGM, and are merely guidelines in order to simplify the model. During deglaciation, a bottom water temperature of 2°C is usually used.

5: Ice thickness

Different properties of the water column have also affected the study area. For the present day model there is only seawater, meaning that the model uses the density of seawater (1027 kg/m^3) in its calculations. Ice covered the area during LGM, and thus the density was 917 kg/m^3. The ice sheet thickness of the two locations, deep and shallow, are respectively 2088.6 m and 2109.48 m. The retreat of the ice sheet led to isostatic rebound of the seafloor during deglaciation. Hence, during deglaciation the seafloor laid at a depth of 474 m and 431 m.

5 – Results

5.1 – Seafloor furrows
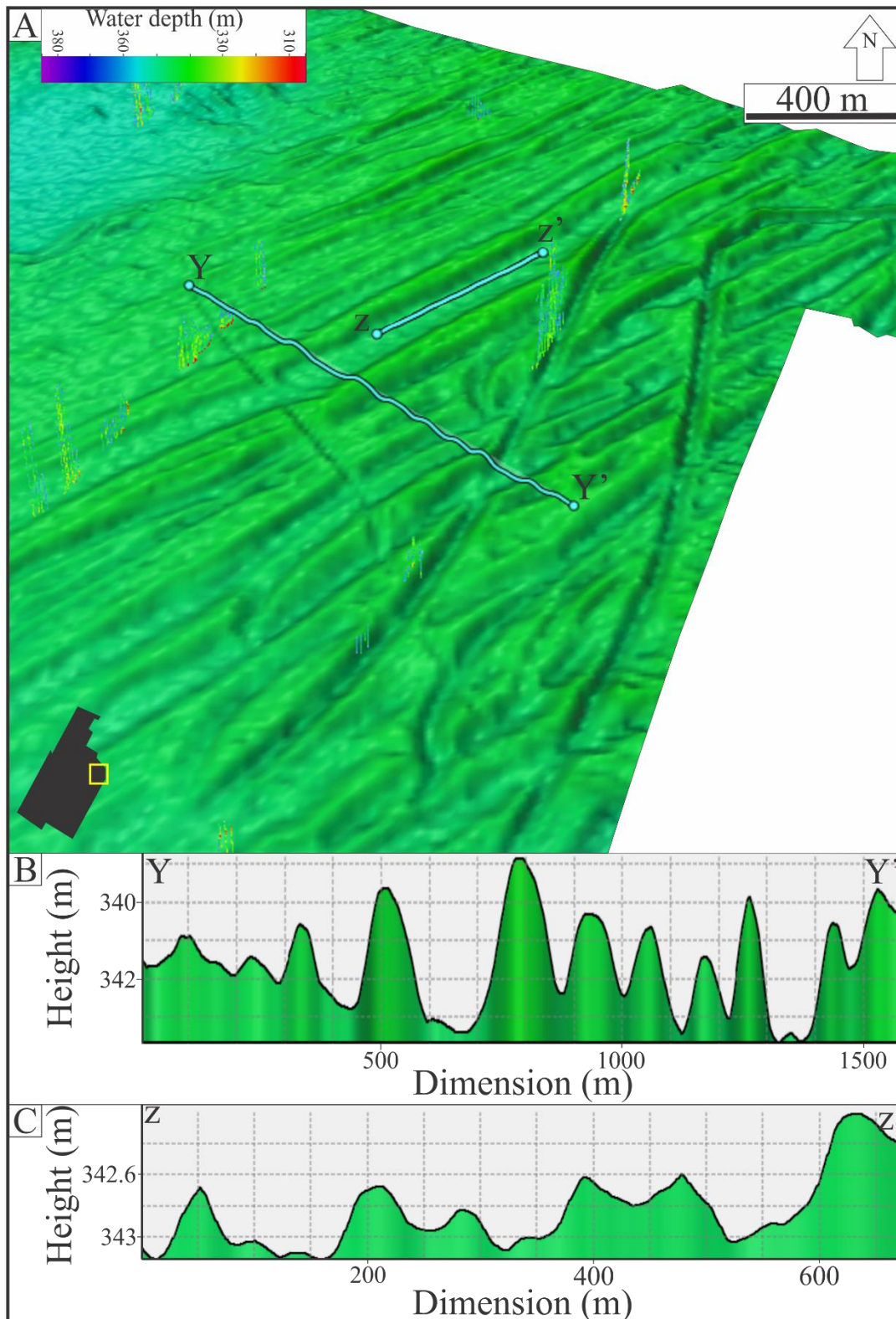
Figure 11: A: Bathymetric overview map of the seafloor furrows. B: Bathymetric profile, Y-Y', across the large furrows. C: Bathymetric profile, Z-Z', inside a large furrow. Illumination: SW-8°. Vertical exaggeration (VE): 6.

An area consisting of loads of parallel furrows are observed northeast in the study area (Fig.11). The furrows are parallel to subparallel in orientation, going from northeast to southwest. Two main furrows crosscut the others, but the main direction of them remain the same. The dimension of the furrows are partly limited, as they stretch outside of the study area. Observations show that the length range from 400 m to 4.4 km, and with a width of 40 to 200 m. The ridges on the side of the furrows range from 1-4 m in height and 40-90 m in width (Fig.11, B).

Inside the largest furrow, there are small parallel ridges with a height between 0.2-0.8 m. The ridges cross the furrow with have spacing of 75 to 200 m (Fig.11, C).

5.2 – Bedrock craters

5.2.1 – Depression overview
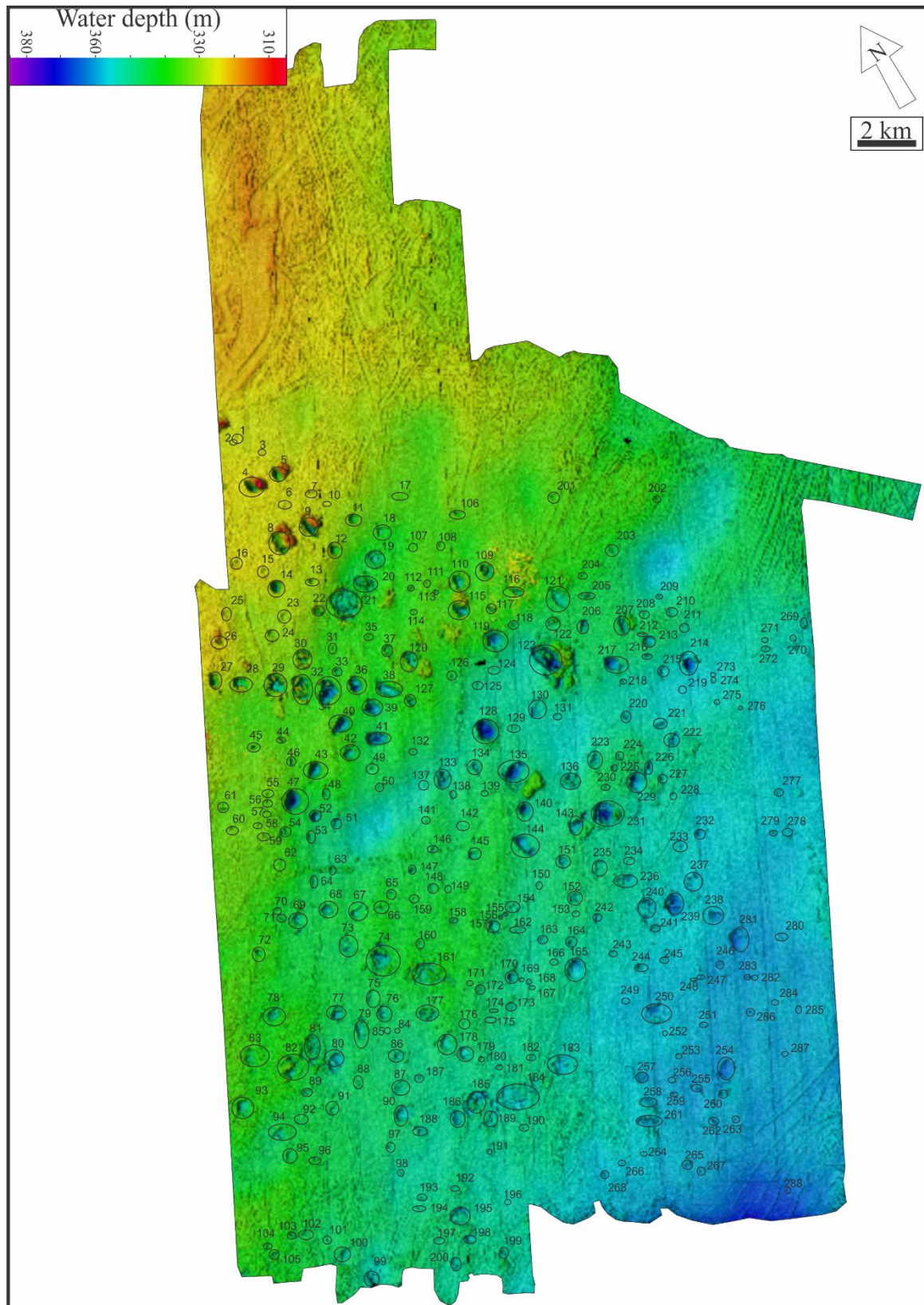
Figure 12: Overview map showing the distribution of circular depressions in the study area.

Mapping of the depressions in the study area show that there are 288 depressions. The lateral extent of each varies greatly. Mapping of the circular depressions and their properties are listed in Table 3. The shortest length across the depressions act as measurement length for the lateral dimension. Some of them will be even larger upon investigation in other directions. Mapping of the features proved difficult due to the resolution. A horizontal cell grid of 15x15m of the large area led to loss of features, as they cannot be properly distinguished from the natural topography of the area. Some of the craters counted as systems, which mean that not every single depression is marked as a distinct feature.

Circular depressions found in the study area have a lateral extent varying from 43 m (depression nr.264, Figure 12) to 906 m (depression nr.21, Fig.12). Generally, the depressions are 100-200 m wide, but with an average of 226 m. The depth of these depressions range from 0.5 m (depression nr.85, 256, 273 and 278, Fig.12) to 34 m (depression nr.123, Fig.12). The average depth of the circular depressions are 6.3 m, whereas generally they are 5 m deep. 212 (73.6 %) of the depressions are not found in relation to mounds in the area. Meaning that 76 (26.4 %) are located in close proximity to mounds. Different shapes, like circular, elliptical and semi-circular define the outline of the depression. No specific trend emerge, and the shapes seem evenly distributed, with a slight tendency towards the elliptical shape.

5.2.2 – Extent of depressions
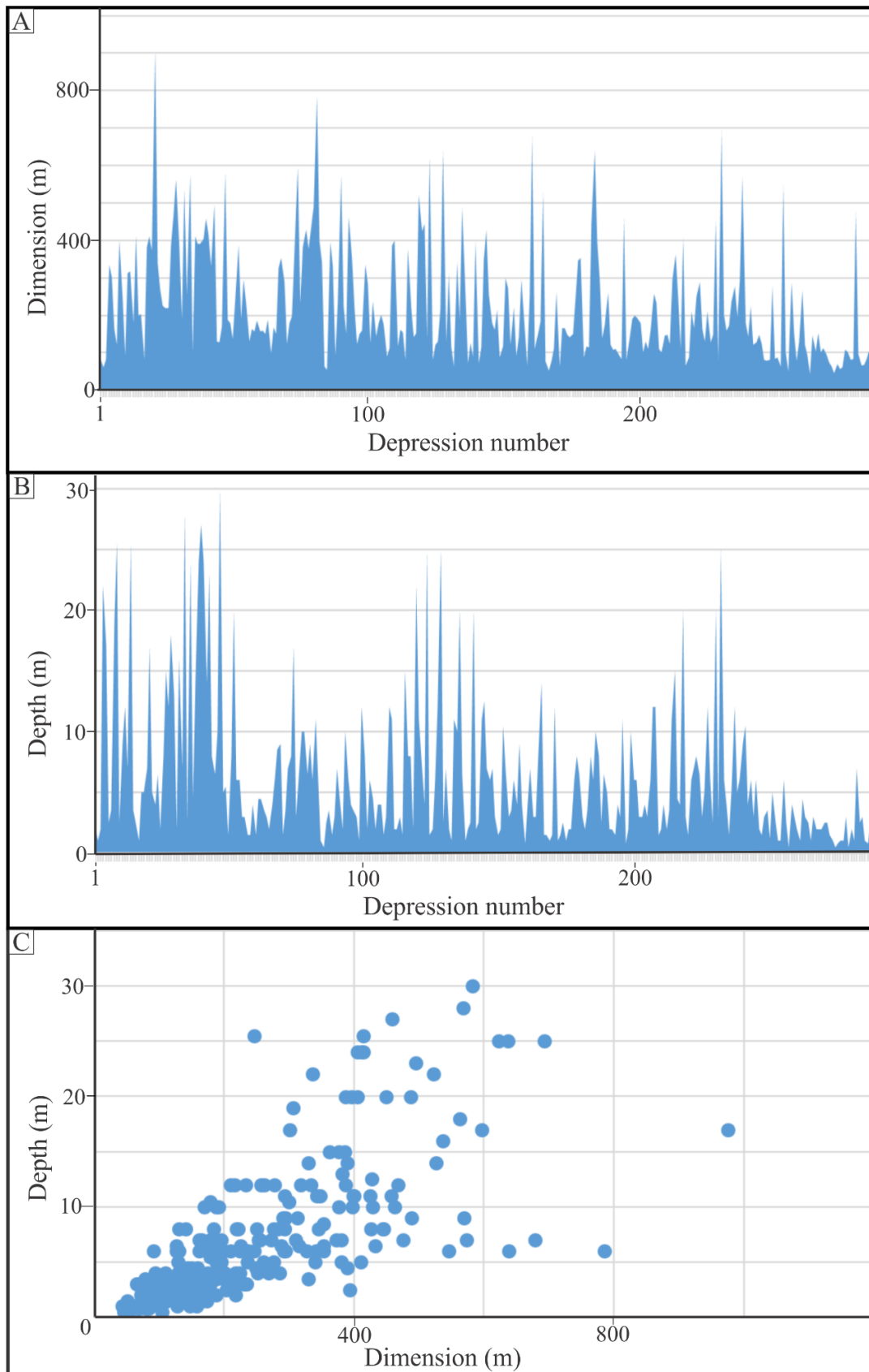
Figure 13: A) Overview of the dimension of depressions. B) Overview of the depth of depressions. C) Scatter plot of the correlation between depth and dimension.

Based on Figure 13, C, a trend in the dimensions of the depressions emerge. This line is expressed as (1):

$$Depth = 0{,}0289 * Dimension - 0{,}2489$$

Equation (1) enable us to calculate the depth of a depression if we know the diameter of it.

The circular depressions are evenly distributed throughout the study area, and there is no sign of them favouring any water depth. Regarding the size distribution, it is difficult to find any trend whether they are larger in the shallower or deeper parts of the study area. Investigating the depth of the depressions show a trend where deeper depressions favour shallower areas (Fig.13, B).

5.3 – Seafloor mounds

5.3.1 – Mound overview
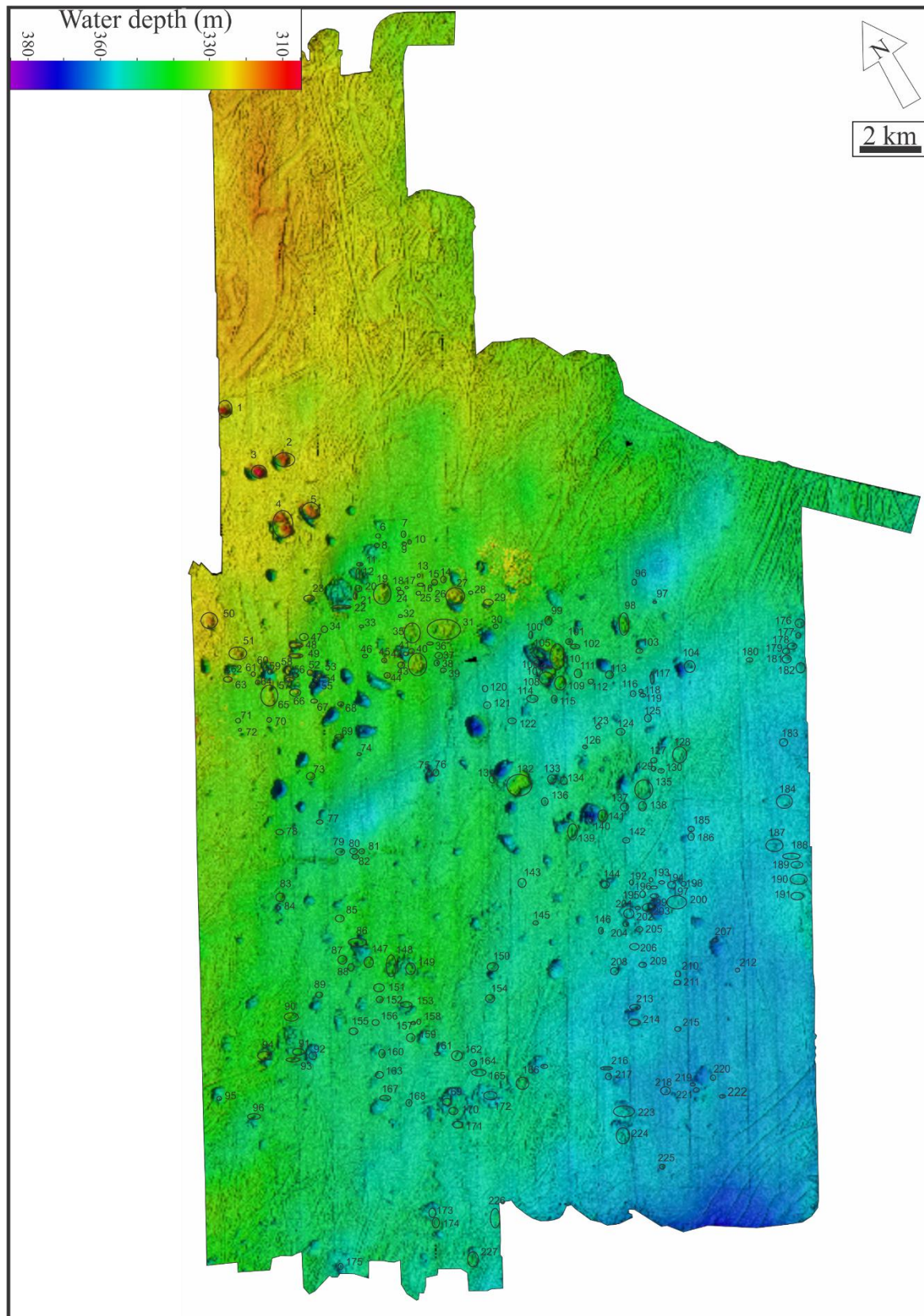
Figure 14: Overview map showing the distribution of mounds in the study area.

Mapping of the mounds in the study area show 227 elevated areas (Fig.14). The features and their properties are listed in Table 4. The short axis act as measuring length. Due to the grid resolution of the bathymetric data, loss of smaller mounds occur. Mapping the features proved more difficult than the depressions, as the mounds are generally smaller than the depressions.

The mounds typically seem much more similar to each other than the depressions. Mounds of the study area have a lateral extent ranging from 28 m (mound nr.17, 18 and 26, Fig.14), while the largest mound spread for 650 m (mound nr.35, Fig.14). The average dimension is 132 m, but with a general trend of them being smaller. Concerning elevation, the mounds range from only 0.2 m (mound nr.37, Fig.14), to 25 m (mound nr.105, Fig.14). Average elevation is 4 m, but with a clear tendency, that generally they are lower. The mounds appear mostly in proximity of depressions, with 55 % doing so, while 12 % have a possible connection with the depressions. 30 % of the mounds in proximity of depressions lay inside a depression. The shape of the mounds are the same as the depressions, with a slight favouring of the elliptical shape. The topographical shape varies from cone-shaped, rounded-cone and flat top. Cone is the least favoured shape of these, but with no specific tendency towards any of them.

5.3.2 – Extent of mounds
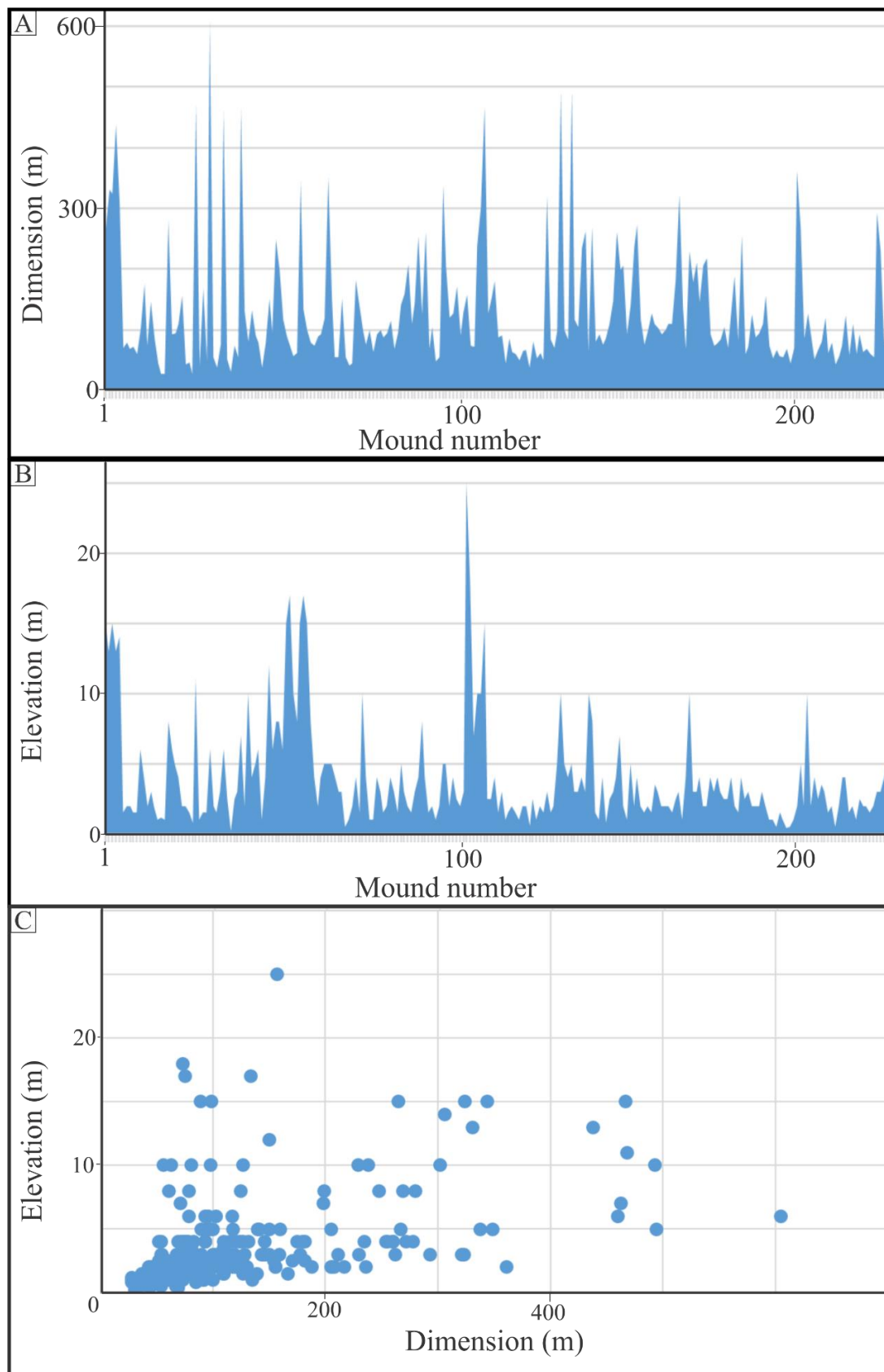
Figure 15: A) Overview of the dimensions of mounds. B) Overview of the elevation of mounds. C) Scatter plot of the correlation between elevation and dimension.

37

Based on the scatter plot of Figure 15, C a trend is visible. A linear equation of this trend turns out to be (2):

$$Elevation = 0,0158 * Dimension + 1,9014$$

Equation (2) enable us to estimate the elevation of the mounds if the dimension is stated. The trend is not as obvious as for the depressions. This means that the formula has a larger uncertainty.

Upon inspection of the distribution of mounds, there is a trend that the mounds prefer shallower water depth. However, there is no tendency of mounds favouring shallow or deep waters when it comes to the dimension. An almost even distribution is observable, where the spikes also occur evenly. Higher elevated mounds lies in the shallower areas.

5.4 – Gas flares
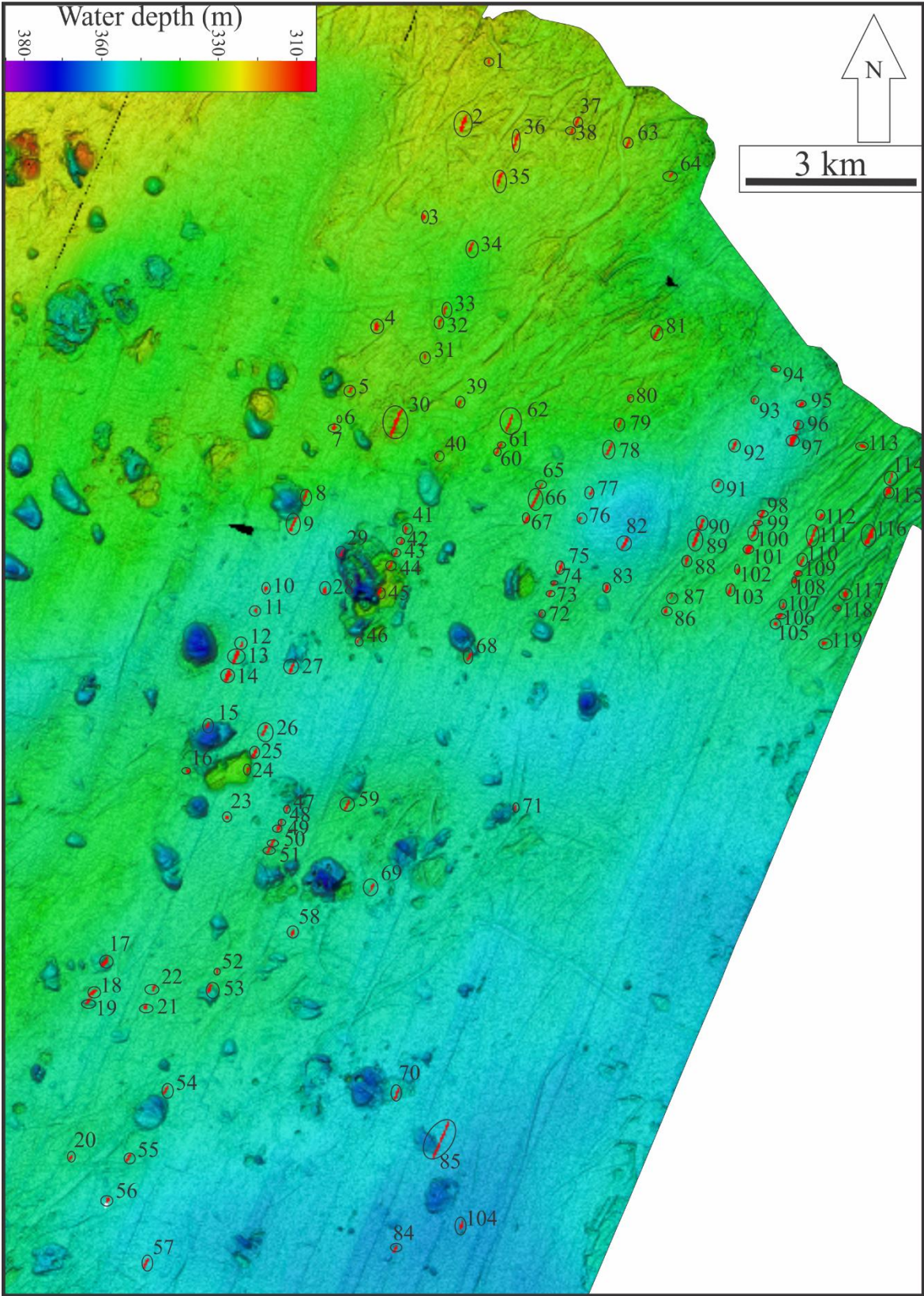
Figure 16: Overview map showing the distribution of gas flares in the study area. Marked in red for easier visualization and mapping.

Mapping of gas flares show that there are 119 flares in the study area (Fig.16). The different flares are listed in Table 5. The lowest flares are 4 m high (flare nr.38, 65 and 72, Fig.16). The tallest flare is 95 m (flare nr.17, Fig.16). Generally, the flares appear with a similar lateral extent, with a few exceptions like flare nr.85 (Fig.16).
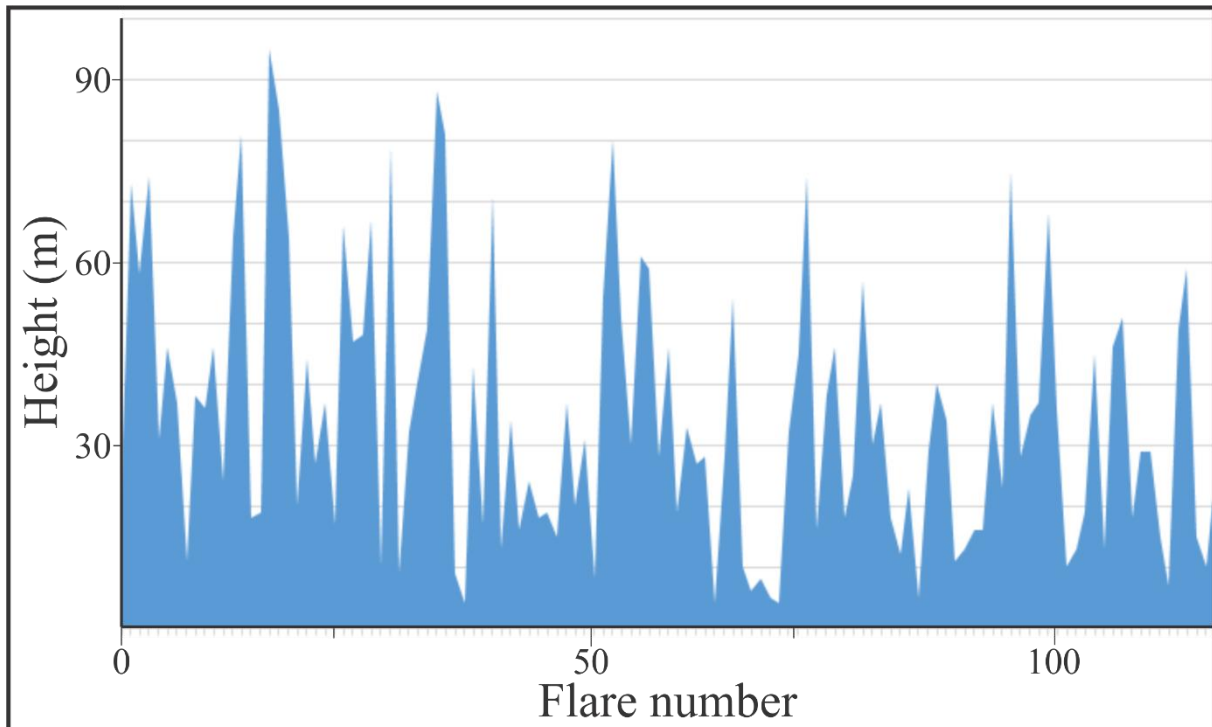
Figure 17: Overview of the height distribution of the gas flares.

The flares seem evenly distributed throughout the study area (Fig.16). Due to limited data coverage, the echosounder data only cover part of the whole study area (Fig.2). Based on the location of the flares, most of them appear in northeast, at the location of the parallel furrows (Fig.16). The craters and mounds exist with some flares inside and on them. The majority of them appear in no relation to any features. However, there are more flares at the edges and outside, than inside any features (Fig.16). The height of the different flares also appear evenly distributed, with no preference towards the shallow or deep area (Fig.17).

5.5 – Areas

The study area is divided into three regions, consisting of craters and mounds that will be more closely looked into (Fig.18). The different areas were chosen based on available seismic data from the seafloor features. Both mounds and craters are visible. The three areas lies northwest in the study area, but consist of a considerable amount of geomorphological features.
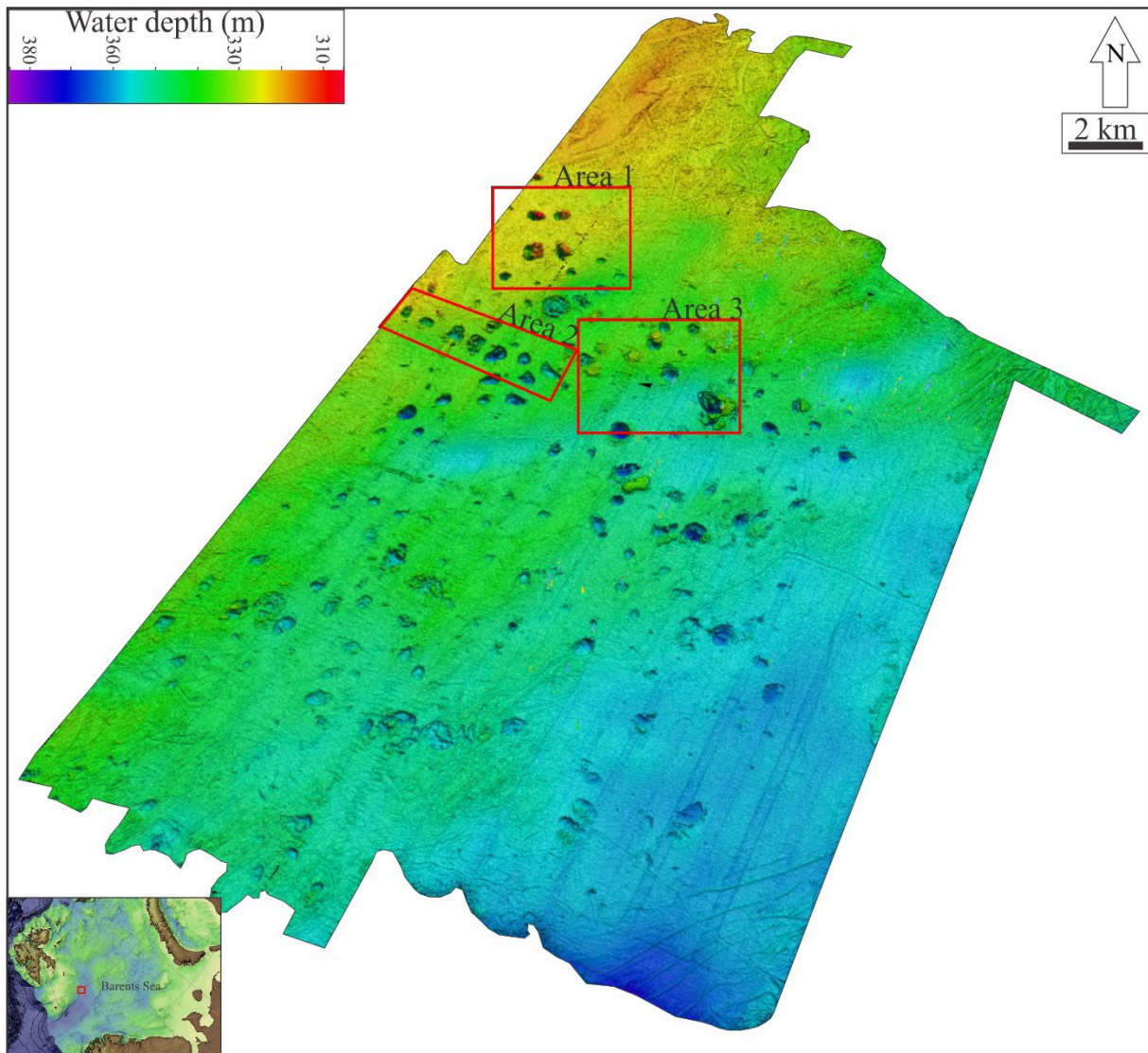
Figure 18: Overview map of the study area. Three different areas, outlined with red, are chosen to be further inspected.

5.5.1 – Area 1

Area 1 (Fig.19) lies northwest in the study area (Fig.18). It covers an area of 23.735 km^2. The water depth of the area range from 300 to 352 m. In the area, there are 13 craters and 4 mounds. Two seismic sections go across four features.
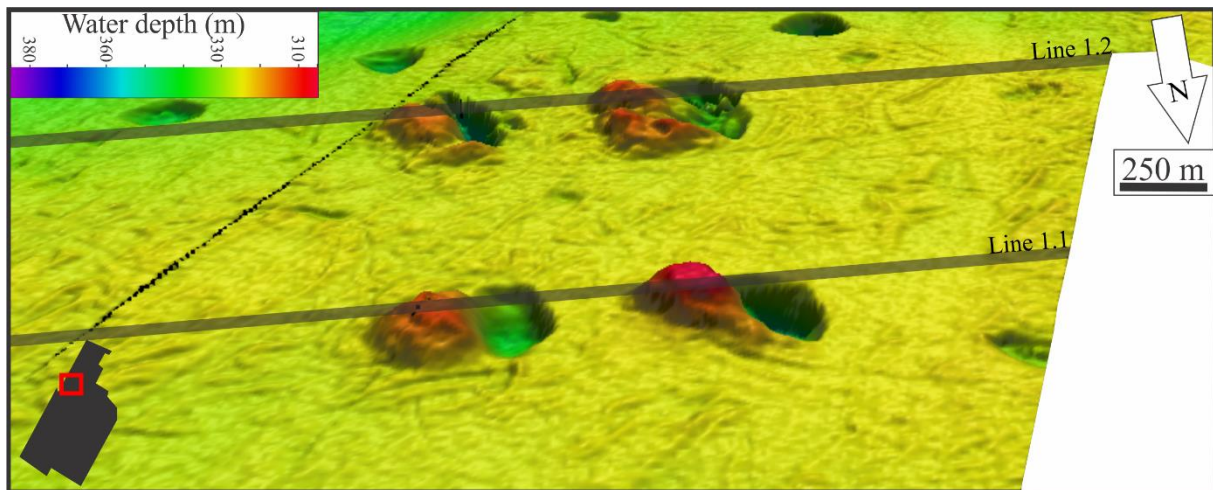
Figure 19: Overview map of area 1. Two 2D seismic lines crosscut the geomorphological features visible in this area. Line 1.1 is HH13_038_mig_deghost, and lies furthest north. Line 1.2 is745730-93Potential2, observable to the south. VE: 6. Illumination: S - 8°
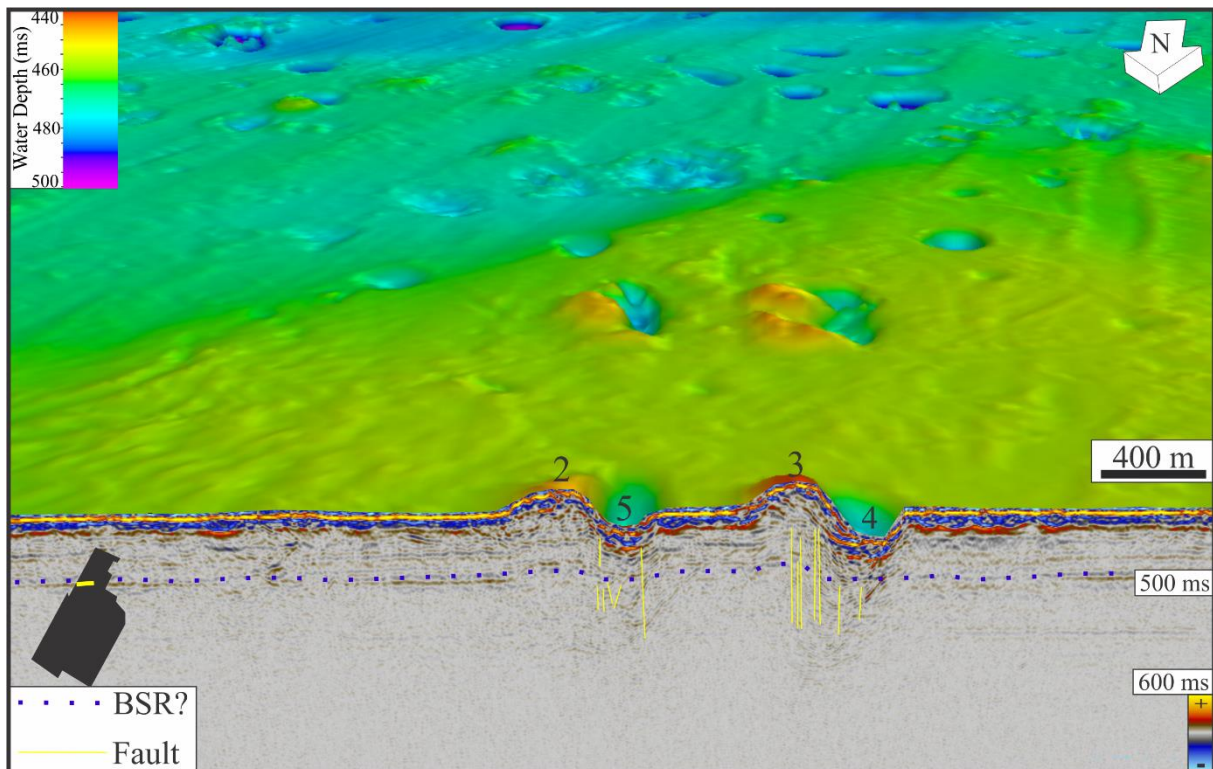
Figure 20: 3D bathymetric map, with a crosscutting 2D seismic line. The seismic line is the line HH13_038_mig_deghost collected by CAGE. The direction of the line is NE-SW. Vertical exaggeration (VE): 5. Illumination: Two sources: N - 60°. N - 50°.

Line 1.1 crosscut four features (Fig.20). These features are depressions nr.4 and nr.5 (Fig.12), and mounds nr.2 and nr.3 (Fig.14). From Table 3 and Table 4 they are respectively 336, 301, 331 and 324 m wide. They are all quite similar in appearance as they are elated in an N to S direction, and have gentle slopes.

Down to the centre of depression, nr.4 (Fig.12) there is a dip of 4° in N-S-direction. From west to east, the depression characterizes by having a higher dip than from north to south, found to be 10°, and ending in a depression 22 m below the seafloor. The corresponding mound is 13 m high, with a gentle slope to the north, 2°, and a steep slope to the south, 7°. A flat plateau mark the top of the mound, and the slopes in W and E direction are 7° and 5° respectively.

The eastern crater and corresponding mound have the same direction as the previous feature (Fig.20). The depression is 17 m deep, and has the same dip of 4° in N-S direction. That means the same as for depression nr.4. From E-W, there is also a slightly steeper dip, estimated to be 7-10°. Mound nr.3 (Fig.14) is 15 m high, with a flat plateau on the top. The slope towards the highest point of the mound is 3° from north, 7° from south, 3° from east and 8° from the crater side.

The seismic line (Fig.20), HH13_038_mig_deghost, shows the sediments under the features. Due to use of high frequencies during collection of the data, the penetration of the seismic is low, reaching only 700 ms down. From the seismic section (Fig.20), there may be a slight tendency towards some stronger reflectors directly underneath the features. Underneath the craters and mounds, there are several visible faults. They stretch from around 550 ms and up to the seabed. The faults may be even longer, but since the resolution is poor, it is hard to tell.

Upon inspection, the seabed reflector is a continuous reflector. However, the seabed reflector at the geomorphological features are only slightly distorted for the mounds, whereas the craters are more discontinuous.

5.5.1.2 – Line 1.2

Figure 21: 3D bathymetric map, with a crosscutting 2D seismic line. The seismic line is the line 745730-93Potential2.The direction of the line is NE-SW. VE: 5. Illumination: Two sources; N - 60°, N - 50°.

The second line of area 1 crosscut four features (Fig.21). These are depression nr.8 and nr.9 (Fig.12), and mound nr.4 and nr.5 (Fig.14). Similar to the features from Figure 20, these are also oriented in an N-S direction. The features are more complex than the previous ones. This is observable in the bathymetric data, as the topography of the features are more variable.

Depression nr.8 has a depth of 19 m, and a width of 306 m along the shortest axis (Fig.21). Here, the dip is 10°. The long axis is 850 m, with a gentle dip of 2° to the north, and 5° to the south. Inside the depression, there is an elevated area of 6 m, which has rounded shape. Several other small mounds are observable that only reach 1 m above the seabed. Associated with depression nr.8, mound nr.4 stretch 13 m above the general seafloor. It can be split into two mounds, which seem to have grown together. However, it is interpreted as one mound. The width of the feature is 438 m, and has a length of 901 m. A dip of 3° to the north, 2° to the east, 2° to the south, and 3° to the east indicate a generally gentle mound.

Depression nr.9 and nr.5 are located east of depression nr.8 and nr.4 (Fig.12, 14). Depression nr.9 is a relatively thin elongated depression (Fig.19). The short axis is 246 m, while the long axis is 880 m. A dip of 3° from the north, 4° from the south, 18° from the west and 14° from the east lead down to the lowest point of the depression of 25.5 m below the seabed.

Mound nr.5 (Fig.14) is a feature with a flat plateau on the top. It reach 14 m above the seabed. The short axis, with a length of 306 m, has a dip of 8° to the east and 5° to the west. The long axis is 767 m long and has a dip of 5° to the south, and 2° to the north.

On the seismic section (Fig.21), collections of faults are visible underneath depression nr.9 and mound nr.5. One region of sediment packages are dipping westward from between 600ms to 1000 ms. At the lowermost end of this section there is a pull-up of the reflectors. At the edges of this pull-up-effect, there is a slight blanking area, leading further up to the faults. Towards the deeper parts of the seismic section there are several vertical to sub-vertical distortions of seismic reflectors. These are mainly based underneath the seafloor features.

Figure 22: 3D bathymetric map, with a crosscutting 2D seismic line. The seismic line is the line 745730-93Potential2. The seismic attribute envelope is applied on the seismic line. VE: 5 Illumination: Two sources; N - 60°, N - 50°. The red arrows indicate the possible migration pathway of hydrocarbons.

The seismic attribute envelope (Fig.22) shows the reflection strength. It is a seismic attribute sensitive to acoustic impedance change. Hence, its usage extend to show lithological change, porosity change, thin-bed tuning and the presence of hydrocarbons (Chopra and Marfurt, 2005). For the purpose of this seismic section, it mainly show the possible migration paths of hydrocarbons. Fluids migrating in the subsurface tend to move horizontally when hitting a new layer. This is due to the permeability change when going to another sediment package.

Several layers of higher reflection strength are observable (Fig.22). These are mainly located at large depths, and follow trends seen in the reflection amplitude seismic section (Fig.21). At depths around 2000 ms, there is a larger degree of distortion and masking of the seismic signal underneath the geomorphological seabed features (Fig.22). In between this masking, there are local areas of higher amplitude. Based on the vertical distortions seen in Figure 21, the

amplitude anomalies observed in Figure 22 may be related to the migration of hydrocarbons towards lower pressure, and the seabed.

5.5.2 – Area 2

Area 2 is an area of 16.53 km^2 (Fig.23). The water depth range from 318 to 366 m. In this area, there is a total of 10 depressions and 24 mounds. Mapping two depressions with the seismic line 2737-89-LS, seven of the depressions with a bathymetric profile (Fig.23), and two depressions with the seismic line 7455-87-WPotential1.
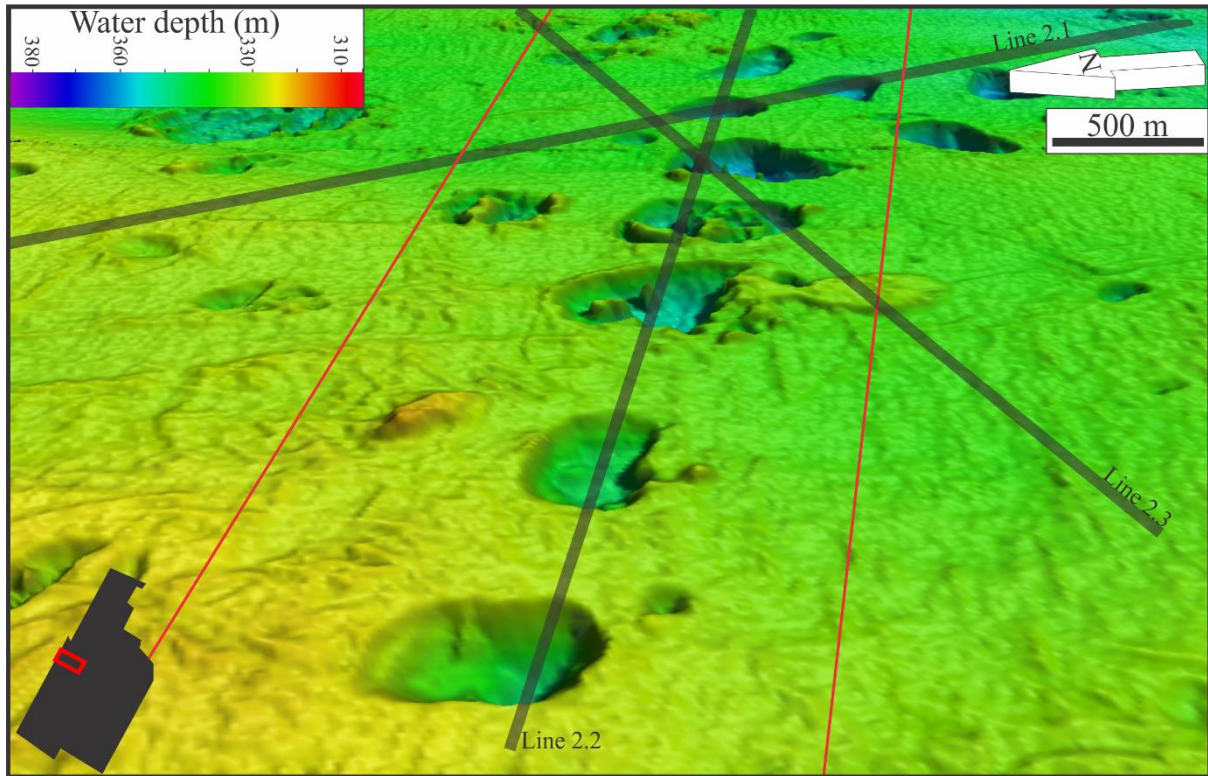
Figure 23: Overview map of area 2. The area is located southwest of area 1. Three lines crosscut geomorphological features visible in the area. Line 2.1 is 2737-89-LS located east in the area. Line 2.2 refers to a bathymetric profile. Line 2.3 refers to the seismic section 7455-87-WPotential1. VE: 6. Illumination: S - 8°.
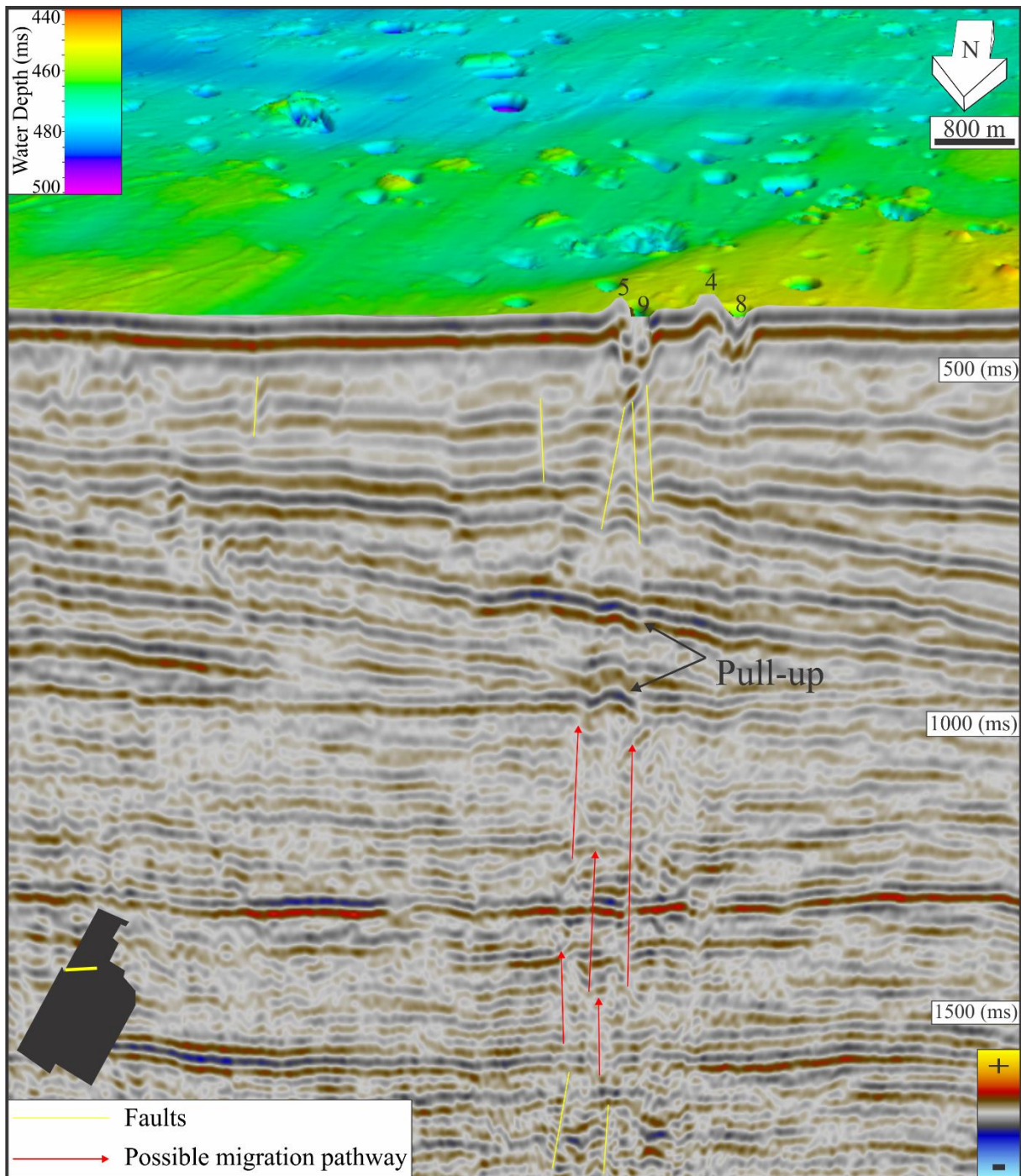
5.5.2.1 – Line 2.1

Figure 24: 3D bathymetric map, with a crosscutting 2D seismic line. The seismic line is the line 2737-89-LS. The direction of the line is from N to S. VE: 5. Illumination: Two sources: NW - 60°, N - 50°.

The seismic line crosscut two depressions. These are depression nr.36 and nr.39 (Fig.12). Depression nr.36 is 411 m wide and 598 m long, with an N-S direction (Fig.24). It is a smooth depression, with two small internal features, each 3 m high. The depression is 24 m deep. A dip of 3° to the north, 7° to the south, 7° to the west and 5° to the east, lead down to the deepest point of the crater.

Depression nr.39 is 405 m wide and 607 m long. It has the same direction as depression nr.38, and shows no sign of internal features (Fig.24). A dip of 5° to the north and south, 9° to the west and 5° to the east, lead down to the deepest point 24 m below the seabed.

In the seismic section (Fig.24), there are several distortions in the reflectors, which are marked as possible migration pathways. These are especially located underneath the geomorphological features. In contrast to the distortions in the surrounding area, the distortions underneath the bedrock craters seem to have a possible migration path towards the seabed. The surrounding areas tend to have distortions ending some place in a reflector. In addition, there are few to no signs of masked reflectors.
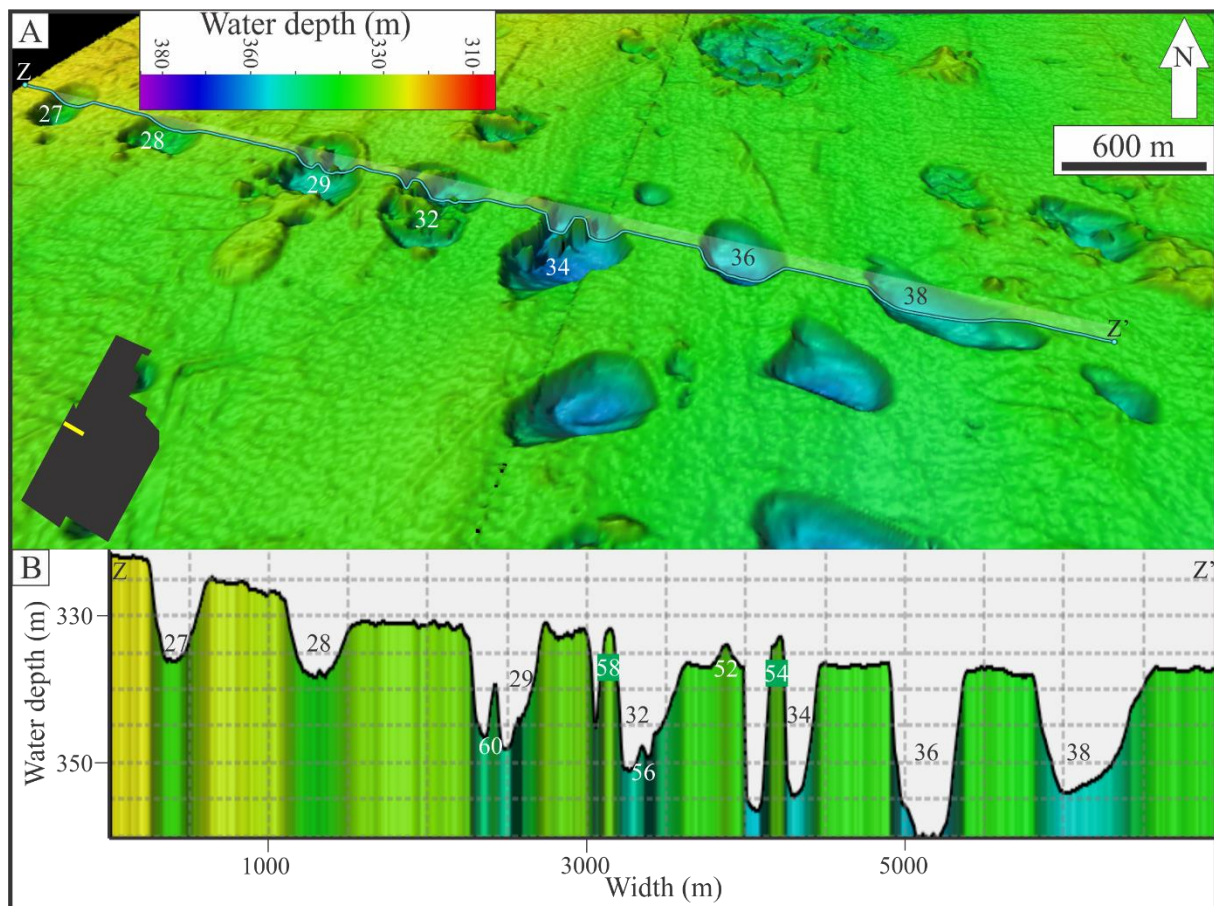
Figure 25: A: 3D bathymetric map, showing the seven depressions. B: Bathymetric profile across the seven depressions.
VE: 6

Line Z-Z' (Fig.25, A) shows the location of the bathymetric profile (Fig.25, B). It passes seven large depressions northwest in the study area. The depressions are number 27, 28, 29, 32, 34, 36 and 38 (Fig.12). In addition, mounds number 52, 54, 56, 58 and 60 are visible in the bathymetric profile (Fig.25, B).

The depth of the different depressions are 15 m (nr.27), 12 m (nr.28), 18 m (nr.29), 16 m (nr.32), 28 m (nr.34), 24 m (nr.36) and 14 m (nr.38), while the mounds are 6 m (nr.52), 17 m (nr.54), 8 m (nr.56), 17 m (nr.58) and 8 m (nr.60). They range in size from 386 to 568 m for the depressions, and 61 to 134 m for the mounds, and most of them have an elliptical shape. Typically, the depressions have steep slopes in the west to east direction, and a gentler slope from north to south. The slopes are generally in the range of 3-6°, but for depression nr.34 slopes of 12 and 15° were found for the northwest and southeast slope, respectively. Being by far the steepest slope of area 2.

The mounds of the area show a variety of shapes, from flat to cone-shaped, and no preferred appearance exist. From the main depressions, a few mounds reach above the seafloor. Generally not more than 2-3 m above the seafloor. The mounds appear to reach above the seabed if they are large lateral features. Otherwise, the only possibility for them to reach the seabed is if they are part of a larger feature inside the crater.
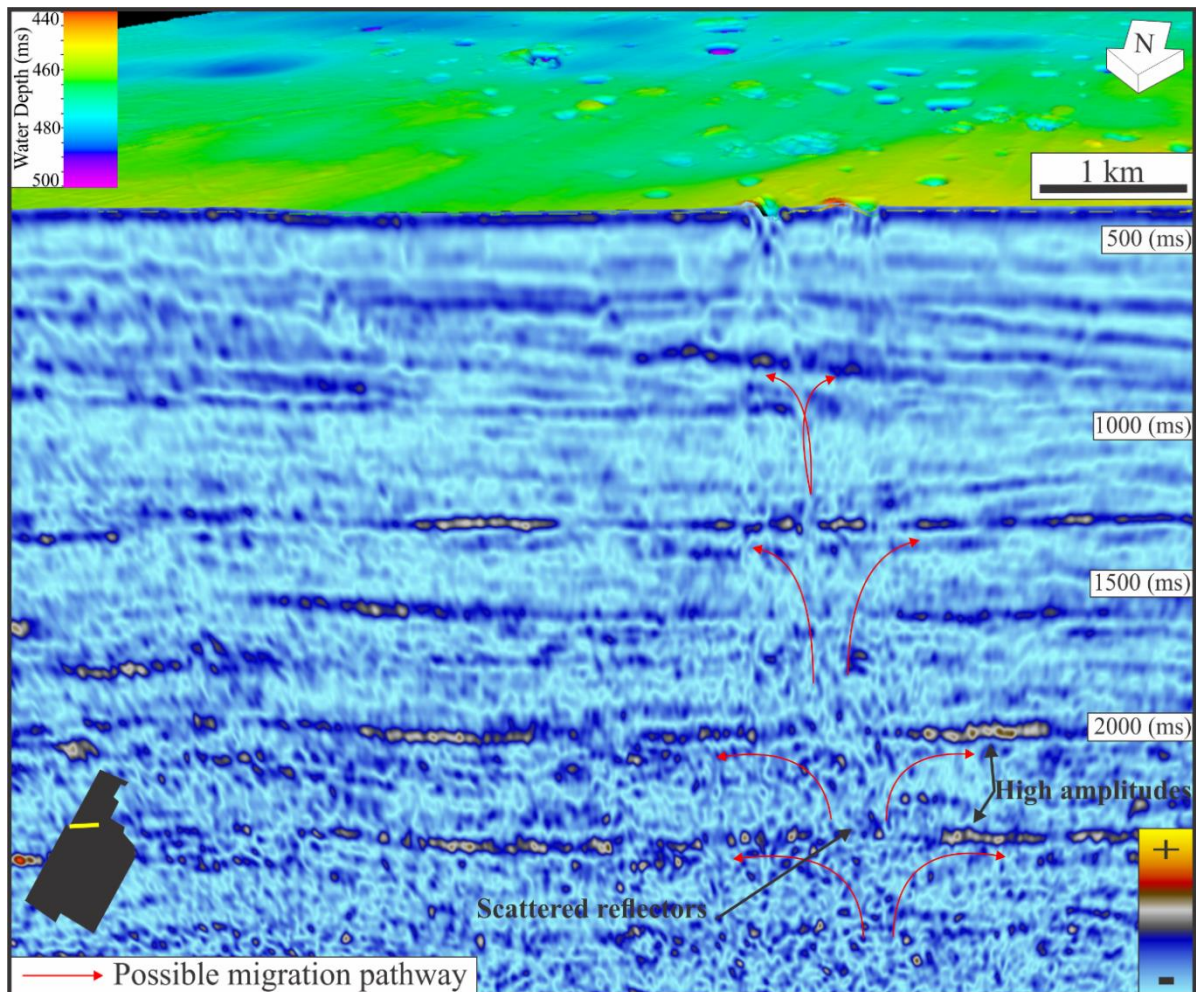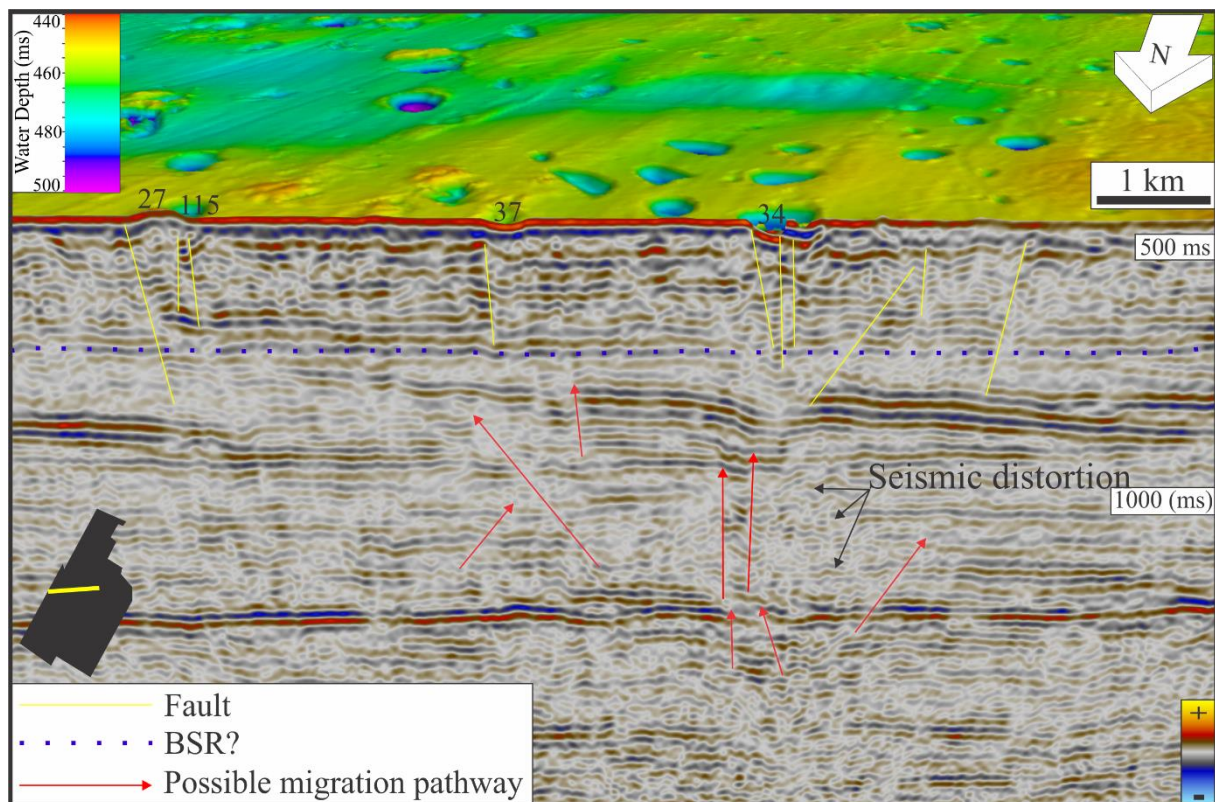
Figure 26: 3D bathymetric map, with a crosscutting 2D seismic line. The seismic line is the line 7455-87-WPotential1. The direction of the line is W-E. VE: 5. Illumination: Two sources: N - 50°, S - 60°.

The seismic section (Fig.26) is the line 7455-87-WPotential1. It shows one of the seven depressions, more precisely depression nr.34. The crater is described in the previous section, and it has been established that it is has the steepest slopes in area 2 (Fig.23). The seismic section show several large faults close to the seabed. In addition, there are vertical distortions of the seismic reflectors visible at a two-way travel time of 1300 ms, marked as possible migration pathways.

Previously, the subsurface distortions occur underneath the seabed features, which is also the case here. The largest degree of change of reflectors appear underneath depression nr.34. Whereas for the other depressions, depression nr.37, there are fewer possible migration pathways and faults. This depression is shallow and only 4.5 m deep. The lateral extent of it is 390 m, and it has slopes of 0-2°.

5.5.3 – Area 3

Area 3 (Fig.27) lies slightly north of the centre of the study area. The water depth of the area varies from 326 to 374 m. The size of the area is 28 km^2. Mapping of geomorphological features of the area show 19 depressions and 34 mounds. In addition, 22 gas flares lies in the area. The different lines crosscut respectively two mounds and a depression, a mound and the large complex.
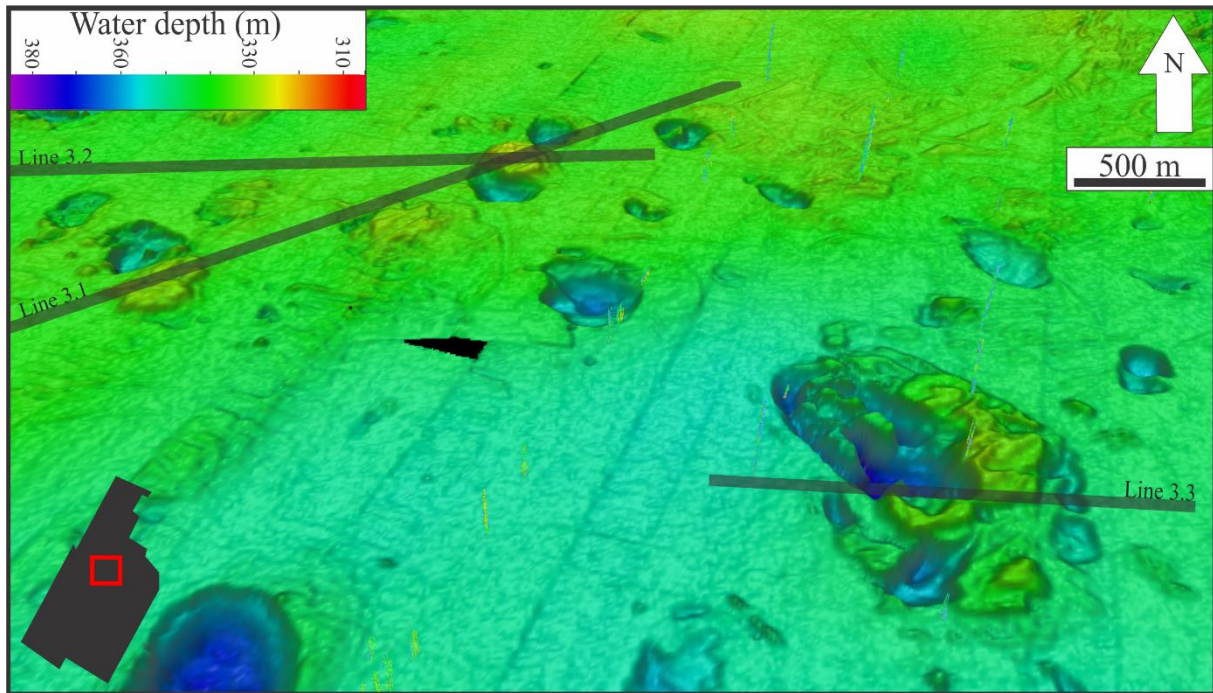
Figure 27: Overview map of area 3. Three lines crosscuts the geomorphological features visible in the area. Line 3.1 refers to the Cage15-5-001. Line 3.2 refers to the seismic section 7455-87-WPotential1. Line 3.3 is a bathymetric profile. VE: 6. Illumination: S - 8°.
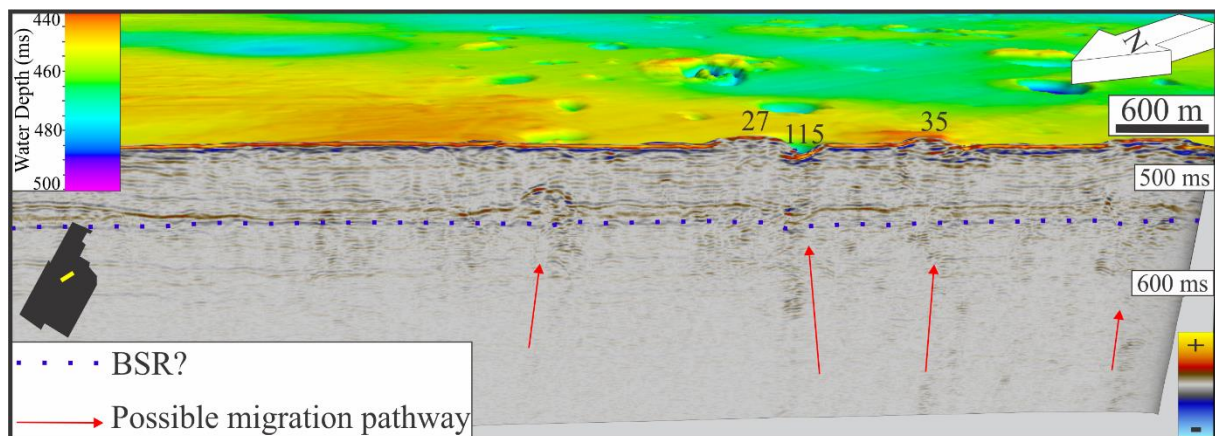
Figure 28: 3D bathymetric map, with a crosscutting 2D seismic line. The seismic line is the line Cage15-5-001. The direction of the line is from SW to NE. VE: 5. Illumination: Two sources: W - 55°, NW - 60°.

The seismic section (Fig.28) crosscut two mounds and one depression. These are located north in area 3 (Fig.27). Mound nr.27 and nr.35, as well as depression nr.115 are those features that Figure 28 covers. Depression nr.115 is 15 m deep and 377 m wide. It has a semi-circular shape, and the long axis is 603 m. No internal features are observable, and the slopes are 3° to the north, 4° to the south, 4° to the west and 6° to the east. Associated with the depression mound nr.27 appear, which lies east of the depression. This contribute to a steeper slope in this direction.

Mound nr.27 is 11 m high, and has a flat top (Fig.28). It is 468 m wide and 640 m long. Giving an elliptical shape. The slopes towards the highest point are generally 2-3°, with the western side being steeper as the depression lies here. The second mound is mound nr.35. This is 6 m high, 460 m wide and 540 m long. Calculation show that the slopes are from 1° to 3°.

Observation of the seismic section (Fig.28) show a lack of deep penetration from the seismic. Underneath the seabed features, vertically there are slightly stronger reflectors. In the subsurface, at around 520 ms, there is an elevated reflector. Beneath this, there is also slightly stronger reflectors in the vertical section.
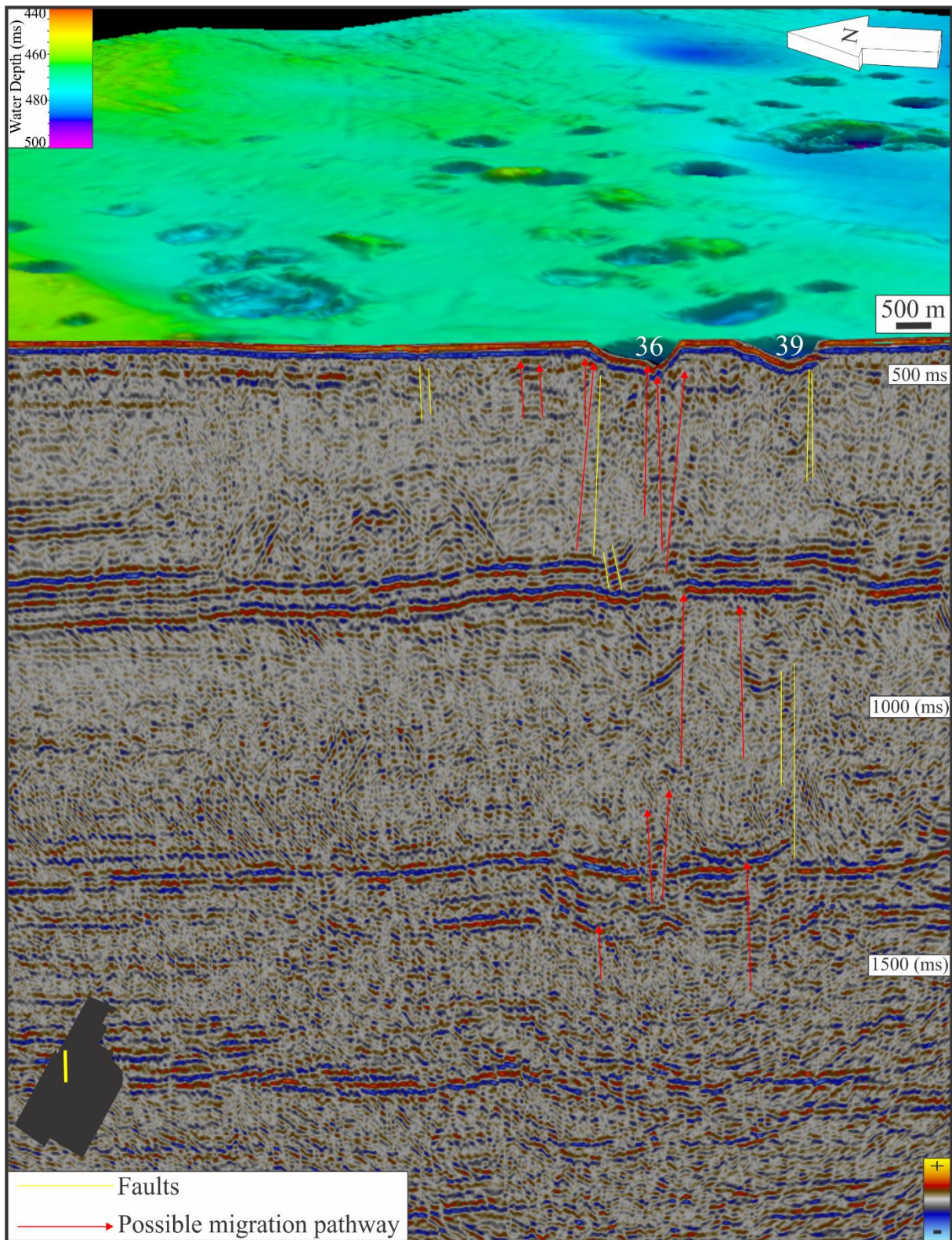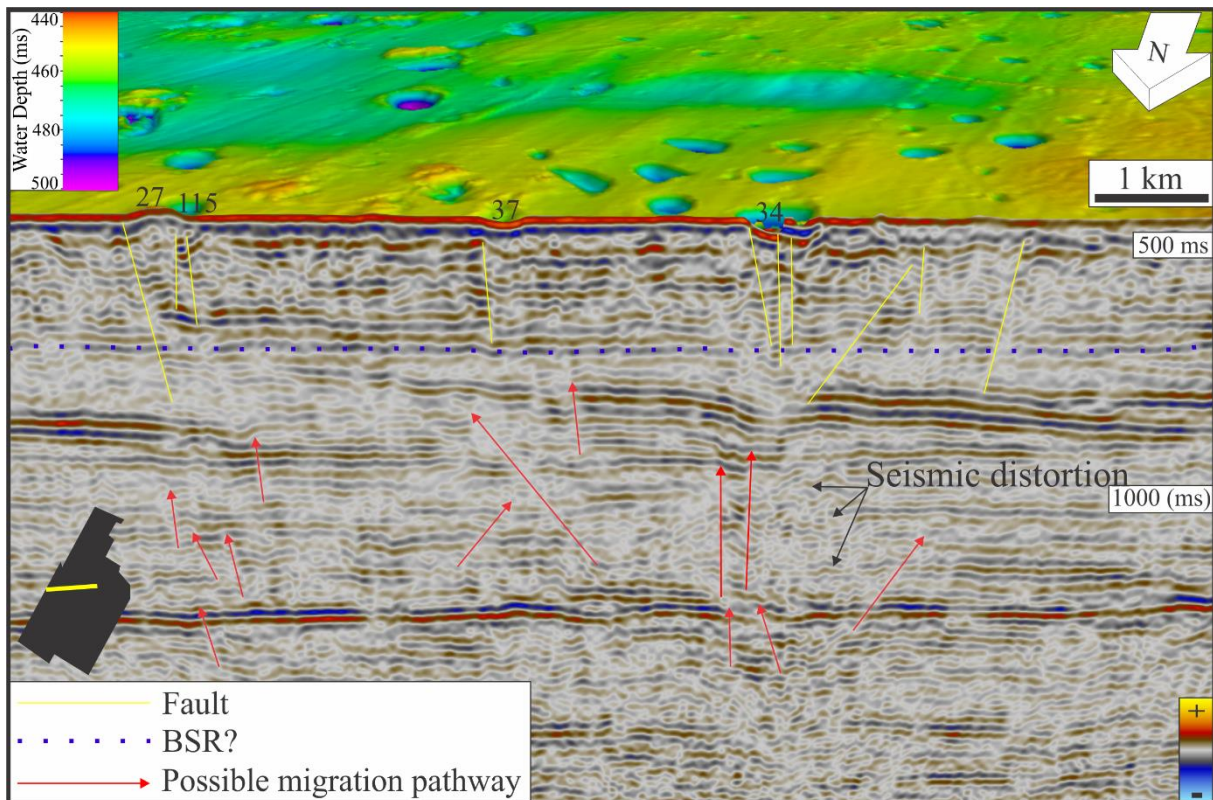
Figure 29: 3D bathymetric map, with a crosscutting 2D seismic line. The seismic line is the line 7455-87-WPotential1. The direction of the line is from W to E. VE: 5. Illumination: Two sources: N - 50°, S - 60°.

The feature of interest is mound nr.27 on the seismic section to the left (Fig.29). It is previously described in the section 5.5.3.1. As the seismic penetration in Figure 28 was limited, a seismic section of better penetration is shown here (Fig.29). Underneath the mound, there are several faults that stretch for 300 ms. At larger depths there are several small, vertical distortions of the seismic reflectors, marked as possible migration pathways. These vary from 80 ms to 400 ms in length.
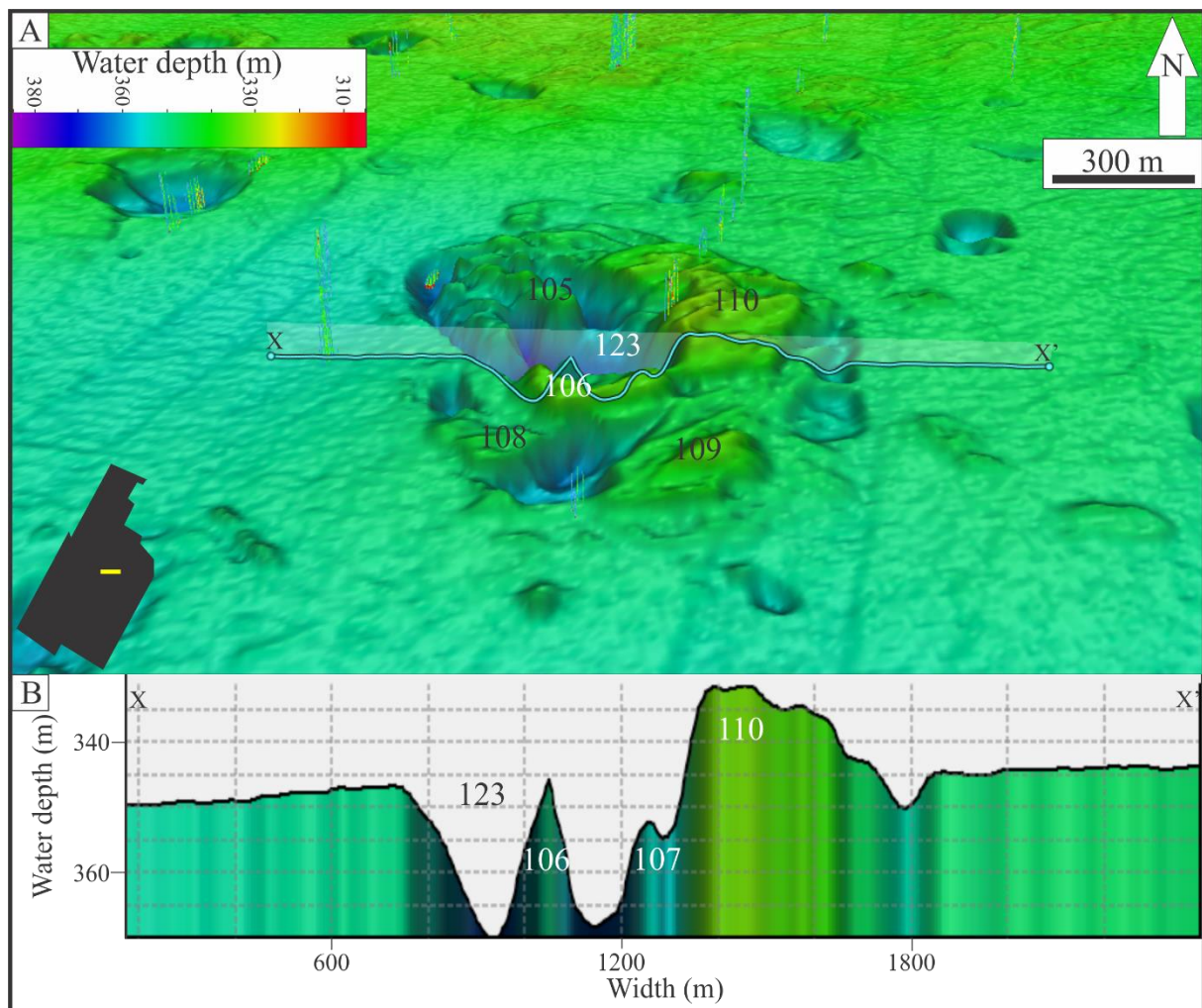
Figure 30: A: 3D bathymetric overview of depression nr.123. B: Bathymetric profile trough line X-X'. VE: 6.

The complex observed in Figure 30, A, is the largest of the study area. It consists of a large depression, surrounded by four smaller depressions. Inside the main depression, there are two small mounds, and a large horseshoe-shaped mound. On the rim of the depression there is a mound going from the northeastern side and round to the southwestern side. Associated with the surrounding depressions there are also smaller mounds, which contribute to the whole complex being 1.98 km long and 1.5 km wide.

Depression nr.123 is 25 m deep (Fig.13, 30, B). The width of the main crater is 623 m, and it has a length of 1165 m. Towards the deep centre of the crater the slopes are 3° to the north, 5° to the south, 9° to the west and 7° to the east. The surrounding depressions range from 6 to 15 m, and are 72 to 212 m wide along the shortest axis.

The observed mounds are nr.105-110. They are 25 m high (nr.105), 18 m (nr.106), 7 m (nr.107), 10 m(nr.108), 10 m (nr.109) and 15 m (nr.110). The width of them are 157 m (nr.105), 73 m

(nr.106), 71 m (nr.107), 238 m (nr.108), 302 m (nr.109) and 467 m (nr.110). Two out of three of those mounds observed inside the main depression reach above the seabed. All of the mounds are flat, as the top of them typically only have a few scours to differ the topography from a flat plateau. The differing mound is mound nr.106 (Fig.30, B), which has the shape of a cone.

5.5.3.4 – Gas flares
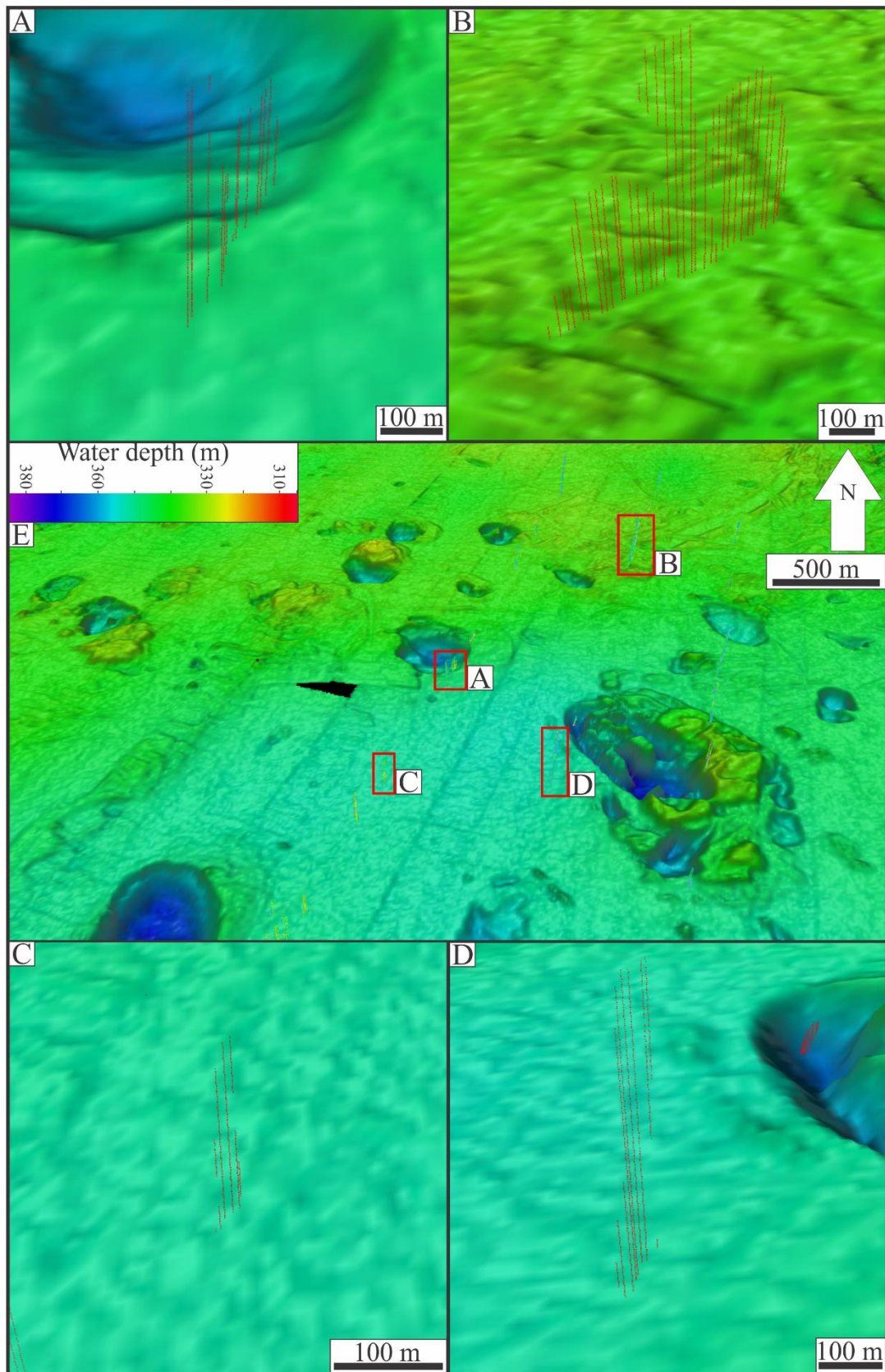
Figure 31: A-D: Bathymetric map view of four selected gas flares. E: Overview map of area 3, with the marked locations of the selected gas flares. For visualization purposes, the gas flares are red.

The four selected flares are A: nr.9, B: nr.30, C: nr.28, D: nr.10 (Fig.16, 31). Respectively, they are 38, 79, 67 and 36 m high. Sampling of data was in one direction, hence the dimension of the flares are just in one direction. The different flares are respectively 273, 510, 111 and 70 m long (Fig.31). The longest lies at a slightly elevated area at the end/beginning of a furrow (Fig.31, B), while one lies at the edge of a crater (Fig.31, A), and the last two lays on the generally flat seafloor (Fig.31, C, D).

5.5.4 – Gas hydrate stability zone models

5.5.4.1 – Gas hydrate stability zone-model at LGM
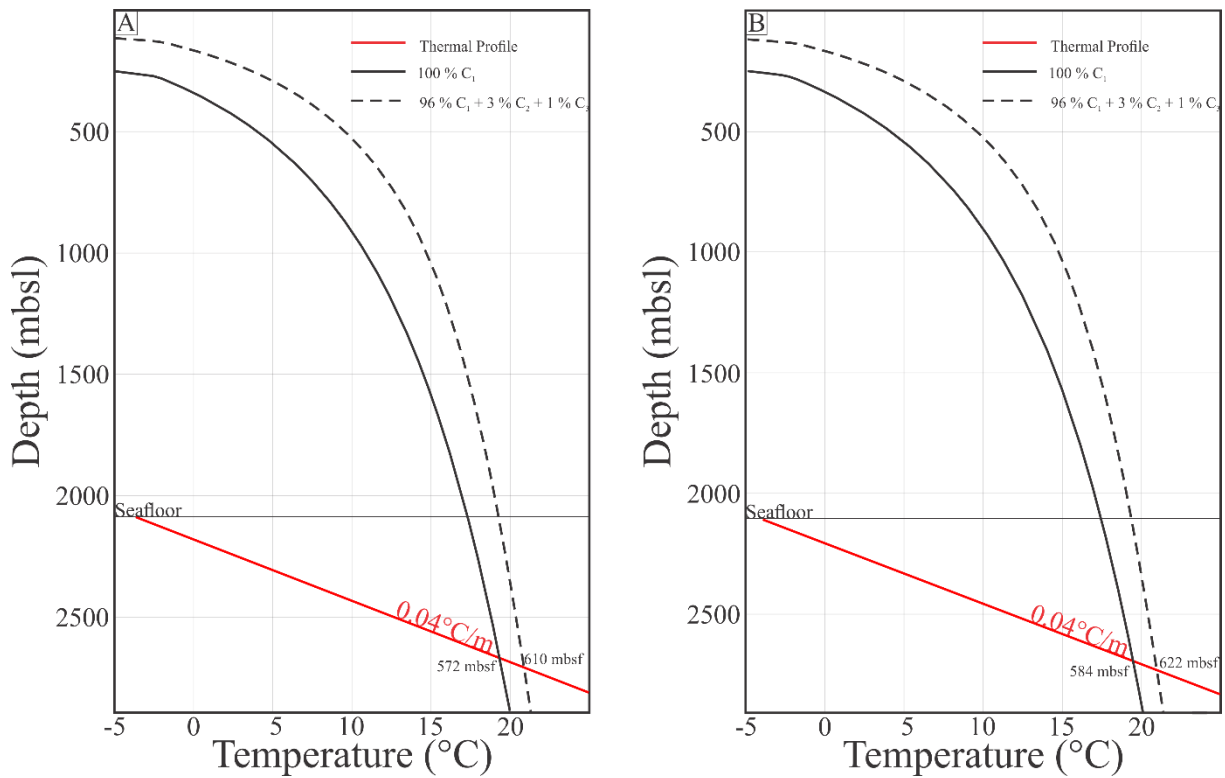
Figure 32: A) Model of the deep part of the study area during LGM. The horizontal line indicates the seafloor at the time, while the red indicates the geothermal gradient, which decreases with depth. The dotted line indicates the stability curve for mixed gas composition, and the covered line indicates the stability curve for the 100 % methane composition. B) Model for the shallow part of the study area during LGM.

The model depicts at what depths gas hydrates are stable (Fig.32). At the point where the stability curve and geothermal gradient crosscut, the hydrates are stable in the subsurface at the conditions above the geothermal gradient and below the seafloor. Based on this, gas hydrates consisting of 100 % methane are stable down to 572 m below the seafloor in the deep part of the study area (Fig.32, A), while those of mixed composition are stable down to 610 m below the seafloor.

In the shallow area (Fig.32, B), the 100 % methane hydrates are stable at even larger depth, 584 m below the seafloor, while the mixed are stable down to 622 m below seafloor. The increase of the stability zone from the deep to the shallow contradict logic. However, due to an increased ice sheet thickness in the shallow area, as well as colder bottom water temperature, the model show a reasonable result.

5.5.4.2 – Gas hydrate stability zone-model during deglaciation
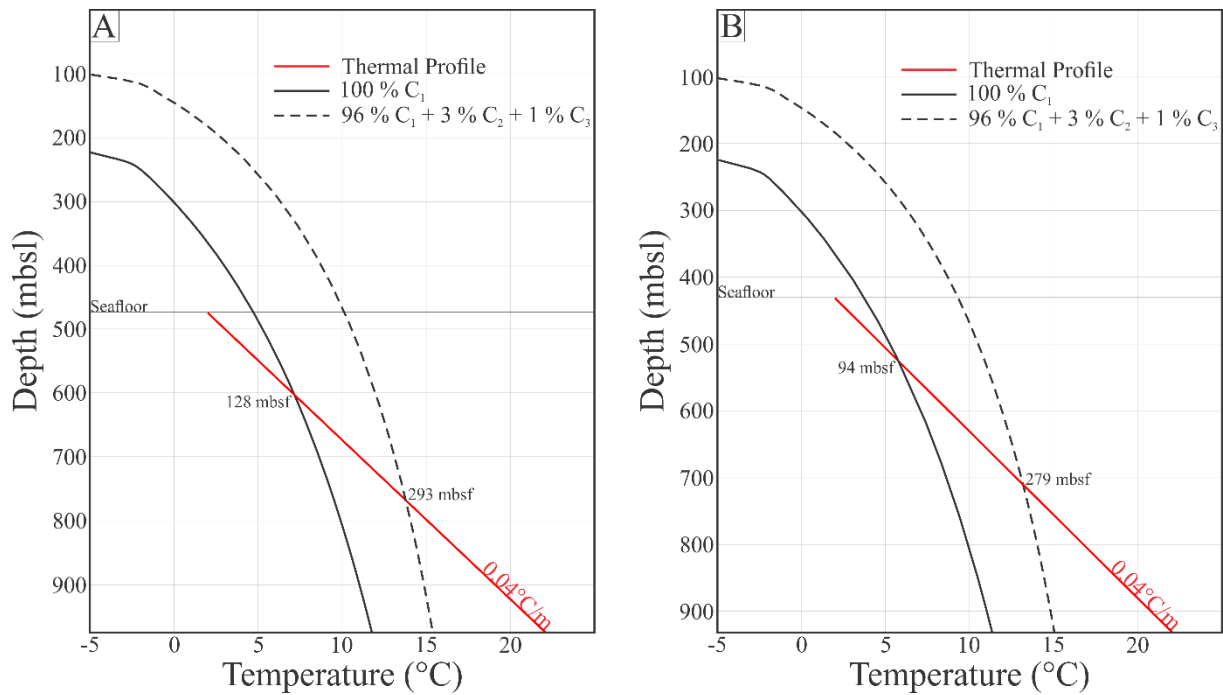
Figure 33: A) Model of the deep part of the area during deglaciation. B) Model of the shallow part of the area during deglaciation.

During deglaciation, the seafloor lied at shallower depth. In addition, the ice-free conditions implies both a higher bottom water temperature as well as different properties of the overburden material. The change result in a thinner gas hydrate stability zone, found to be 128 m below seafloor for 100 % methane in the deep area (Fig.33, A), and 293 m below seafloor for mixed composition of gas (Fig.33, A).

At the shallow seafloor (Fig.33, B), the stability zone is even thinner, and here at 94 m below seafloor for 100 % methane, and 279 m below seafloor for the mixed composition.

63

5.5.4.3 – Gas hydrate stability zone-model at present day
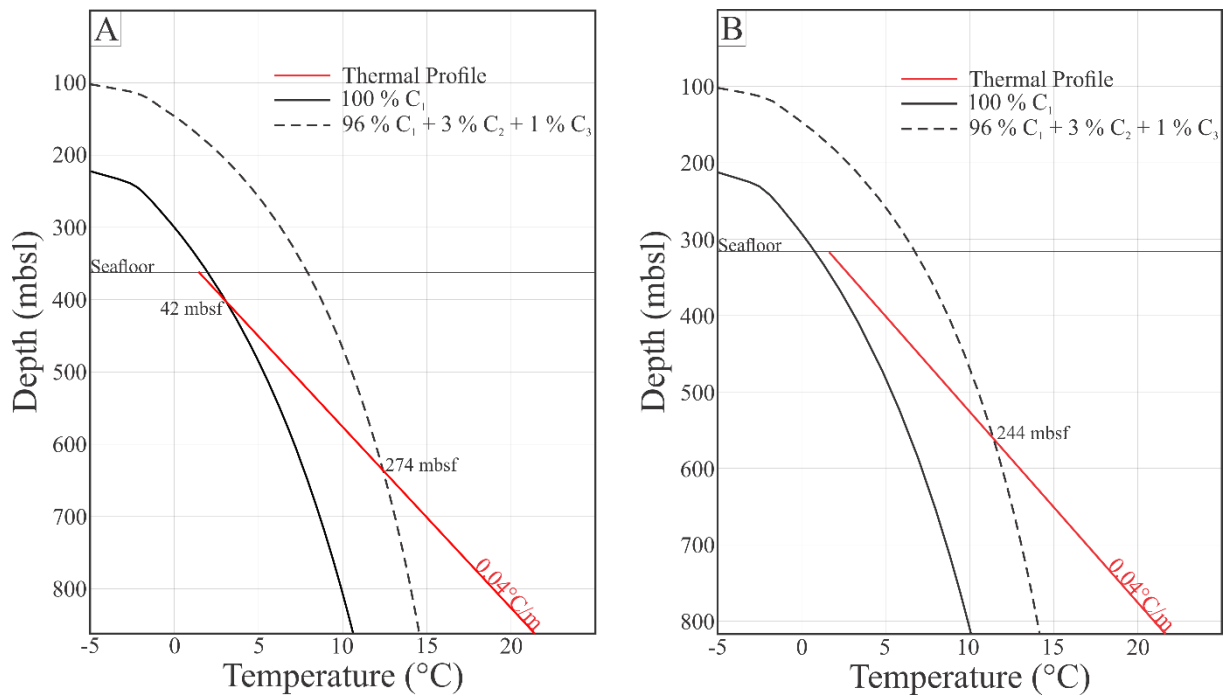
Figure 34: A) Model of the deep part of the study area at present day. B) Model of the shallow part of the study area at present day.

At present day, gas hydrates are predicted to be stable down to 42 m below seafloor in the deep area, with a gas composition of 100 % methane (Fig.34, A). For the mixed composition, gas hydrates are stable at larger depths, 274 m below seafloor.

In the shallow area (Fig.34, B), gas hydrates of 100 % methane cannot be stable, and will act as free gas in the sediments. With the mixed gas composition, gas hydrates are stable down to 244 m below seafloor.

6 – Interpretation and discussion

Topographical change of the seafloor is a result of many different processes. From the geological history of the Barents Sea, it is evident that huge forces contributed to the present day geomorphology and stratigraphical layers. The same applies for the glacial history of the Barents Sea. The different forces of the glaciers having acted on the Barents Sea surface, created mega-scale glacial lineations, ploughmarks, acoustically transparent bodies, retreat moraines, ridge networks, and corrugation ridges (Ottesen and Dowdeswell, 2006; 2009; Winsborrow et al., 2010; Andreassen et al., 2014; Bjarnadóttir et al., 2014).

Being an epicontinental shelf with trough and bank areas (Fig.1), led to erosion of the surface of the troughs, and deposition of sediments at the edges and end of troughs. These troughs have acted as the main area for glacial movement. The study area for this thesis lies inside such a trough. More exactly, Bjørnøyrenna trough (Fig.1).

Furrows on the seafloor, as observed in the northern part of the study area (Fig.2, 11), suggest an erosive agent that scraped away sediments from the seafloor. The other explanation is sediment accumulation, thereby creating ridges. Creation of ridges suggest an ocean current whirling sediments in a specific direction. The ridges of the study area are typically 1-4 m high, with some ridges lying parallel to sub-parallel (Fig.11, B). The water currents need to have accumulated sediments for a prolonged period, to create ridges of this size. Combining this with the differences in orientation of the furrows, and observation of small depressions at the end of some furrows, dismisses the possibility of the water currents.

Uplift of different areas of the Barents Sea led to movement of sediments from high areas towards the lower parts. Sediments travelling downwards erode the surface, but the deep, wide (40-200 m) and long (several kilometres long) furrows would need a large boulder in order to create such features (Fig.11, A). Boulders of this size exist, but as the environment contributes with sediments, the furrows are too long and wide to be made of this process.

Apart from geological history of the area, glacial movement has contributed to the appearance of present day. Studies of glacial processes and features correspond with those observed in the study area. Glacial ploughmarks are typically 0.5-15 m deep, depending on whether they are individual or combined ploughmarks (Andreassen et al., 2014). They have a width of 60-200 m, and combined parallel furrows can be up to 800 m wide (Andreassen et al., 2014). In Bjørnøyrenna (Fig.1), similar furrows are found to be 2-5 m deep and 60-100 m wide, interpreted as iceberg ploughmarks (Bjarnadóttir et al., 2014). The findings of this thesis

correspond with those sightings, and the furrows in the study area are interpreted as iceberg ploughmarks.

Circular depressions occur at the end of some of these ploughmarks. Iceberg ploughmarks have been previously found to terminate in rimmed pits (Bass and Woodworth-Lynas, 1988; Andreassen et al., 2014). The pits are a result of terminating icebergs, rolling at the same location for a prolonged period, leading to icebergs digging down in the underlying sediments, to create circular depressions.

Small bumps inside furrows lying perpendicular to the inferred iceberg flow exist in the study area (Fig.11, C). The small ridges going across the furrows have the same appearance as previously observed ridges, identified as corrugation ridges (Jakobsson et al., 2011; Andreassen et al., 2014). All these features, rimmed pits and corrugation ridges, are observable in the furrows of the study area, and further confirm that the furrows are iceberg ploughmarks.

Having established that the glacial period influenced the study area, there are several features that are interesting to investigate further. The circular depressions and mounds of the study area (Fig.2) drape the seafloor. Some of the circular depressions are iceberg pits. However, the majority of the depressions lies in no relation to any of the ploughmarks of the study area. Inferring that there is another reason why these geomorphological features appear on the seabed.

The first study of seafloor circular depressions done by King and Maclean (1970) suggested seven different formation mechanisms; Man's activities, falling boulders of ice, meteorites, biological activity (fish scouring the surface), water percolation or gas flow. Throughout time, several others have also suggested different mechanisms. Solheim and Elverhøi (1993) suggested three different formation mechanisms; meteorite impact, glacial erosion and shallow gas or gas hydrates. Fichler et al., (2005) suggested the following mechanisms: meteorite impact, volcanism, sediment injection and gas/fluid movement. All of which ended up with the gas flow mechanism as the most likely. In addition, there are new studies that from the beginning inferred that the features were made of gas flow (Nicholas et al., 2014; Nakajima et al., 2014; Ingrassia et al., 2015; Riboulot et al., 2016).

Assessment of the possible explanations for the craters;

1: Man's activities:

For the depressions to be man-made, sign of human activity, or any report of human activity in the area need to be documented. No report of mechanical operations in the area exist, and there are no evidence on the seafloor itself suggesting that humans have created the craters. The study area lies at water depths of 317 to 362 m (Fig.2), and the Barents Sea experience uplift even today, meaning that the water depths previously was deeper. This makes the possibility of having craters made by humans highly unlikely.

The theory is dismissed.

2: Ice-rafted falling boulders:

Falling ice-rafted boulders may create craters. Dependent on the height from which they fall, the impact of boulders hitting soft sediments at the seafloor may create craters. There are however pitfalls to this theory. First, the water depth is high, leading to a slowing down of the boulder, before even hitting the seafloor. Secondly, the dimensions of the craters are massive, which mean that the impact would need to be severe. At last, the depressions are in bedrock, not soft sediments. It would thus be highly unlikely for boulders to hit the seafloor with the amount of force needed to both penetrate the deep water, and yet still have enough force to create massive craters in bedrock.

The theory is dismissed.

3: Meteorites:

The same arguments as for ice-rafted boulders applies for the meteorite theory. Formation of craters due to meteorites is possible, but the condition of the study area and the appearance of the depressions suggest otherwise. The water depth would most likely prevent the meteorites from hitting the seafloor with the force needed. In addition, a meteorite would create a rim at the edge of the craters. The majority of the depressions have no rim. There is the possibility of eroding the rim away post formation of craters, but yet again, the water depth issue is significant.

The theory is dismissed.

4: Biological activity:

Fish and other smaller organisms are able to create craters. Bacteria and marine life exist inside craters, but research show that communities are based on gas seepage, rather than the actual crater (Judd and Hovland, 2007). The massive distribution of craters diminish the possibility of biological activity.

The theory is dismissed.

5: Glacial erosion:

Glacitectonic processes creating circular depressions is well documented, and described as rimmed pits (Bass and Woodworth-Lynas, 1988). These craters occur at the end of glacial ploughmarks. The majority of craters appear alone or at least with no relation to any glacial ploughmarks (Fig.12). Erosion of the seafloor could remove such a relation, but this is highly unlikely, especially since ploughmarks are observed all over the study area.

The other obvious possible mechanism for glaciers to create craters is the so-called hill-hole pair. This theory is based on glaciers moving sediments such that a hill of remaining sediments, as the glacier retreats, follows a hole. The sediments from the hole are thus creating the downstream hill (Sættem, 1990). This means that the hill lies on top of the seafloor, and hence exist with a basal seafloor reflection. Many of the craters exist in close proximity to mounds, but no immediate sign of them laying in the downstream direction of the inferred glacial movement exist.

The theory is plausible.

6: Water percolation:

Water percolation is a process where water migrate in the sediment packages. Through up-dip bedding planes and faults, water can access the seafloor, and send sediments into suspension. Slumping of material at the edge, and further suspension of the sediments would gradually build a large depression. The process is a plausible theory, and may explain the observed seabed features.

The theory is plausible.

7: Gas in the subsurface:

The last possible theory is a process involving hydrocarbons. It is in some way similar to the theory of water percolation. As gas migrates towards the seafloor, there will be a gradual accumulation of gas in the subsurface. The accumulated gas breach the threshold level and bursts into the water column. The process is explosive and sediments are blown away. Since the process is explosive, and happen at a short period, it is a plausible explanation.

The theory is plausible.

Three theories stand as the most plausible explanations; glacial erosion, water percolation and gas.

Ice sheet movement of the study area is inferred to be from northeast to southwest (Winsborrow et al., 2010; Bjarnadóttir et al., 2014). In order to establish glacial erosion and glacitectonic processes as the triggering factor for the craters, a further investigation of the craters is necessary. In investigation of glacial erosional processes, it is common to separate between subglacial and proglacial erosion. Subglacial erosion is the process of erosion underneath the ice sheet, while proglacial erosion is the process of erosion in front of the ice sheet.

Two main processes occur in a subglacial environment. These are abrasion and plucking (Goduie, 2004). Abrasion refer to the process of a glacier carrying coarse debris at the base of the ice sheet to grind the bedrock beneath the glacier. Plucking refers to the process of the glacier detaching large rocks from the already weathered bedrock (Goduie, 2004). In addition, there is the meltwater dynamics occurring in a subglacial environment.

Abrasion of the surface alone would not be able to create craters, as the process scour the seafloor, rather than creating craters. Thus, a secondary process of meltwater dynamics is necessary as a digging and polishing factor. First of all this suggest that the craters are found in association with glacial striations, and in addition, that the observed features appear with a smoothed surface. The majority of craters have a complex appearance, and appear in no relation to any observed glacial striations. This means that abrasion and meltwater dynamics are not able to create the observed craters.

Formation of observed depressions as a cause of plucking is more likely, since circular rock particles can be quarried. Different environments like marine and continental has affected the study area. Thus, there is considerable reason to believe that weathering of the seafloor would

have taken place. Pressure differences due to the different glaciations affecting the study area obviously create faults in the subsurface, but can also create joints in the seafloor. This enhance weathering and increase the possibility of plucking of rock particles from the study area. However, this process mostly create cirques, arêtes and horns (Goduie, 2004). These are huge landforms with no relationship to circular depressions observed on the seafloor. Thus, the possibility of subglacial erosion creating the depressions is highly unlikely, and dismissed as a theory.
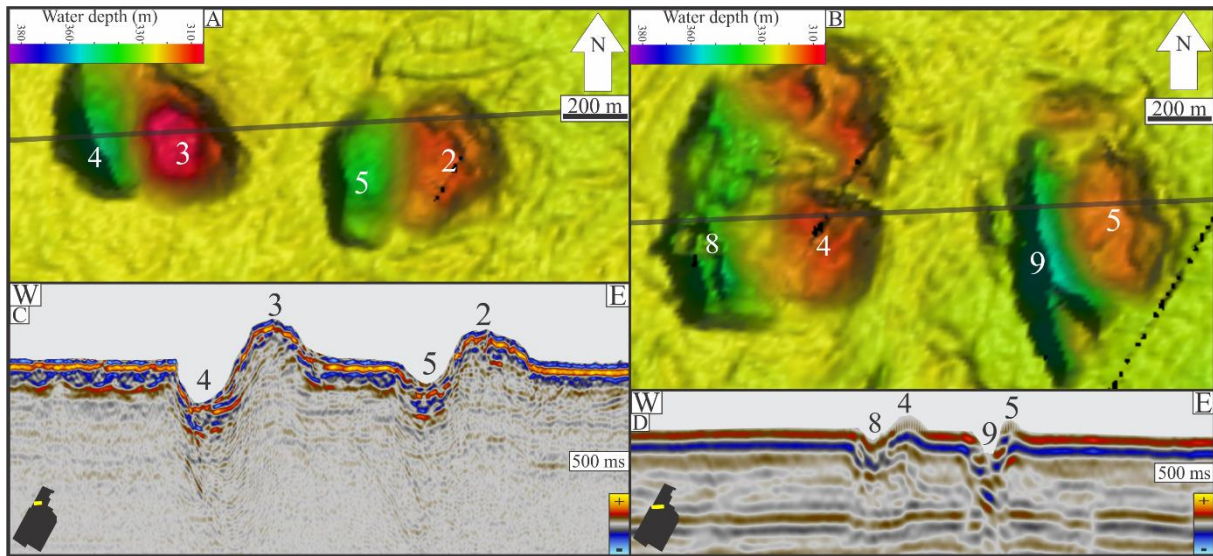
Figure 35: Overview map, showing possible hill-hole pair. C: Seismic section HH13_038_mig_deghost. D: Seismic section 745730-93Potential2.

Proglacial erosion occur in the front, and create large features such as meltwater channels, moraines, ridges, banks and outwash plains (Goduie, 2004). The craters formed by proglacial erosion lies next to mounds, and are called hill-hole pairs. The mounds of the study area are typically associated with pockmarks, meaning that the possibility of them being hill-hole pairs exist. The typical hill-hole system as a whole is between 1 km^2 to 100 km^2, and has a structural relief of 30 to 200 m (Aber et al., 1989). The most notable craters occurring as hill-hole pairs are the system of crater and mound nr.4/3, nr.5/2, nr.8/4 and nr.9/5 (Fig.35). All four lies in area 1 (Fig.19), and follow the same direction concerning what side the mounds lies on. The dimensions of the four systems are between 0.3 and 0.7 km^2. Thus, they are not in the size limit observed by Aber et al., (1989). Since sediments from the hole form an adjacent mound, the sediments lies on top of the seafloor. Upon inspection of the seismic section, the four mounds appear with a basal seafloor reflection. On the two seismic sections (Fig.35, C, D) there are no basal reflection corresponding to the seafloor. This mean that the systems are not hill-hole pairs, and in total dismissing the theory of glacial erosion being the triggering factor for the craters.

70

Previous studies of similar circular depressions all suggested that gas is the triggering mechanism (Solheim and Elverhøi, 1993; Fichler et al., 2005; Sultan et al., 2010; Chand et al., 2012; Nakajima et al., 2014). This is further inferred from the seismic sections (Fig.21, 22, 24, 26, 28, and 29). There are several signs of possible migration pathways for gas in the subsurface. As well as observed gas flares in the study area (Fig.31). In seismic sections, gas is observed as distortions in the seismic reflectors. This is not the case for water. Most of the seismic sections (Fig.21, 24, 26 and 29) show that there are vertical distortions interpreted to be possible migration pathways, and acoustic pipes. Gas in the subsurface contribute to a significant loss of p-wave velocity. Even small amounts of gas in the subsurface lead to change in the seismic sections (Andreassen et al., 2007).

The zones of vertical distortion of seismic reflectors characterizes by having low seismic amplitude and low coherency. A different setting is observed underneath the geomorphological features at Figure 20 and Figure 28. At these locations, there are stronger reflections underneath the seabed features. Low penetration lead to a highly reflected seabed, but less reflected subsurface. Underneath the geomorphological features, there are vertically stronger reflectors. Gas in sediments does not only wipe out the reflections, but may also enhance them, in an environment where there is generally low reflection strength. Hence, the stronger vertical reflectors are interpreted as fluid migration pathways, and acoustic pipes (Løseth et al., 2011).

Pull-up and pull-down of seismic reflectors are visible on Figure 21. The pull-down effect is a good indication of gas in sediments. Hydrocarbons lower the velocity of the sediments, and increase the travel time compared to the surrounding sediments. This create a pull-down effect. In opposition to the pull-down effect, the pull-up effect usually appear because of authigenic carbonates or salt (Marfurt and Alves, 2015). A pull-up effect is also observable in association with the GHSZ (Collett, 2000). The effect typically lies inside the GHSZ, while the opposite pull-down effect usually lies outside of the GHSZ. Due to the lack of a prominent BSR, and the depths at which this effect exist (1000 ms), it is unlikely that the pull-up effect relate to gas hydrates. At the edges of the pull-up (Fig.21), possible fault systems exist. This suggest that compressional faulting cause the effect, rather than gas hydrates.
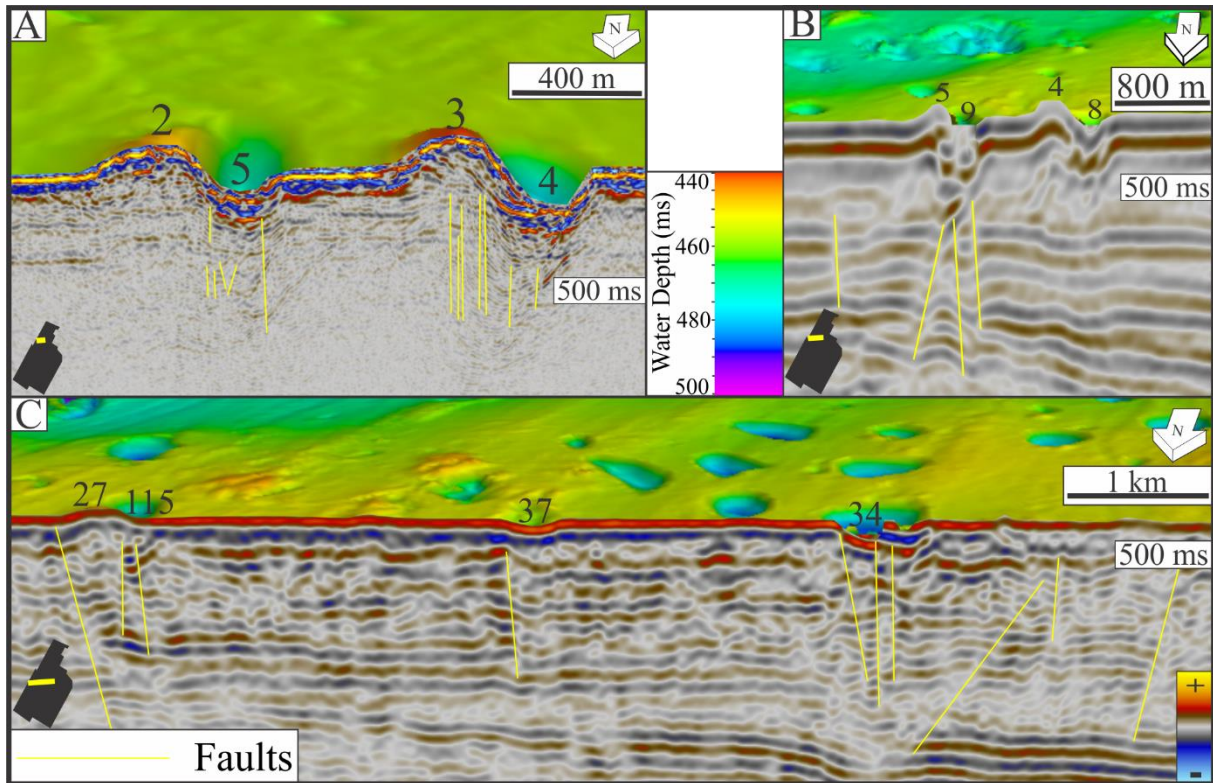
Figure 36: Images showing the fault systems underneath the geomorphological features. A: HH_13_038_mig_deghost. B: 745730-93Potential2. C: 7455-87-8WPotential1. Illumination and vertical exaggeration as the whole images shown in previous sections.

Fault systems close to the seabed (Fig.36) show no specific trend in the orientation of the dip. The faults appear both closely spaced and with large spacing (Fig.36, A, C). The majority of faults in the area appear underneath the seabed features, inferring that there is a link between them and the observed geomorphological features. These seafloor features are thought to be formed by gas, and faults act as good conduits for fluids. Strengthening the theory of gas as the triggering factor.

The mounds of the study area generally occur in association with the craters and are found with many of the same subsurface properties, such as faults and possible migration pathways. However, they are positive topographical features, suggesting that there is another triggering factor. Serié et al., (2012) postulated two main explanations for fluid flow mounds. These are sub-marine volcanoes and gas hydrate mounds. The two theories have different approach as to how the formation mechanism is. Sub-marine volcanoes are extrusive features, expelling fluidized sediments and gases, while gas hydrate mounds are mounds formed due to internal growth of hydrates in the shallow subsurface. With growth of hydrates, an increasing pressure is inflicted on the seafloor, giving rise to the seafloor mound (Serié et al., 2012).

The main factor differentiating the two formation mechanisms is that while sub-marine volcanoes occur with an internal structure and basal reflection corresponding to the seafloor, gas hydrate mounds appear with a lack of internal structure and basal reflection corresponding to the seafloor (Serié et al., 2012). Based on this, and the appearance of the mounds in the seismic section (Fig.36), the gas hydrate mound-theory is most likely correct for the study area. None of the mounds appears with a basal reflection corresponding to the seafloor. Suggesting that the formation mechanism is the growth of gas hydrates, and that they are submarine pingos. To confirm this theory there is a need to find the features in close association with a BSR.
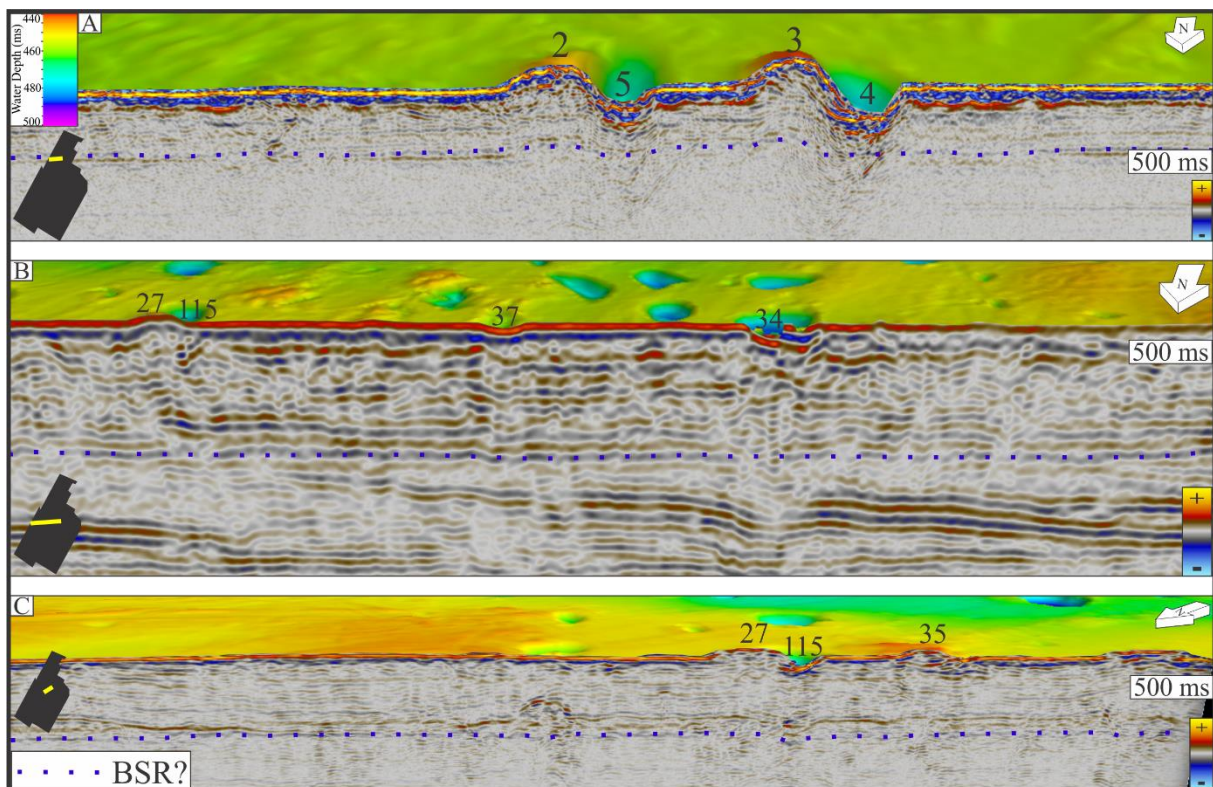
Figure 37: Overview of the three seismic sections with possible BSRs. A: 7455-87-8WPotential1. B: HH_13_038_mig_deghost. C: Cage15-5-001.

Modelling of the GHSZ show that a BSR should exist between the depths of 42 m, and 274 m below seabed (Fig.34). Depending on the gas composition and geothermal gradient, it may exist in between or at even larger depths. By looking after a reversed amplitude reflector, compared to the seafloor, it is possible to identify gas hydrate BSRs. The BSR reflector follows the seafloor depth, and crosscut the sediment packages, as the existence rest on whether or not hydrates are stable (Hyndman and Davis, 1992). A possible BSR is marked in Figure 37, A. The BSR in the seismic section is a negative amplitude layer, opposite of the positive seabed reflector. The same factors applies for the two other possible BSRs (Fig.37, B, C).

Upon inspection of the suggested BSRs, the first (Fig.37, A) appears to be a side-trough. In addition, the BSR appear at very shallow depth. The possible BSR of Figure 37, A, is thus dismissed. The other two bear no sign of being side-troughs. The possible BSR of Figure 37, B, crosscut the underlying clinoforms at 750 ms TWTT, and lies at a depth of 719 ms TWTT. Meaning it lies in the possible BSR range. Due to a lack of log data, the exact depth of the modelled BSR is not possible to illustrate. Based on the model (Fig.34), and the fact that the layer crosscut the clinoforms, it is interpreted to be a gas hydrate BSR.

The third possible BSR lies at a depth of 560 ms TWTT, with the seabed at a deeper water depth than the previous (Fig.37, C). Conditions the model at present day (Fig.34) deem as unstable conditions for gas hydrates. Suggesting that the possible BSR is a regular stratigraphical layer.

Modelling the GHSZ is highly dependent on input parameters. The insecurities of the models is mainly based on gas compositions and geothermal gradient. The 100 % methane composition is an easy choice, as this is the thinnest possible stability zone. However, the chosen mixed gas composition may be wrong, which would lead to either a thinner or thicker stability zone. Only one seismic section show an interpreted BSR that fit the identification factors for BSRs. Thus, there are several possibilities: 1) Gas hydrates are unstable in the study area as a whole. 2) BSRs exist in the study area, but only in local areas not covered by the seismic lines. 3) Too low resolution of the seismic lines to be able to identify any BSR. 4) The model depicts correctly, and the interpreted BSR (Fig.37, B) is an actual BSR. Inferring that gas hydrates are stable in the study area.
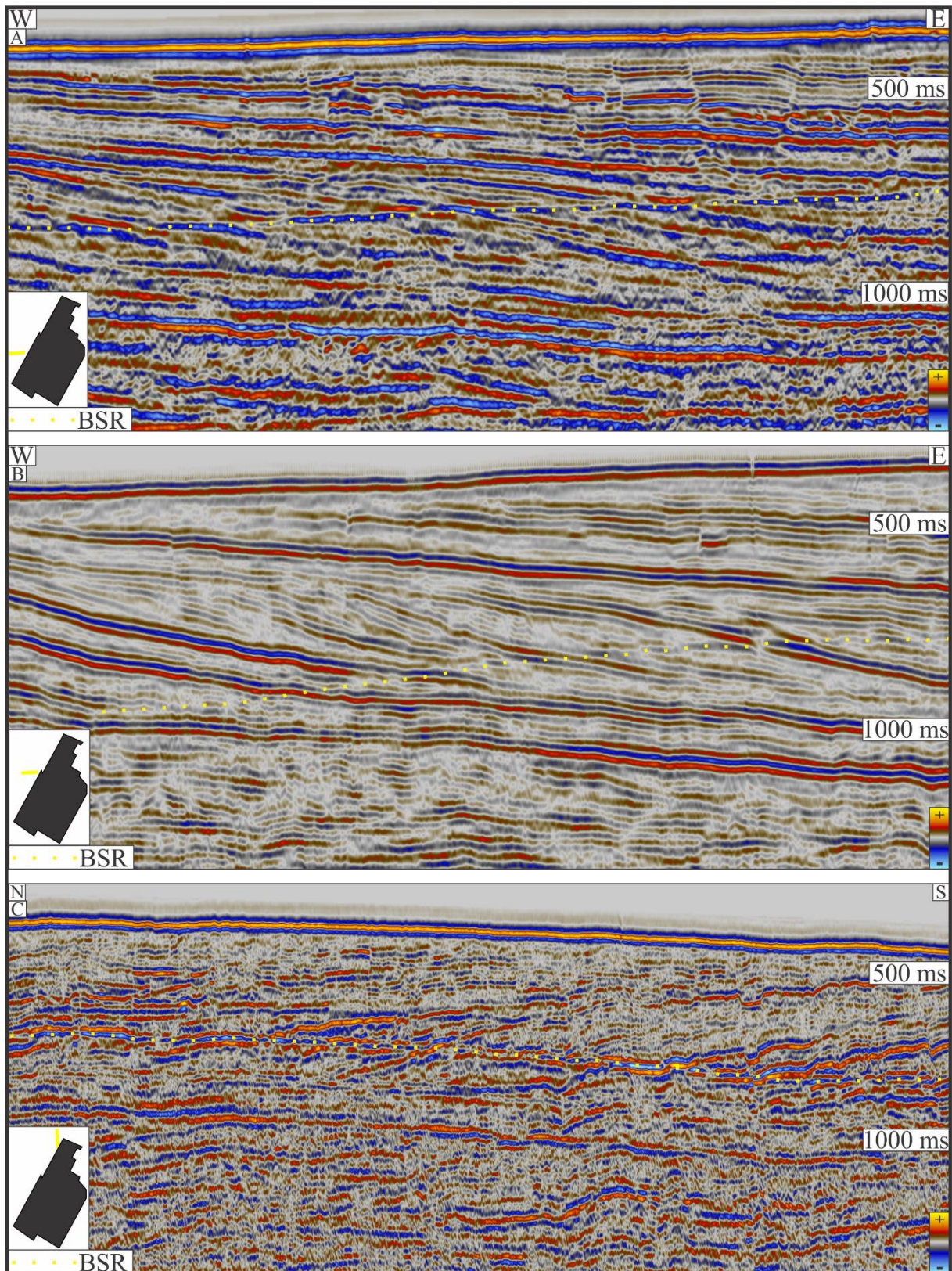
Figure 38: A: Seismic section of 745230-94, with interpreted BSR. B: Seismic section of 745730-93Potential2, with interpreted BSR. C: Seismic section 2745-87_SBSW, with interpreted BSR.

Outside of the study area, several prominent BSRs are visible (Fig.38). Each of which crosscuts

the stratigraphy, and at a reasonable depth for gas hydrate BSR occurrence. Gas hydrate BSRs

exist in several different locations throughout the Barents Sea (Chand et al., 2012; Ostanin et al., 2013; Vadakkepuliyambatta et al., 2015). All three BSRs on the outside of the study area occur at the same depth compared to the seafloor as the interpreted BSR of Figure 37, B. Thus, it is reasonable that gas hydrates are stable in the area, and that the lack of BSRs underneath the craters and mounds ascribe to poor seismic resolution, low concentrations of free gas or that it is difficult to detect due to a lack of dipping bedding planes in the subsurface.

It is obvious that the GHSZ is severely reduced because of the retreat of ice sheets (Fig. 32 and 34). Thus, the dissolution of gas hydrates indisputably contributed to an accumulation of free gas in the subsurface. In the most extreme case of the models, there is a release of 622 m of free gas (Fig.32 and 34). This add a massive volume of free gas in the subsurface. Keeping in mind that the volume correlation of 1 m^3 gas hydrate equal 164 m^3 of free gas (Kvenvolden, 1998), result in a considerable amount of potential free gas.

Despite of this there are few clear signs of gas in the subsurface in the seismic sections (Fig.20, 21, 22, 24, 26, 28 and 29). Two possible explanations emerge to explain this. The first is that water has migrated in the migration pathways, while the second is that the gas has left the area. Suggesting a dormant area. Migration of water through fault systems is no new observation, but the biggest issue with the water theory is that it is highly unlikely for water to accumulate enough pressure to create the circular depressions. Hence, it is more likely that gas inflicted the area.

At the seafloor of the study area, several gas flares are visible (Fig.31). This shows that the area is active today. A larger number of gas flares exist on top of mounds, rather than inside the craters, where most of them rather lies on the rim, suggesting that a cementation takes place when the gas vent out of the crater (Hovland and Svensen, 2006). The result is that the gas need to find another way to migrate, and thus move to the sides of the craters, where it can migrate into the water column.

As gas flares show that the area is active today, it is likely to observe clear hydrocarbon indications in the subsurface. Except for the possible migration pathways and acoustic pipes, the seismic sections (Fig.20, 21, 22, 24, 26, 28 and 29) lacks bright spots and other normal hydrocarbon indications. Interpreted to be because of permeable layers in the subsurface, the hydrocarbons never accumulate enough free gas under a sealing sediment package, and just continue to migrate towards the seafloor.

The migration take place both inside faults and through permeable sediment packages. Tectonic movement enhances and reactivate the faults in the subsurface. In addition, the proven glacial movement add further stress to the already brittle rock. Further reactivating the faults, enhancing the migration pathway (Ostanin et al., 2013). In respect to this, it is crucial how old the geomorphological features are.

Observation of the mounds of the study area (Fig.14) show that many of them exist with glacial ploughmarks. This means that icebergs moved in the area at the time these mounds already had formed. Dating the mounds with ploughmarks to be younger than LGM and created during deglaciation. During deglaciation, the icebergs floated in the water, and had a sufficient ice supply upstream of the study area. Some of the mounds appear without glacial ploughmarks, and are interpreted to be even younger than those created during deglaciation.

Craters made before LGM characterizes by gentle slopes, partly infill of sediments in the direction of the glacial movement, and lack of rims at the edges (Solheim and Elverhøi, 1993). Few to none of the craters in the study area (Fig.12) have these characteristics, and thus the craters are interpreted to be younger than LGM.

During the different major glaciations, large ice sheets covered the study area (Fig.6). In addition, the large ice sheets contributed to a more suitable environment for gas hydrates to be stable. With increased pressure and colder climate, the GHSZ increased. When the ice sheet retreats, pressure release and the GHSZ decrease. Gas hydrates start to dissolute, and there is a massive release of free gas. Methane in hydrates expand to 164 times the original volume, when melting (Kvenvolden, 1998). Gas breaching the threshold value of the overburden sediments, create one or several massive expulsions of gas to the water column, and thus craters form.
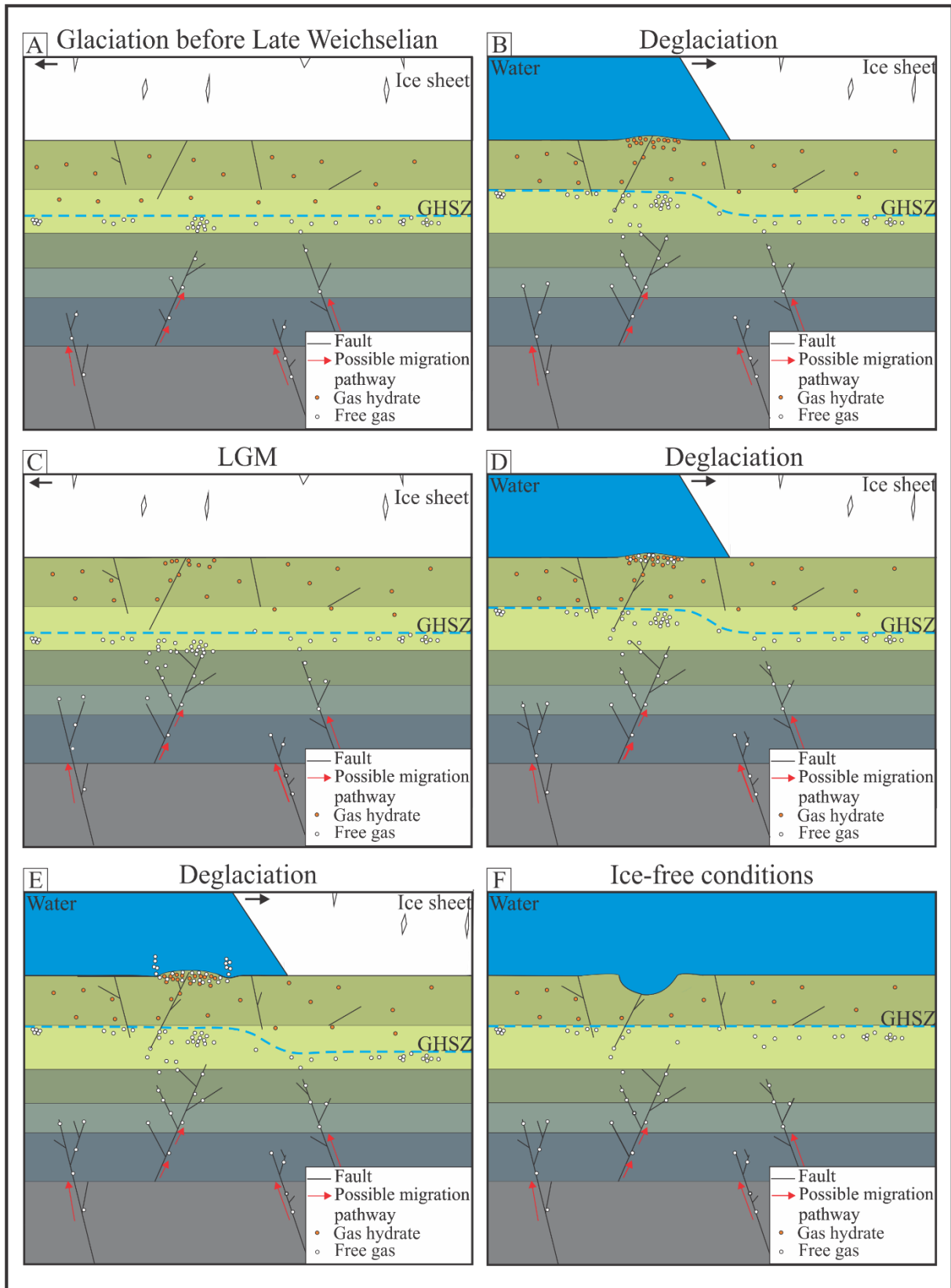
Figure 39: Suggested formation mechanism of the observed features.

The model (Fig.39) shows the suggested formation mechanism of the observed features. In the beginning fault systems in the subsurface exist (Fig.39, A), but with limited extent. The GHSZ decrease as the ice sheet retreat (Fig.39, B), leading to dissolution of gas hydrates, as well as reactivation of faults. With the advance of the ice sheet, the small mound of accumulated gas hydrates in Figure 39, B, is eroded away (C), before reappearing as the ice retreats (D). After LGM the ice sheet retreat and the gas hydrate environment has time to mature (E). In this process, hydrate dissolution and increased pore pressure lead to a collapse of the seafloor at the edges of the mound. Gas leaking into the seafloor at the collapse is observable as gas flares. Continuous dissolution of gas hydrates and an increasing pore pressure result in gas reaching the threshold value for the seafloor. Thus breaching the seafloor in an explosive blowout, creating the crater (F). In some cases, several blowouts have formed the present day craters.

Inferring that the geomorphological features form due to gas hydrates, and it is therefore possible to classify circular depressions based on size. Judd and Hovland (2007) postulated that pockmarks are craters of size smaller than 100 m in diameter. Thus, 20 % of the craters in the study area are pockmarks. Calling those with a diameter of 100-300 m large pockmarks, result in 53 % of them being large pockmarks. The rest are referred to as fluid flow craters, and count for 27 % of the total depressions. Gas hydrate mounds are generally referred to as submarine pingos or just pingos, and thus there are 227 pingos in the study area.

7 – Conclusion

Mapping of geomorphological features and gas flares show that there are 288 craters, 227 mounds and 119 gas flares in the study area. The features have its own distinctive shape and dimension. Dimensions of the depressions range from 43 to 906 m, and with depth of 0.5 to 34 m, while the mounds are 28 to 650 m in width and 0.2 to 25 m in height. The mounds clearly relate to the depressions. They exist either inside or in close proximity, interpreted as one system.

Large vertical faulting systems are visible underneath the geomorphological features. Some of them are difficult to clearly observe as faults. They may act as migration paths for hydrocarbons travelling to the seabed. The base of the craters consist of multiple faults that either reach or are close to the seabed. Generally, the inspected mounds lack internal structure and basal reflection corresponding to the seafloor. They are interpreted as gas hydrate mounds or submarine pingos. An observed reversed reflector crosscutting the stratigraphic layers is interpreted to be a gas hydrate BSR. In addition, three other seismic lines show BSRs lying on the outside of the study area.

Models of the GHSZ during LGM, deglaciation and present day show a large change of the stability zone. The decrease of the GHSZ result in release of free gas, migrating in the migration pathways. Extensive signs of glacial activity cover the study area. Advance and retreat of ice sheets led to fracturing and reactivation of faults, enhancing the fluid migration paths. Gas flares observed on the seafloor indicate that the area is still active. There are few clear hydrocarbon signs underneath the craters and mounds. This is interpreted to be because of sufficient fluid flow towards the seafloor. Lack of gas flares observed inside and near craters is thought to be due to cementing of the migration pathways inside the crater. This result in gas migrating on the outside of the crater, and migrating to the neighbour pingos, where a sufficient migration system exist.

The increased free gas accumulation, either from fluid flow or dissolution of gas hydrates, accumulated gas in the subsurface. Seabed elevated because of gas hydrate accumulation, resulting in pingos. Continuous supply resulted in breaching of the threshold value. Thus, one or several expulsions of free gas created the craters. Based on size there are 58 pockmarks, 153 large pockmarks and 77 fluid flow craters.

8 - References

Aber, J., Croot, D. & Fenton, M., 1989. *Glaciotectonic Landforms and Structures.* 1st ed. Dordrecht, Holland: Springer Netherlands.

Andreassen, K., 2009. *Marine Geophysics, Lecture Notes for Geo-3123.* Tromsø: University of Tromsø.

Andreassen, K., Laberg, J. & Vorren, T., 2008. Seafloor geomorphology of the SW Barents Sea and its glaci-dynamic implications. *Geomorphology,* Volume 97, pp. 157-177.

Andreassen, K., Nilssen, E. & Ødegaard, M., 2007. Analysis of shallow gas and fluid migration within the Plio-Pleistocene sedimentary succession of the SW Barents Sea continental margin using 3D seismic data. *Geo-Mar Lett,* Volume 27, pp. 155-171.

Andreassen, K., Nilssen, L., Rafaelsen, B. & Kuilman, L., 2004. Three-dimensional seismic data from the Barents Sea margin reveal evidence of past ice streams and their dynamics. *Geology,* Volume 32, pp. 729-732.

Andreassen, K., Winsborrow, M., Bjarnadóttir, L. & Rüther, D., 2014. Ice stream dynamics inferred from an assemblage of landforms in the northern Barents Sea. *Quaternary Science Reviews,* Volume 92, pp. 246-257.

Bass, D. & Woodworth-Lynas, C., 1988. Iceberg crater marks on the sea floor Labrador Shelf. *Marine Geology,* Volume 79, pp. 243-260.

Bates, R. & Jackson, J., 1987. *Glossary of Geology.* 3rd ed. Alexandria, USA: American Geophysical Institute.

Benjamin, U., Huuse, M. & Hodgetts, D., 2015. Canyon-confined pockmarks on the western Niger Delta slope. *Journal of African Earth Sciences,* Volume 107, pp. 15-27.

Bjarnadóttir, L., Winsborrow, M. & Andreassen, K., 2014. Deglaciation of the central Barents Sea. *Quarternary Science Reviews,* Volume 92, pp. 208-226.

Bulat, J., 2005. Some considerations on the interpretation of seabed images based on commerical 3D seismic in the Faroe-Shetland Channel. *Basin Research,* Volume 17, pp. 21-42.

Butt, F., Elverhøi, A., Solheim, A. & Forsberg, C., 2000. Dechiphering Late Cenozoic development of the western Svalbard Margin from ODP Site 986 results. *Marine Geology,* Volume 169, pp. 373-390.

Bünz, S., Mienert, J. & Berndt, C., 2003. Geological controls on the Storegga gas-hydrate system of the mid-Norwegian continental margin. *Earth and Planetary Science Letters,* Volume 209, pp. 291-307.

Bünz, S. et al., 2012. Active gas venting through hydrate-bearing sediments on the Vestnesa Ridge, offshore W-Svalbard. *Marine Geology,* Volume 332-334, pp. 189-197.

Chand, S. et al., 2008. Gas hydrate stability zone modelling in areas of salt tectonics and pockmarks of the Barents Sea suggests an active hydrocarbon venting system. *Marine and Petroleum Geology,* Volume 25, pp. 625-636.

Chand, S. & Minshull, T., 2003. Seismic constraints on the effects of gas hydrate on sediment physical properties and fluid flow: a review. *Geofluids,* Volume 3, pp. 275-289.

Chand, S. et al., 2012. Multiple episodes of fluid flow in the SW Barents Sea (Loppa High) evidenced by gas flares, pockmarks and gas hydrate accumulation. *Earth and Planetary Science Letters,* Volume 331-332, pp. 305-314.

Chopra, S. & Marfurt, K., 2005. Seismic attributes - A historical perspective. *Geophysics,* 70(5), pp. 3-28.

Clark, C., 1993. Mega-scale glacial lineations and cross-cutting ice-flow landforms. *Earth Surface Processes and Landforms,* Volume 18, pp. 1-29.

Collett, T., 2000. Natural Gas Hydrates: Resource of the 21st Century?. In: *Petroleum Provinces of the 21st Century.* San Diego, California, U.S.A.: The American Association of Petroleum Geologists, pp. 1-64.

Collett, T., Johnson, A., Knapp, C. & Boswell, R., 2009. *Natural Gas Hydrates: Energy Resource potential and Associated Geologic Hazards.* 89 ed. Denver, Colorado, U.S.A.: American Association of Petroleum Geologists.

Directorate, N. P., 2016. *Fact Maps,* Stavanger: Norwegian Petroleum Directorate.

Doré, A., 1995. Barents Sea Geology, Petroleum Resources and Commerical Potential. *Arctuc,* 48(3), pp. 207-221.

Fichler, C., Henriksen, S., Rueslaatten, H. & Hovland, M., 2005. North Sea Quaternary morphology from seismic and magnetic data: indication for gas hydrates during glaciation?. *Petroleum Geoscience,* Volume 11, pp. 331-337.

Goduie, A., 2004. *Encyclipedia of Geomorphology.* 2nd ed. London, UK; New York, USA: Routledge.

Hornbach, M. et al., 2003. Direct seismic detection of methane hydrate on the Blake Ridge. *Geophysics,* 68(1), pp. 92-100.

Hovland, M., 2005. Gas hydrates. In: *Encyclopedia of Geology.* s.l.:Elsevier, pp. 261-268.

Hovland, M. & Svensen, H., 2006. Submarine pingoes: Indicators of shallow gas hydrates in a pockmark at Nyegga, Norwegian Sea. *Marine Geology,* Volume 228, pp. 15-23.

Hyndman, R. & Davis, E., 1992. A Mechanism for the Formation of Methane Hydrate and Seafloor Bottom-Simulating Reflectors by Vertical Fluid Expulsion. *Journal of Geophysical Research,* Volume 97, pp. 7025-7041.

Ingrassia, M. et al., 2015. The Zannone Giant Pockmark: First evidence of a giant complex seeping structure in shallow-water, central Mediterrian Sea, Italy. *Marine Geology vol.363,* pp. 38-51.

International Heat Flow Commision, T., 2016. *The Global Heat Flow Database.* [Online]
Available at: http://www.heatflow.und.edu/index2.html
[Accessed 25 04 2016].

IPCC, 2013. *Climate Change 2013: The Physical Science Basis.* Cambridge, United Kingdom and New York, NY, USA: Cambridge University Press.

Jakobsson, M. et al., 2011. Geological record of ice shelf break-up and grounding line retreat, Pine Island Bay, West Antarctica. *Geology,* 39(7), pp. 691-694.

Judd, A. & Hovland, M., 2007. *Seabed Fluid Flow: The Impact on Geology, Biology, and Marine Environment.* 1 ed. Northumberland, High Mickley, UK: Cambridge University Press.

King, L. & MacLean, B., 1970. Pockmarks on the Scotian Shelf. *Geological Society of America Bulletin,* Volume 81, pp. 3141-3148.

Knies, J., Matthiessen, J., Vogt, C. & Stein, R., 2002. Evidence of 'Mid-Pliocene' (~3 Ma) global warmth' in the eastern Arctic Ocean and implications for the Svalbard/Barents Sea ice sheet during the late Pliocene and early Pleistocene (~3-1.7 Ma). *Boreas,* Volume 31, pp. 82-93.

Kvenvolden, K., 1998. A primer on the geological occurence of gas hydrate. In: J. Henriet & J. Mienert, eds. *Gas hydrates: Relevance to World Margin Stability and Climate Change.* London: Geological Society, London, Special Publications 137, pp. 9-30.

Laberg, J., Andreassen, K. & Knutsen, S., 1998. Inferred gas hydrate on the Barents Sea shelf a model for its formation and a volume estimate. *Geo Marine Letters,* Volume 18, pp. 26-33.

Laberg, J. & Vorren, T., 1996. The Middle and Late Pleistocene evolution of the Bear Island Trough Mouth Fan. *Global and Planetary Change,* Volume 12, pp. 309-330.

Long, D., Lammers, S. & Linke, P., 1998. Possible hydrate mounds within large sea-floor craters in the Barents Sea. *Geological Society, London Special Publications vol.137,* pp. 223-237.

Lundschien, B., Høy, T. & Mørk, A., 2014. Triassic hydrocarbon potential in the Northern Barents Sea; integrating Svalbard and stratigraphic core data. *Norwegian Petroleum Directorate Bulletin,* Volume 11, pp. 3-20.

Løseth, H., Gading, M. & Wensaas, L., 2009. Hydrocarbon leakage interpreted on seismic data. *Marine and Petroleum Geology,* Volume 26, pp. 1304-1319.

Løseth, H. et al., 2011. 1000 m long gas blow-out pipes. *Marine and Petroleum Geology,* Volume 28, pp. 1047-1060.

Marfurt, K. & Alves, T., 2015. Pitfalls and limitations in sesmic attribute interpretation of tectonic features. *Interpretation,* Volume 3, pp. A5-A15.

Mienert, J., Posewang, J. & Lukas, D., 2001. Changes in the Hydrate Stability Zone on the Norwegian Margin and their Consequence for Methane and Carbon Releases Into the Oceanosphere. In: S. P., W. Ritzrau, M. Schlüter & J. Thiede, eds. *The Northern North Atlantic: A Changing Environment.* Tromsø: Springer, pp. 259-280.

Nakajima, T. et al., 2014. Formation of pockmarks and submarine canyons associated with dissociation of gas hydrates on the Joetsu Knoll eastern margin of the Sea of Japan. *Journal of Asian Earth Sciences,* Volume 90, pp. 228-242.

Nicholas, W. et al., 2014. Pockmark development in the Petrel Sub-basin, Timor Sea, Northern Australia: Seabed habitat mapping in support of CO2 storage assessments. *Continental Shelf Research,* Volume 83, pp. 129-142.

Nouzé, H. et al., 2009. Geophysical characterization of bottom simulating reflectors in the Fairway Basin (off New Caledonia, Southwest Pacific), based on high resolution seismic profiles and heat flow data. *Marine Geology,* 266(10), pp. 80-90.

Ostanin, I., Zahie, A., Primio di, R. & Bernal, A., 2013. Hydrocarbon plumbing systems above the Snøhvit gas field: Structural control and implications for thermogenic methane leakage in the Hammerfest Basin, SW Barents Sea. *Marine and Petroleum Geology,* Volume 43, pp. 127-146.

Ottesen, D. & Dowdeswell, J., 2006. Assemblages of submarine landforms produced by tidewater glaciers in Svalbard. *Journal of Geophysical Research,* Volume 111, p. F01016.

Ottesen, D. & Dowdeswell, J., 2009. An inter-ice-stream glaciated margin: Submarine landforms and a geomorphic model based on marine-geophysical data from Svalbard. *GSA Bulletin,* 121(11/12), pp. 1647-1665.

Riboulot, V., Sultan, N., Imbert, P. & Ker, S., 2016. Initiation of gas-hydrate pockmark in deep-water Nigeria: Geo-mechanical analysis and modelling. *Earth and Planetary Science Letters vol.434,* pp. 252-263.

Riis, F. et al., 2008. Evolution of the Triassic shelf in the northern Barents Sea region. *Polar Research,* Volume 27, pp. 318-338.

Sejrup, H. et al., 2005. Pleistocene glacial history of the NW European continental margin. *Marine and Petroleum Geology,* Volume 22, pp. 1111-1129.

Serié, C., Huuse, M. & Schødt, N., 2012. Gas hydrate pingoes: Deep seafloor evidence of focused fluid flow on continental margins. *Geology,* 40(3), pp. 207-210.

Shipley, T. et al., 1979. Seismic Evidence for Widespread Possible Gas Hydrate Horizons on Continental Slopes and Rises. *The American Association of Petroleum Geologists Bulletin,* 63(12), pp. 2204-2213.

Siegert, M., Dowdeswell, J., Hald, M. & Svendsen, J.-I., 2001. Modelling the Eurasian Ice Sheet through a full (Weichselian glacial cycle). *Global and Planetary Change,* Volume 31, pp. 367-385.

Sloan, E. J., 1998. *Clathrate hydrates of natural gases.* 2nd ed. Golden, Colorado: Marcel Dekker Inc..

Smelror, M., Petrov, O., Larssen, G. & Werner, S., 2009. *Geological History of the Barents Sea.* Trondheim: Geological Survey of Norway.

Solheim, A., Andersen, E., Elverhøi, A. & Fiedler, A., 1996. Late Cenozoic depositional history of the western Svalbard continental shelf, controlle by subsidence and climate. *Global and Planetary Change,* Volume 12, pp. 135-148.

Solheim, A. & Elverhøi, 1993. Gas-related sea floor craters in the Barents Sea. *Geo-Marine Letters vol.13,* pp. 235-243.

Solheim, A. & Elverhøi, A., 1985. A pockmark field in the Central Barents Sea; gas from petrogenic source?. *Polar Research,* Volume 3, pp. 11-19.

Solheim, A. & Elverhøi, A., 1993. Gas-related sea floor craters in the Barents Sea. *Geo-Marine Letters,* Volume 13, pp. 235-243.

Sultan, N. et al., 2010. Hydrate dissolution as a potential mechanism for pockmark formation in the Niger Delta. *Journal of geophysical research,* Volume 115.

Sun, Y. et al., 2012. Gas hydrates associated with gas chimneys in fine-grained sediments of the northern South China Sea. *Marine Geology,* Volume 311-314, pp. 32-40.

Svendsen, J. et al., 2004. Late Quaternary ice sheet history of northern Eurasia. *Quaternary Science Reviews,* Volume 23, pp. 1229-1271.

Svendsen, J., Gataullin, V., Mangerud, J. & Polyak, L., 2004. The Glacial Histroy of the Barents and Kara Sea region. *Developments in Quarternary Sciences,* Volume 2, pp. 369-378.

Sættem, J., 1990. Glaciotectonic forms and structures on the Norwegian continental shelf: observations, processes and implications. *Norsk Geologisk Tidsskrift,* Volume 70, pp. 81-94.

Sættem, J., Poole, D., Ellingsen, L. & Sejrup, H., 1992. Glacial geology of outer Bjørnøyrenna, southwestern Barents Sea. *Marine Geology,* Volume 103, pp. 15-51.

Vadakkepuliyambatta, S., Hornbach, M., Bünz, S. & Phrampus, B., 2015. Controls on gas hydrate system evolution in a region of active flow in the Barents Sea. *Marine and Petroleum Geology,* Volume 66, pp. 861-872.

Vorren, T., Landvik, J., Andreassen, K. & Laberg, J., 2011. Glacial History of the Barents Sea Region. In: J. Meer van der, ed. *Developments in Quaternary Science Vol.15.* Tromsø: Elsevier, pp. 361-372.

Winsborrow, M., Andreassen, K., Corner, G. & Laberg, J., 2010. Deglaciation of a marine-based ice sheet: Late Weichselian paleo-ice dynamics and retreat in the southern Barents Sea reconstructed from onshore and offshore glacial geomorphology. *Quarternary Science Reviews,* Volume 29, pp. 424-442.

9 – Appendix

9.1 – Depressions spreadsheet

Table 3: Overview of depressions in the study area, and their properties. Y=Yes, N=No.

Number:	Dimension (m):	Depth (m):	Shape:	Relation to mounds (Y/N):	Type:
1	82	2	Circular	N	Pockmark
2	61	1	Circular	N	Pockmark
3	81	2	Elliptical	N	Pockmark
4	336	22	Elliptical	Y	Crater
5	301	17	Elliptical	Y	Crater
6	164	2.5	Semi-circular	N	Large pockmark
7	121	3.5	Elliptical	N	Large pockmark
8	306	19	Elliptical	Y	Crater
9	246	25.5	Elliptical	Y	Large pockmark
10	93	2.5	Circular	N	Pockmark
11	313	9	Circular	N	Crater
12	318	12	Circular	N	Crater
13	178	7	Semi-circular	N	Large pockmark
14	414	25.5	Circular	N	Crater
15	200	3.5	Circular	N	Large pockmark
16	203	2.5	Semi-circular	Y	Large pockmark
17	82	1	Semi-circular	N	Pockmark
18	381	5	Semi-circular	N	Crater
19	410	5	Semi-circular	N	Crater
20	372	7	Elliptical	Y	Crater

21	976	17	Semi-circular	Y	Crater
22	340	5	Semi-circular	Y	Crater
23	268	4	Semi-circular	Y	Large pockmark
24	226	6.5	Elliptical	Y	Large pockmark
25	218	2	Semi-circular	N	Large pockmark
26	219	8	Elliptical	Y	Large pockmark
27	386	15	Elliptical	N	Crater
28	467	12	Circular	Y	Crater
29	563	18	Semi-circular	Y	Crater
30	382	13	Elliptical	Y	Crater
31	188	2	Circular	N	Large pockmark
32	536	16	Elliptical	Y	Crater
33	253	7	Circular	N	Large pockmark
34	568	28	Elliptical	Y	Crater
35	100	2.5	Elliptical	N	Pockmark
36	411	24	Elliptical	N	Crater
37	390	4.5	Circular	N	Crater
38	390	14	Elliptical	N	Crater
39	405	24	Elliptical	N	Crater
40	458	2	Elliptical	N	Crater
41	414	24	Elliptical	N	Crater
42	330	14	Circular	Y	Crater
43	495	23	Circular	N	Crater
44	131	8	Elliptical	N	Large pockmark
45	127	6.5	Elliptical	N	Large pockmark

46	170	10	Elliptical	N	Large pockmark
47	582	30	Circular	N	Crater
48	188	5	Circular	N	Large pockmark
49	178	5.5	Circular	N	Large pockmark
50	136	1.5	Elliptical	N	Large pockmark
51	276	8	Elliptical	Y	Large pockmark
52	387	20	Circular	N	Crater
53	190	6	Circular	N	Large pockmark
54	294	6	Elliptical	N	Large pockmark
55	232	3	Circular	N	Large pockmark
56	131	3	Circular	N	Large pockmark
57	164	1.5	Circular	N	Large pockmark
58	157	1.5	Circular	N	Large pockmark
59	185	4	Circular	N	Large pockmark
60	157	1.5	Circular	N	Large pockmark
61	159	4.5	Elliptical	N	Large pockmark
62	150	4.5	Elliptical	N	Large pockmark

63	188	3.5	Elliptical	Y	Large pockmark
64	98	3	Circular	N	Pockmark
65	167	2	Circular	N	Large pockmark
66	149	4	Elliptical	N	Large pockmark
67	327	6	Semi-circular	N	Crater
68	353	8.5	Circular	N	Crater
69	290	9	Circular	Y	Large pockmark
70	123	1.5	Circular	N	Large pockmark
71	180	3.5	Elliptical	N	Large pockmark
72	196	7	Circular	N	Large pockmark
73	426	8	Semi-circular	Y	Crater
74	586	17	Semi-circular	Y	Crater
75	230	3	Elliptical	Y	Large pockmark
76	381	7	Circular	N	Crater
77	429	10	Semi-circular	Y	Crater
78	37	10	Semi-circular	N	Crater
79	433	6.5	Elliptical	Y	Crater
80	488	9	Circular	N	Crater
81	785	6	Circular	Y	Crater
82	398	11	Elliptical	Y	Crater
83	341	6	Elliptical	N	Crater
84	62	1	Circular	N	Pockmark
85	54	0.5	Elliptical	N	Pockmark
86	394	2.5	Circular	Y	Crater
87	330	3.5	Semi-circular	Y	Crater

88	93	1.5	Circular	N	Pockmark
89	235	3	Circular	N	Large pockmark
90	573	7	Circular	Y	Crater
91	224	4	Elliptical	N	Large pockmark
92	150	2	Circular	N	Large pockmark
93	463	10	Circular	N	Crater
94	353	6	Semi-circular	N	Crater
95	218	4	Elliptical	N	Large pockmark
96	124	3.5	Elliptical	N	Large pockmark
97	150	3	Elliptical	N	Large pockmark
98	158	1	Elliptical	N	Large pockmark
99	334	12	Elliptical	Y	Crater
100	283	8	Circular	N	Large pockmark
101	126	2	Semi-circular	N	Large pockmark
102	237	6	Elliptical	N	Large pockmark
103	144	4.5	Elliptical	N	Large pockmark
104	180	2	Elliptical	N	Large pockmark
105	201	4	Elliptical	N	Large pockmark
106	174	4	Elliptical	N	Large pockmark

107	89	1.5	Semi-circular	N	Pockmark
108	112	3	Circular	N	Large pockmark
109	387	12	Circular	N	Crater
110	400	11	Circular	Y	Crater
111	117	2	Elliptical	N	Large pockmark
112	162	2	Semi-circular	N	Large pockmark
113	154	3	Semi-circular	N	Large pockmark
114	81	1.5	Circular	N	Pockmark
115	377	15	Semi-circular	Y	Crater
116	221	8	Elliptical	N	Large pockmark
117	141	8	Elliptical	N	Large pockmark
118	152	2	Circular	N	Large pockmark
119	522	22	Circular	Y	Crater
120	425	11	Circular	Y	Crater
121	445	8	Elliptical	N	Crater
122	137	4	Elliptical	Y	Large pockmark
123	623	25	Elliptical	Y	Crater
124	80	1.5	Semi-circular	N	Pockmark
125	120	2	Semi-circular	N	Large pockmark
126	130	6	Semi-circular	N	Large pockmark
127	216	12	Elliptical	N	Large pockmark
128	637	25	Circular	Y	Crater

129	129	2.5	Circular	N	Large pockmark
130	310	7	Semi-circular	N	Crater
131	114	2	Elliptical	N	Large pockmark
132	63	1	Circular	N	Pockmark
133	342	11	Elliptical	Y	Crater
134	187	10	Elliptical	N	Large pockmark
135	487	20	Elliptical	Y	Crater
136	315	6.5	Semi-circular	Y	Crater
137	71	1	Elliptical	N	Pockmark
138	125	2	Elliptical	N	Large pockmark
139	90	2.5	Circular	N	Pockmark
140	396	20	Circular	Y	Crater
141	72	2	Circular	N	Pockmark
142	114	2.5	Elliptical	N	Large pockmark
143	348	11	Semi-circular	Y	Crater
144	427	12.5	Elliptical	N	Crater
145	255	7	Semi-circular	N	Large pockmark
146	179	6	Semi-circular	N	Large pockmark
147	161	7	Circular	N	Large pockmark
148	215	3	Circular	N	Large pockmark
149	88	1.5	Circular	N	Pockmark
150	117	2	Semi-circular	N	Large pockmark

151	300	10.5	Elliptical	N	Large pockmark
152	272	7	Semi-circular	N	Large pockmark
153	122	3	Elliptical	N	Large pockmark
154	221	3.5	Elliptical	N	Large pockmark
155	91	6	Elliptical	N	Pockmark
156	142	4	Elliptical	N	Large pockmark
157	295	9	Elliptical	N	Large pockmark
158	200	4	Semi-circular	N	Large pockmark
159	66	0.8	Circular	N	Pockmark
160	252	4	Semi-circular	N	Large pockmark
161	675	7	Elliptical	Y	Crater
162	110	3	Elliptical	N	Large pockmark
163	149	3	Semi-circular	N	Large pockmark
164	184	8	Circular	N	Large pockmark
165	526	14	Semi-circular	Y	Crater
166	77	1.5	Semi-circular	Y	Pockmark
167	51	1.5	Elliptical	N	Pockmark
168	77	1	Elliptical	N	Pockmark
169	111	1.5	Semi-circular	N	Large pockmark
170	262	12	Circular	N	Large pockmark

171	62	1	Circular	N	Pockmark
172	165	1.5	Semi-circular	Y	Large pockmark
173	165	2.5	Semi-circular	Y	Large pockmark
174	147	1	Elliptical	N	Large pockmark
175	140	2	Semi-circular	N	Large pockmark
176	149	2	Semi-circular	N	Large pockmark
177	246	6	Elliptical	N	Large pockmark
178	345	8	Semi-circular	N	Crater
179	353	6.5	Circular	N	Crater
180	87	3	Elliptical	N	Pockmark
181	116	2	Elliptical	N	Large pockmark
182	115	3.5	Semi-circular	N	Large pockmark
183	444	8	Semi-circular	N	Crater
184	638	6	Semi-circular	Y	Crater
185	397	10	Elliptical	Y	Crater
186	293	8	Elliptical	Y	Large pockmark
187	139	2.5	Circular	N	Large pockmark
188	175	6.5	Elliptical	N	Large pockmark
189	260	5	Elliptical	Y	Large pockmark
190	120	2	Semi-circular	N	Large pockmark

191	107	2	Circular	N	Large pockmark
192	110	1.5	Elliptical	N	Large pockmark
193	94	4	Elliptical	N	Pockmark
194	84	3	Elliptical	N	Pockmark
195	457	11	Semi-circular	N	Crater
196	80	0.8	Circular	N	Pockmark
197	140	2	Semi-circular	N	Large pockmark
198	191	10	Circular	Y	Large pockmark
199	200	6	Semi-circular	Y	Large pockmark
200	193	6	Elliptical	N	Large pockmark
201	178	3	Semi-circular	N	Large pockmark
202	100	3	Semi-circular	N	Pockmark
203	129	4	Elliptical	N	Large pockmark
204	109	3	Semi-circular	N	Large pockmark
205	162	6	Elliptical	N	Large pockmark
206	257	12	Elliptical	N	Large pockmark
207	233	12	Elliptical	Y	Large pockmark
208	111	1.5	Elliptical	N	Large pockmark
209	100	2	Circular	N	Pockmark

210	146	4	Semi-circular	N	Large pockmark
211	147	2	Elliptical	N	Large pockmark
212	123	3.5	Elliptical	N	Large pockmark
213	293	11	Circular	Y	Large pockmark
214	362	15	Elliptical	N	Crater
215	249	4.5	Elliptical	N	Large pockmark
216	110	4	Elliptical	Y	Large pockmark
217	405	20	Elliptical	N	Crater
218	65	3	Elliptical	N	Pockmark
219	87	1.5	Circular	N	Pockmark
220	210	6	Elliptical	N	Large pockmark
221	165	7	Elliptical	N	Large pockmark
222	250	8	Elliptical	Y	Large pockmark
223	288	6.5	Elliptical	N	Large pockmark
224	163	3	Semi-circular	N	Large pockmark
225	129	5	Elliptical	N	Large pockmark
226	210	12	Elliptical	Y	Large pockmark
227	127	6	Circular	Y	Large pockmark

228	148	2.5	Circular	N	Large pockmark
229	450	20	Semi-circular	Y	Crater
230	80	3	Circular	N	Pockmark
231	693	25	Semi-circular	Y	Crater
232	200	6	Semi-circular	N	Large pockmark
233	160	4	Semi-circular	N	Large pockmark
234	173	1.5	Semi-circular	N	Large pockmark
235	236	5	Elliptical	N	Large pockmark
236	277	12	Elliptical	N	Large pockmark
237	195	5	Semi-circular	N	Large pockmark
238	292	6	Elliptical	N	Large pockmark
239	569	9	Semi-circular	Y	Crater
240	178	10.5	Elliptical	Y	Large pockmark
241	144	4	Circular	Y	Large pockmark
242	224	6	Circular	N	Large pockmark
243	120	3	Semi-circular	N	Large pockmark
244	128	6	Circular	Y	Large pockmark
245	147	2	Semi-circular	N	Large pockmark

246	126	1.5	Circular	N	Large pockmark
247	82	3	Circular	N	Pockmark
248	78	3.5	Circular	N	Pockmark
249	80	1.2	Semi-circular	N	Pockmark
250	276	5	Elliptical	Y	Large pockmark
251	83	2.5	Circular	N	Pockmark
252	87	1	Circular	N	Pockmark
253	62	1	Circular	N	Pockmark
254	546	6	Semi-circular	N	Crater
255	100	2.5	Elliptical	N	Pockmark
256	50	0.5	Semi-circular	N	Pockmark
257	285	4	Circular	N	Large pockmark
258	152	3	Elliptical	Y	Large pockmark
259	78	2	Circular	N	Pockmark
260	128	1	Elliptical	N	Large pockmark
261	265	4.5	Elliptical	Y	Large pockmark
262	121	3	Elliptical	N	Large pockmark
263	91	2.5	Elliptical	N	Pockmark
264	43	1	Semi-circular	N	Pockmark
265	145	3	Circular	Y	Large pockmark
266	104	2	Circular	N	Large pockmark
267	152	2	Elliptical	N	Large pockmark

268	101	2	Circular	N	Large pockmark
269	112	2.5	Elliptical	Y	Large pockmark
270	94	2.5	Elliptical	Y	Pockmark
271	75	1.5	Circular	N	Pockmark
272	64	1	Circular	N	Pockmark
273	46	0.5	Circular	N	Pockmark
274	69	0.8	Circular	N	Pockmark
275	56	1	Semi-circular	N	Pockmark
276	60	1	Circular	N	Pockmark
277	108	3	Circular	Y	Large pockmark
278	104	0.5	Elliptical	Y	Large pockmark
279	82	2	Circular	Y	Pockmark
280	83	1	Circular	N	Pockmark
281	475		Semi-circular	N	Crater
282	97	2.5	Semi-circular	N	Pockmark
283	66	3	Circular	N	Pockmark
284	67	1	Circular	N	Pockmark
285	83	0.8	Circular	N	Pockmark
286	106	2.5	Circular	N	Large pockmark
287	46	0.6	Circular	N	Pockmark
288	62	1	Semi-circular	N	Pockmark

9.2 – Mounds spreadsheet

Table 4: Overview of mounds in the study area and their different properties. Y=Yes, P=Possibly, N=No. R-cone=Rounded cone.

Number:	Size (m):	Height (m):	Shape:	Shape2:	Related to pockmark (Y/P/N):	Inside pockmark (Y/N):
1	265	15	Elliptical	Flat	P	N
2	331	13	Elliptical	Flat	Y	N
3	324	15	Semi-circular	Flat	Y	N
4	438	13	Elliptical	Flat	Y	N
5	306	14	Elliptical	Flat	Y	N
6	70	1.5	Circular	Cone	N	N
7	79	2	Circular	Cone	N	N
8	69	2	Circular	Cone	P	N
9	71	1.5	Circular	Cone	N	N
10	59	1.5	Circular	Cone	N	N
11	103	6	Circular	R-cone	P	N
12	175	4	Semi-circular	Cone	Y	Y
13	73	2	Semi-circular	Cone	P	N
14	145	3	Elliptical	Flat	P	N
15	86	2	Elliptical	Flat	P	N
16	45	1	Circular	Cone	N	N
17	28	1.2	Circular	Cone	N	N
18	28	1	Circular	R-cone	N	N
19	280	8	Elliptical	Flat	N	N
20	93	6	Circular	R-cone	P	N
21	94	5	Elliptical	Cone	Y	N
22	110	4	Elliptical	Cone	Y	Y
23	156	2	Semi-circular	Flat	Y	N
24	43	2	Circular	Cone	N	N

25	46	1.5	Circular	R-cone	N	N
26	28	0.8	Circular	R-cone	N	N
27	468	11	Elliptical	Flat	Y	N
28	41	1	Circular	R-cone	N	N
29	167	1.5	Elliptical	Flat	Y	N
30	50	1.5	Circular	R-cone	P	N
31	605	6	Semi-circular	Flat	N	N
32	55	2	Circular	R-cone	N	N
33	37	1.5	Circular	R-cone	N	N
34	75	3	Circular	R-cone	N	N
35	460	6	Semi-circular	Flat	Y	Y
36	52	2.5	Circular	R-cone	N	N
37	31	0.2	Semi-circular	Cone	N	N
38	3	2.5	Elliptical	R-cone	N	N
39	54	3	Circular	R-cone	N	N
40	463	7	Semi-circular	Flat	Y	N
41	130	2	Circular	Flat	Y	N
42	81	10	Circular	Flat	Y	Y
43	132	4	Semi-circular	Flat	Y	N
44	90	5	Elliptical	Cone	P	N
45	79	6	Circular	R-cone	P	N
46	38	1	Circular	Cone	N	N
47	78	4	Circular	Cone	N	N
48	150	12	Elliptical	R-cone	Y	Y
49	96	6	Elliptical	Flat	Y	N
50	248	8	Semi-circular	R-cone	Y	N
51	199	8	Elliptical	Flat	N	N

52	117	6	Semi-circular	R-cone	Y	N
53	89	15	Semi-circular	Flat	Y	Y
54	75	17	Elliptical	Cone	Y	Y
55	56	10	Elliptical	Flat	Y	Y
56	61	8	Circular	R-cone	Y	Y
57	344	15	Semi-circular	Flat	Y	Y
58	134	17	Elliptical	Flat	Y	Y
59	99	15	Semi-circular	Flat	Y	Y
60	79	8	Elliptical	Flat	Y	Y
61	73	4	Circular	R-cone	P	N
62	89	2	Semi-circular	R-cone	Y	N
63	93	4	Semi-circular	Flat	N	N
64	118	5	Semi-circular	R-cone	P	N
65	349	5	Elliptical	Flat	Y	N
66	150	5	Semi-circular	Flat	Y	N
67	54	4	Circular	R-cone	Y	N
68	55	3	Circular	R-cone	P	N
69	150	3	Semi-circular	R-cone	P	N
70	54	0.5	Circular	Cone	N	N
71	41	1	Circular	R-cone	N	N
72	45	2	Circular	Cone	N	N
73	182	4	Semi-circular	Cone	N	N

74	139	1.5	Semi-circular	Cone	Y	N
75	98	10	Elliptical	Flat	Y	Y
76	75	4	Semi-circular	Cone	Y	N
77	100	1	Semi-circular	Cone	P	N
78	63	1	Elliptical	R-cone	Y	N
79	93	4	Elliptical	Cone	N	N
80	100	3	Elliptical	Cone	N	N
81	87	1.5	Elliptical	Cone	N	N
82	94	2	Elliptical	Flat	N	N
83	115	4	Elliptical	Cone	P	N
84	68	3	Elliptical	Cone	Y	Y
85	96	1.5	Elliptical	R-cone	N	N
86	141	5	Elliptical	R-cone	Y	Y
87	159	3	Elliptical	R-cone	P	N
88	208	2	Semi-circular	Flat	P	N
89	110	1.5	Circular	R-cone	Y	N
90	143	3	Elliptical	Flat	N	N
91	254	4	Semi-circular	Flat	Y	N
92	125	8	Elliptical	Flat	Y	Y
93	260	4	Elliptical	Flat	P	N
94	68	1.5	Elliptical	Cone	Y	Y
95	104	2	Elliptical	Cone	Y	N
96	48	1	Circular	Cone	N	N
97	54	2	Circular	R-cone	Y	N
98	338	5	Elliptical	Flat	Y	N
99	205	5	Semi-circular	R-cone	Y	N
100	120	2	Elliptical	Flat	N	N

101	127	4	Semi-circular	Flat	N	N
102	171	2.5	Semi-circular	Cone	N	N
103	90	2	Semi-circular	R-cone	Y	N
104	128	3	Elliptical	Flat	Y	N
105	157	25	Elliptical	Flat	Y	Y
106	73	18	Circular	Cone	Y	Y
107	71	7	Elliptical	Flat	Y	Y
108	238	10	Elliptical	Flat	Y	N
109	302	10	Elliptical	Flat	Y	N
110	467	15	Elliptical	Flat	Y	N
111	126	2.5	Elliptical	Flat	N	N
112	154	2.5	Elliptical	Flat	N	N
113	180	4	Semi-circular	Cone	Y	N
114	88	1.5	Elliptical	R-cone	P	N
115	90	3	Semi-circular	R-cone	N	N
116	44	1	Circular	Cone	N	N
117	86	1.5	Elliptical	Cone	Y	N
118	63	2	Circular	Cone	N	N
119	59	1.5	Circular	Cone	N	N
120	50	1	Circular	R-cone	N	N
121	65	2	Circular	Cone	N	N
122	67	2	Circular	Cone	N	N
123	37	0.6	Circular	Cone	N	N
124	81	2.5	Elliptical	R-cone	N	N
125	53	1	Circular	Cone	P	N
126	62	2	Circular	R-cone	P	N
127	49	1.5	Semi-circular	R-cone	N	N

128	321	3	Elliptical	Flat	N	N
129	84	1.5	Elliptical	R-cone	N	N
130	70	2	Semi-circular	Cone	N	N
131	97	5	Elliptical	Cone	Y	N
132	493	10	Elliptical	Flat	P	N
133	100	5	Elliptical	Flat	Y	N
134	83	4	Elliptical	R-cone	Y	N
135	494	5	Semi-circular	Flat	Y	N
136	117	3	Semi-circular	Flat	N	N
137	105	3	Elliptical	Flat	N	N
138	235	4	Semi-circular	Flat	N	N
139	262	3	Elliptical	Flat	Y	N
140	63	10	Elliptical	R-cone	Y	Y
141	269	8	Elliptical	Flat	Y	N
142	81	1.5	Elliptical	Cone	N	N
143	92	1	Circular	Cone	N	N
144	75	4	Circular	R-cone	Y	Y
145	85	0.8	Circular	R-cone	N	N
146	109	2.5	Circular	R-cone	N	N
147	147	3	Elliptical	Flat	Y	N
148	260	4	Elliptical	Flat	Y	Y
149	198	7	Elliptical	R-cone	Y	Y
150	205	2	Circular	R-cone	Y	N
151	92	1	Semi-circular	R-cone	N	N
152	140	5	Semi-circular	Cone	N	N
153	236	2	Elliptical	Flat	Y	N
154	272	4	Circular	R-cone	N	N

155	117	2	Semi-circular	Cone	N	N
156	76	1.5	Semi-circular	Cone	N	N
157	100	2	Semi-circular	R-cone	N	N
158	127	1.5	Semi-circular	R-cone	N	N
159	110	3.5	Elliptical	R-cone	P	N
160	103	3	Elliptical	R-cone	Y	N
161	93	2	Circular	R-cone	Y	N
162	100	2	Circular	Cone	Y	N
163	109	2	Semi-circular	R-cone	Y	N
164	110	1.5	Circular	Cone	N	N
165	182	2.5	Semi-circular	Flat	N	N
166	323	3	Elliptical	Flat	Y	N
167	135	1	Elliptical	R-cone	Y	N
168	69	4	Semi-circular	Cone	N	N
169	229	10	Circular	Flat	Y	Y
170	178	3	Elliptical	Flat	Y	N
171	211	3	Semi-circular	Flat	Y	N
172	146	4	Elliptical	Flat	Y	Y
173	206	2	Semi-circular	Flat	Y	Y
174	217	2	Elliptical	Flat	Y	N
175	93	4	Semi-circular	Flat	Y	Y
176	74	3	Elliptical	R-cone	N	N
177	77	4	Elliptical	R-cone	Y	N

178	84	3	Semi-circular	R-cone	N	N
179	105	2.5	Semi-circular	R-cone	N	N
180	70	2.5	Circular	R-cone	Y	N
181	121	4	Semi-circular	R-cone	N	N
182	188	2	Elliptical	Flat	N	N
183	82	1.5	Elliptical	R-cone	N	N
184	255	4	Elliptical	Flat	N	N
185	60	2.5	Semi-circular	Cone	P	N
186	71	3	Elliptical	Cone	P	N
187	125	2	Elliptical	R-cone	N	N
188	87	2	Elliptical	Cone	N	N
189	94	2	Semi-circular	Cone	N	N
190	109	3	Elliptical	R-cone	N	N
191	156	2	Semi-circular	Flat	N	N
192	73	1	Elliptical	R-cone	N	N
193	53	1	Semi-circular	R-cone	N	N
194	67	0.5	Circular	R-cone	N	N
195	57	1.5	Elliptical	R-cone	N	N
196	54	1	Circular	R-cone	N	N
197	69	0.4	Semi-circular	Cone	Y	N
198	45	0.5	Semi-circular	Cone	Y	N
199	70	1	Semi-circular	R-cone	Y	N

200	361	2	Semi-circular	Flat	Y	N
201	267	5	Semi-circular	Flat	Y	Y
202	86	2	Elliptical	Flat	Y	N
203	127	10	Circular	R-cone	Y	Y
204	94	2	Elliptical	R-cone	Y	N
205	52	4	Elliptical	Cone	Y	N
206	66	2.5	Elliptical	R-cone	N	N
207	81	3.5	Semi-circular	Cone	Y	Y
208	119	3	Elliptical	R-cone	Y	N
209	61	1.5	Semi-circular	R-cone	N	N
210	79	2	Circular	R-cone	N	N
211	43	0.5	Elliptical	Cone	N	N
212	56	2	Semi-circular	Cone	N	N
213	74	4	Elliptical	Cone	Y	N
214	124	4	Elliptical	Flat	Y	N
215	58	1.5	Circular	Cone	Y	N
216	110	2	Circular	R-cone	P	N
217	60	1	Semi-circular	R-cone	P	N
218	93	2.5	Circular	R-cone	N	N
219	64	2	Semi-circular	Cone	Y	N
220	68	2	Circular	R-cone	Y	N
221	59	1.5	Semi-circular	Cone	Y	N
222	54	2	Circular	R-cone	N	N
223	293	3	Elliptical	Flat	Y	N

224	230	3	Semi-circular	Flat	Y	N
225	72	4	Semi-circular	R-cone	Y	N
226	160	5	Elliptical	Flat	N	N
227	278	4	Semi-circular	Flat	Y	N

9.3 – Gas flares spreadsheet

Table 5: Overview of gas flares in the study area and their height.

Number:	Height (m):
1	22
2	73
3	58
4	74
5	31
6	46
7	37
8	11
9	38
10	36
11	46
12	24
13	64
14	81
15	18
16	19
17	95
18	85
19	64
20	20
21	44
22	27
23	37
24	17
25	66
26	47
27	48
28	67
29	10

30	79
31	9
32	32
33	40
34	49
35	88
36	81
37	9
38	4
39	43
40	17
41	71
42	13
43	34
44	16
45	24
46	18
47	19
48	15
49	37
50	20
51	31
52	8
53	54
54	80
55	51
56	30
57	61
58	59
59	28
60	46
61	19
62	33

63	27
64	28
65	4
66	28
67	54
68	10
69	6
70	8
71	5
72	4
73	32
74	45
75	74
76	16
77	38
78	46
79	18
80	25
81	57
82	30
83	37
84	18
85	12
86	23
87	5
88	29
89	40
90	34
91	11
92	13
93	16
94	16
95	37

96	23
97	75
98	28
99	35
100	37
101	68
102	36
103	10
104	13
105	19
106	45
107	13
108	46
109	51
110	18
111	29
112	29
113	15
114	7
115	49
116	59
117	15
118	10
119	24